

FORCED CURRENT EXCITATION IN SELECTABLE FIELD OF VIEW COILS
FOR 7T MRI AND MRS

A Dissertation

by

JIAMING CUI

Submitted to the Office of Graduate and Professional Studies of
Texas A&M University
in partial fulfillment of the requirements for the degree of

DOCTOR OF PHILOSOPHY

Chair of Committee,	Steven M. Wright
Committee Members,	Mary P. McDougall
	Jim Xiuquan Ji
	Robert D. Nevels
Head of Department,	Miroslav M. Begovic

August 2017

Major Subject: Electrical Engineering

Copyright 2017 Jiaming Cui

ABSTRACT

High field magnetic resonance imaging (MRI) provides improved signal-to-noise ratio (SNR) which can be translated to higher image resolution or reduced scan time. 7 Tesla (T) breast imaging and 7 T spine imaging are of clinical value, but they are challenging for several reasons: A bilateral breast coil requires the use of closely-spaced elements that are subject to severe mutual coupling which leads to uncontrollable current distribution and non-uniform field pattern; A spine coil at 7T requires a large field of view (FOV) in the z direction and good RF penetration into the human body. Additionally, the ability to switch FOV without the use of expensive high power RF amplifiers is desired in both applications. This capability would allow reconfigurable power distribution and avoid unnecessary heat deposition into human body.

Forced-Current Excitation (FCE) is a transmission line-based method that maintains equal current distribution across an array, alleviating mutual coupling effects and allowing current/field replication across a large FOV. At the same time, the nature of this method enables selectable FOV with the inclusion of PIN diodes and a controller.

In this doctoral work, the theory of FCE is explained in detail, along with its benefits and drawbacks. Electromagnetic simulation considerations of FCE-driven coils are also discussed. Two FCE-driven coils were designed and implemented: a switchable bilateral/unilateral 7T breast coil, and a segmented dipole for spine imaging at 7T with reconfigurable length. For the breast coil, shielded loop elements were used to form a volume coil, whereas for the spine coil, a segmented dipole was chosen as the final design

due to improved RF penetration. Electromagnetic simulations were performed to assist the design of the two coils as well as to predict the SAR (specific absorption rate) generated in the phantom. The coils were evaluated on bench and through MRI experiments in different configurations to validate the design. The switchable breast coil provides uniform excitation in both unilateral and bilateral mode. In unilateral mode, the signal in the contralateral breast is successfully suppressed and higher power is concentrated into the breast of interest; The segmented dipole was compared to a regular dipole with the same length used for 7T spine imaging. The segmented dipole shows a large FOV in the long mode. In the short mode, the residual signal from other part of the dipole is successfully suppressed. The ability to switch FOV and reconfigure the power distribution improves the B_1 generated with unit specific absorption rate towards the edge of the dipole, compared to the regular dipole.

ACKNOWLEDGEMENTS

I gratefully acknowledge my advisor, who is also the chair of my committee, Dr. Steven Wright. The Magnetic Resonance System Lab (MRSL) has been built into a remarkable place for the development not only in magnetic resonance engineering, but also in electrical engineering in general. Development of the lab took decades of hard work from Dr. Wright and his students, all of whom are acknowledged. I am grateful for Dr. Wright's lead into this area and to MRSL, where so much talent and expertise were found. I am also grateful for his guidance and patience throughout this work, as well as the sharing of his scientific expertise.

I would also like to thank my committee members: Dr. Mary McDougall for her help and advice in the projects that we collaborated on, as well as for sharing her resources when needed; Dr. Jim Ji and Dr. Robert Nevels for their invaluable time and input.

Thanks also goes to my friends and colleagues at the MRSL: Dr. John Bosshard for his guidance and endless patience. His expertise and experience is unparalleled; Dr. Neal Hollingsworth also for his guidance and brainpower into this work; Dr. Joseph Rispoli for his guidance on electromagnetic simulation software and coil development. Thanks also goes to Minyu Gu, Chenhao Sun, Samantha By and Dheyaa Alkandari for their help on some hardware constructions, as well as Wen-yang Chiang for interesting discussions on work and life. Other lab members are also acknowledged for their support and encouragement throughout my study.

I appreciate Drs. Ivan Dimitrov, Sergey Cheshkov, and Craig Malloy at University of Texas Southwestern Medical Center for providing access to the 7T magnet, as well as the time spent by Ivan and Sergey in assisting me with the imaging experiments. This work would not have been possible without their contribution.

Finally, thanks to my mother and father for their encouragement throughout my life and their support so that I can have access to a world-class education. Thanks to my dearest wife for her patience and love, as well as her company during the hard times towards my graduation.

CONTRIBUTORS AND FUNDING SOURCES

Contributors

This work was supervised by a dissertation committee consisting of Professor Steven Wright [advisor] and Professor Jim Ji, Professor Robert Nevels of the Department of Electrical & Computer Engineering and Professor Mary McDougall of the Department of Biomedical Engineering.

The MRI experiments described in Chapter IV and V were conducted under the help of Dr. Ivan Dimitrov (University of Texas Southwestern Medical Center, Philips Medical system) and Dr. Sergey Cheshkov (University of Texas Southwestern Medical Center).

Part of the hardware construction described in Chapter IV was performed with help from Dr. John Bosshard; Part of the hardware construction described in Chapter IV was performed with help from Chenhao Sun and Minyu Gu.

All other work conducted for the dissertation was completed by the student independently.

Funding Sources

This work was made possible in part by Cancer Prevention and Research Institute of Texas (CPRIT), grant number RP100625 and RP160847; as well as the National Institutes of Health grant numbers EB015908 and EB016394.

Its contents are solely the responsibility of the authors and do not necessarily represent the official views of the CPRIT.

NOMENCLATURE

TAMU	Texas A&M University
UTSW	University of Texas Southwestern
MRI	Magnetic Resonance Imaging
MRS	Magnetic Resonance Spectroscopy
T	Tesla
FDTD	Finite-Difference Time Domain
MRI	Magnetic Resonance Imaging
FCE	Forced Current Excitation
FOV	Field of View
RF	Radio Frequency
TX	Transmit
SAR	Specific Absorption Rate
SAR_{10g_max}	The maximum of 10 gram tissue averaged specific absorption rate
SAR_{1g_max}	The maximum of 1 gram tissue averaged specific absorption rate
EM	Electromagnetic
CEST	Chemical-Exchange-Saturation-Transfer

TABLE OF CONTENTS

	Page
ABSTRACT	ii
ACKNOWLEDGEMENTS	iv
CONTRIBUTORS AND FUNDING SOURCES.....	vi
NOMENCLATURE.....	vii
TABLE OF CONTENTS	viii
LIST OF FIGURES.....	xi
LIST OF TABLES	xvi
CHAPTER I INTRODUCTION	1
1.1 Motivation.....	1
1.2 Dissertation Organization	2
CHAPTER II BACKGROUND.....	3
2.1 Magnetic Resonance Imaging	3
2.1.1 RF Transmission and Reception	3
2.1.2 Gradients and Spatial Encoding	4
2.2 SAR and FDTD Algorithm	4
2.3 Seven Tesla MRI.....	5
2.3.1 Benefits and Challenges.....	5
2.3.2 Parallel Transmission	6
2.4 Challenges in 7T Breast and Spine Imaging	7
2.4.1 Challenges in 7T Breast Imaging	7
2.4.2 Challenges in 7T Spine Imaging	8
2.4.3 Coupling Between Elements in an Array	9
CHAPTER III FORCED-CURRENT EXCITATION.....	12
3.1 Introduction	12
3.2 Benefit from FCE	12
3.3 FDTD Simulation for FCE Coils	14

3.4 Losses in FCE Coils	20
3.5 Detuning FCE Coils	22
3.6 FCE with Switchable Field of View	24
CHAPTER IV FCE BILATERAL BREAST COIL AT 7T*	26
4.1 Introduction	26
4.2 Switched-mode Bilateral Breast Coil at 7T	27
4.2.1 Introduction	27
4.2.2 Coil Design	29
4.2.3 Forced-Current Excitation and Mode Switching	31
4.2.4 Electromagnetic Modeling	34
4.2.5 Coil Testing - Bench Measurements	37
4.2.6 Coil Testing - MRI Experiments	42
4.2.7 Summary	46
4.3 Modified Bilateral Breast Coil for Receive Array Insert at 7T	47
4.3.1 Introduction	47
4.3.2 Coil Design	49
4.3.3 Transmission with Shielded Twinaxial Cable	51
4.3.4 Coil Testing-Bench Measurement	54
4.3.5 Detuning	55
4.3.6 Coil Testing – MRI Experiments	58
4.4 Method for Simultaneous Tuning in Switched-Mode FCE Coils	60
CHAPTER V SWITCHABLE TRANSMIT ELEMENT FOR SPINE IMAGING AT 7T	65
5.1 Introduction	65
5.2 Rung Element Configurations for Spine Imaging at 7T	66
5.2.1 Initial Trials	67
5.2.2 Uniform Ground vs. Separate Ground for Rung Element	72
5.2.3 Height of the Rung	73
5.3 A Segmented Rung Element with FCE and Selectable FOV	75
5.4 The Effect of the Length of a Dipole on Transmit Efficiency	80
5.4.1 Description	80
5.4.2 Electromagnetic Simulation	80
5.4.3 Numerical Validation-Methods	82
5.4.4 Numerical Validation-Results	83
5.5 A Segmented Dipole Design with FCE and Selectable FOV for 7T Spine Imaging	85
5.5.1 Introduction	85
5.5.2 Element Comparison	87
5.5.3 Element Design and Implementation	95
5.5.4 Bench Measurement	98

5.5.5 MR Experiment	100
5.5.6 Conclusions	105
CHAPTER VI CONCLUSIONS AND DISCUSSIONS	107
6.1 Conclusions	107
6.2 Possible Improvements	109
REFERENCES	111
APPENDIX A THE USE OF INFRARED CAMERA IN DEBUGGING RF COILS AND ESTIMATING CURRENT DISTRIBUTION.....	122

LIST OF FIGURES

	Page
Fig. 1. Two coupled coils	9
Fig. 2. FCE driven, multi-element array	13
Fig. 3. Matrix representation of the FCE configuration	13
Fig. 4. Coupling matrix and current source representation	15
Fig. 5. A Helmholtz pair with fat (pink) and muscle (yellow) as loading. Modeled in XFDTD	17
Fig. 6. Current ratio between I_1 and I_2 vs. current source impedance	18
Fig. 7. Resistance of the top loop, after convergence vs. source impedance	19
Fig. 8. Power loss percentage vs. reflection coefficient and attenuation factor. Length of the cable is 40 cm	21
Fig. 9. Detuning test setup.....	23
Fig. 10. S11 of receive coil, Left: PIN diode reverse biased (12V) (frequency span: 50 MHz). Right: PIN diode forward biased (100 mA).....	24
Fig. 11. Switchable bilateral quadrature coil closed in a housing (left) and with covers removed (right) forms.....	30
Fig. 12. Possible quadrature B_1 field arrangements (a): with the B_1 fields in the same direction; (b): with the B_1 fields in opposite directions. The arrangement on the left was chosen based on numerical simulations.	31
Fig. 13. Schematic of switching network for operating mode control of the Helmholtz/saddle pairs. The same DC signals for switching are routed to the Helmholtz and saddle switching network.	33
Fig. 14. Coil and phantom model. The RF shields are not shown for clarity	35
Fig. 15. Central axial plane B_1 and 10g averaged SAR maps in modes 1-3. The results were scaled to 1W total input power to the coil. 0 dB corresponds to 1.97 μ T and 0.99W/kg in the B_1 and SAR maps, respectively.....	36
Fig. 16. Comparison between FCE mode and non-FCE mode. (a) S11 of the bilateral coil over a 50 MHz span, good matching was achieved at the coil port for	

both cases; (b) Normalized field profiles along the central axis of the left coil at 298 MHz, presented in decibels. In non-FCE mode the coil exhibits field inhomogeneity even when unloaded due to capacitor tolerances in the elements, both of which are connected to a common tune capacitor. When operated in FCE mode, the coil shows much better homogeneity; (c) Normalized S21 over a 50 MHz span at +1 cm on the central axis of the left coil. When operated in FCE mode, the desired mode (equal currents) appears at 298 MHz, giving a uniform field plot. When operated in non-FCE mode, the coil shows a more complex mode structure, and does not provide equal currents in the coil elements resulting in an inhomogeneous field.39

Fig. 17. One dimensional B₁ profiles across the ROI, along x direction. The data measured in modes 1-3 are normalized to a global maximum and plotted together for comparison. When operated in unilateral mode, the active coil has around 3 dB higher sensitivity than when operated in bilateral mode. The non-active coil has much lower sensitivity (9-20 dB lower than the active coil), which indicates successful detuning.41

Fig. 18. Coil mode performance as illustrated by phantom and in vivo imaging: (a, top row) switched-mode coil: bilateral mode; (b) switched-mode coil: right only mode; (c) switched-mode: left only mode. Original in vivo acquisition (coronal) and reconstructed (axial) images are shown in the middle and right columns, respectively. Symmetric performance is observed in the bilateral mode, while excellent signal localization is seen in the unilateral modes.43

Fig. 19. (a./b.) In vivo 3D THRIVE images (first two rows, with and without fat suppression, respectively) in bilateral mode demonstrate coil performance for varying breast sizes. Good coverage of both breasts and the chest wall is seen, along with uniform fat suppression attesting to the transmission homogeneity of the coil. (c.) Flip angle maps demonstrate sufficient homogeneous excitation over the bilateral FOV.46

Fig. 20. Dipole mode formed by the baluns on connected FCE coaxial cables52

Fig. 21. Photo of the double-probe detuning setup56

Fig. 22. S₂₁ measurement: Tuning vs. Detuning. Helmholtz pair56

Fig. 23. S₂₁ measurement: Tuning vs. Detuning. Saddle pair57

Fig. 24. (Left) The switched-mode bilateral breast coil reported earlier; (Right) Modified FCE bilateral coil for receive insertion. Each Helmholtz pair consists of two 166mm loops spaced 80 mm apart, with a concentric

coplanar shield surrounding each loop. Each saddle pair consists of two 165 x 94 mm rectangular coils mounted inside a 3D printed cylindrical tube with an inner diameter of 152mm. Reprinted with permission from [56].	59
Fig. 25. MR Image (coronal) taken from FCE bilateral coil. Homogeneous excitation is achieved. Reprinted with permission from [56].	59
Fig. 26. Bilateral FCE transmit coil with 32- channel array coil. A) front view of the bilateral coil with array coil integrated. The $\lambda/4$ T.L. are connected from the two Helmholtz pairs to a CVP, then from CVP to the match and tune network (M/T). B) side view of the integrated coil and array. Reprinted with permission from [56].	60
Fig. 27. Equivalent circuit for different modes	61
Fig. 28. Photo of the FCE coil modified for simultaneous tuning	63
Fig. 29. Profile across the coil in different modes, after the modification. Values are scaled to the global maximum.	63
Fig. 30. Model rendering for rungs and dipoles in different configurations	67
Fig. 31. B_1 pattern and maximum 10g averaged SAR in each case	68
Fig. 32. $B_1 / \sqrt{\text{input_power}}$ efficiency comparison between separate rungs and connected rungs, in different modes	70
Fig. 33. $B_1 / \sqrt{\text{SAR}_{10\text{g_max}}}$ efficiency comparison between separate rungs and connected rungs, in different modes	71
Fig. 34. Three short rungs - middle only vs. all three excited	72
Fig. 35. Three short rungs configuration-a uniform ground vs. three separate grounds..	73
Fig. 36. Pattern from the configuration where separate grounds are used	73
Fig. 37. Sagittal B_1 pattern for rung element of different height	74
Fig. 38. Transverse field pattern comparison - rung vs. dipole	75
Fig. 39. (Left) Front side of the coil. The rungs are fed from the side. (Right) Back side of the coil, with the switching circuit, the coax cable, and the matching circuit. Reprinted with permission from [94].	77

Fig. 40. Bench measurement in four modes. Mode 4 demonstrates uniform excitation across large FOV, while mode 1-3 demonstrate higher $B_1/\sqrt{\text{input_power}}$ efficiency (3.5-4 dB) at the corresponding region. Reprinted with permission from [94].	78
Fig. 41. Long dipole and three short dipoles as modeled in Remcom XFDTD	81
Fig. 42. Four different designs with the same overall length (37 cm), top view. Case 1 (a): standard dipole; Case 2 (b): separate rungs (ground is displayed as black); Case 3 (c): separate dipoles; Case 4 (d): segmented dipole	89
Fig. 43. Phantom model, and the sagittal plane where B_1 is calculated. The bore of the magnet is modeled but not displayed.	89
Fig. 44. Mode definition for segmented and separated configuration	90
Fig. 45. (Top) Calculated B_1 pattern of the separate dipoles (case 3) and (Bottom) the segmented dipole (case 4) calculated from simulation. The segmented dipole provides a more continuous excitation pattern.	91
Fig. 46. Calculated $B_1/\sqrt{\text{SAR}_{10\text{g_max}}}$ pattern of the separate rung (Left) and the segmented dipole (Right) in the central sagittal plane. The y direction profiles where $B_1/\sqrt{\text{SAR}_{10\text{g_max}}}$ efficiency was compared are marked with dashed black line.	92
Fig. 47. Calculated $B_1/\sqrt{\text{SAR}_{10\text{g_max}}}$ efficiency comparison between the separated rung (Mode B) and the segmented dipole (Mode B). The profile position being compared was shown in Fig. 46.	93
Fig. 48. Z direction profile being compared as marked in the calculated $B_1/\sqrt{\text{SAR}_{10\text{g_max}}}$ pattern of the reference standard dipole	94
Fig. 49. Calculated z direction profile comparison at 5cm deep. Comparison was made between the segmented dipole in different modes and the standard dipole. The ability to switch FOV is observed.	95
Fig. 50. Left: Layout of the coil, including the dipole, quarter-wave feedlines with baluns incorporated, switching circuit as well as matching circuit; Right: schematic of the switching circuit	96
Fig. 51. $B_1/\text{max E}$ results measured on bench at 5cm into the phantom. Comparison was made between the segmented dipole in different modes and the standard dipole	100

Fig. 52. Effect from using two dipoles together: (a) Axial image from segmented dipole element #1 (b) Axial image from segmented dipole element #2 (c) Axial image from two segmented dipoles transmitting at the same time. When two dipoles are used, the axial coverage is improved.	102
Fig. 53. Sagittal THRIVE images from the segmented dipoles (a-d) and the reference standard dipoles (e): (a) Segmented dipoles-Mode A. (b) Segmented dipoles-Mode B. (c) Segmented dipoles-Mode C. (d) Segmented dipoles-Mode A+B+C. (e) Reference standard dipoles. For the segmented dipole, in long mode, long coverage in z direction is achieved; In short mode, signal in the ‘off’ region is largely suppressed.	103
Fig. 54. Flip angle series experiment performed on the segmented dipole and the standard dipole. Horizontal axis indicates the pulse number in the series. The length of the RF pulse is linearly proportional to the pulse number. The maximum signal corresponds to 90 degree flip angle.	104
Fig. 55. Extra heat observed in the tuning capacitor	123
Fig. 56. Thermal images of match and tune cap after new capacitors were installed, and the reference photo.....	124
Fig. 57. A loop coil broken up by distributed capacitors	125

LIST OF TABLES

	Page
Table 1 Transmitter (TX) drive scale (DS), transmitter relative output power, and bench measurement of the three modes	44
Table 2 Losses of different cables (twinax vs. coax)	53
Table 3 Modified bilateral transmit coil-impedance of all Helmholtz pair element	54
Table 4 Modified bilateral transmit coil-impedance of all saddle pair elements	54
Table 5 S21 measurement at different locations inside the transmit coil, measured with a shielded probe	55
Table 6 Impedance and return loss before and after the modification	62
Table 7 Impedance, B_1 and SAR results calculated from XFDTD with three cases: Long dipole; Three short dipoles (excite all); Three short dipoles (excite only the middle one)	81
Table 8 Impedance comparison in different simulation environments and analytical approach. Comparison is made between dipoles of different length	84
Table 9 Calculated B_1 field scaled to input current. Comparison is made between dipoles of different length at 4 cm away	84
Table 10 Calculated B_1 field scaled to input power. Comparison is made between dipoles of different length at 4 cm away	84

CHAPTER I

INTRODUCTION

1.1 Motivation

Due to its excellent soft tissue contrast, unique diagnostic information and non-invasive nature, MRI has found its use in numerous medical applications such as oncological, cardiovascular, neurological and functional MRI. Since the introduction of MRI, the main magnetic field for clinical available MRI has raised from below 1 Tesla (T) to 1.5T and 3T, driven primarily by the improvement in SNR [1-4]. SNR can be traded for reduced scan time or higher spatial resolution by adjusting the pulse sequence design. Some recent research in 7T MRI/MRS has demonstrated an advantage in SNR when compared to 3T [5-7], with the challenges being shortened RF wavelength, complicated RF excitation pattern, as well as increased heat deposition [8, 9]. In particular, breast imaging and spine imaging at 7T is challenging due to mutual coupling between elements as well as the required FOV [10, 11]. In addition, it is often desirable to avoid unnecessary power/heat deposition in part of the body not being examined, therefore a flexible control of FOV is desirable in these applications. This work describes the use of Forced-Current Excitation in addressing the challenges of these applications, as well as the reconfiguration of FCE to include the switchable FOV capability.

1.2 Dissertation Organization

This dissertation is divided into five chapters. Chapter I describes the general motivation of the work as well as the organization of this dissertation; Chapter II gives the background of this work by introducing MRI. It then discusses the benefits and challenges in of MRI at 7T, where the majority of this work was performed. In particular, challenges in 7T breast and spine imaging are discussed in detail. Chapter III describes the Forced-Current Excitation method in detail, including its advantages and drawbacks. Electromagnetic simulation of FCE coils is also discussed; the method of reconfiguring a FCE coil to have a switchable field of view is introduced at the end of this chapter. Chapter IV describes the use of the ‘FCE+switchable FOV’ method in a switchable bilateral/unilateral 7T breast coil design. Electromagnetic simulations were performed to assist the coil design; MRI results as well as bench measurements were performed for validation; a modified version of the bilateral coil, specifically designed to house a 32-channel receive array, is also introduced and characterized. Finally, Chapter V describes the design of a segmented/switchable 7T spine coil using FCE with a switchable FOV principle. Simulations were performed to provide comparison between different element designs, as well as to study the effect of the length in a dipole antenna. Finally, a segmented dipole design is presented. The design of the dipole and the switching circuit is discussed in detail. Through simulations and MR experiments, its $B_1/\sqrt{\text{SAR}_{10\text{g_max}}}$ as well as $B_1/\sqrt{\text{input_power}}$ efficiency was compared to a regular dipole used for 7T spine coil. Throughout this dissertation, B_1 stands for the magnetic field produced by the coil during transmit, which is also commonly denoted as B_1^+ .

CHAPTER II

BACKGROUND

2.1 Magnetic Resonance Imaging

2.1.1 RF Transmission and Reception

The concept of MRI was developed from nuclear magnetic resonance (NMR). NMR utilizes the fact that nucleus that have a nonzero spin property (such as ^1H and ^{13}C), is able to absorb and re-emit electromagnetic energy [12]. The frequency of this radiation is dependent on the strength of the main magnetic field (B_0), with the relationship given by the Larmor equation:

$$\omega_0 = \gamma B_0$$

For MRI, the frequency is typically in the radio frequency (RF) range.

A RF resonant structure, often called a RF coil, is used to transmit and detect a time-varying magnetic field, often called the B_1 field. The B_1 field is perpendicular to the direction of the main magnetic field, B_0 . The sample being examined is exposed to the B_1 field excitation and gives a response back which can be detected by the same or a separate RF coil. For MRI, the same principle is applied. Traditionally it was considered important to use a volume RF coil, such as a birdcage coil, that produces a uniform B_1 field. In later stage of the development of MRI, it was discovered that a surface coil can also be utilized [13, 14]. A surface coil is more sensitive to the signal and noise closer to the coil and less sensitive to those further away. This property was exploited in the development of the receive array, which can be used to obtain a higher signal-to-noise ratio (SNR) or a

reduced scan time [14, 15]. On the transmit side, it is also common now to use multiple surface coils to tailor the B_1 field, as will be discussed in section 2.2.

2.1.2 Gradients and Spatial Encoding

In NMR, there are only two types of magnetic field, the static magnetic field and RF field. Lauterbur et al noted that by introducing a linear gradient field on top of the main magnetic field, B_0 , the spatial location information from the sample can be mapped to the frequency spectrum [16]. The frequency spectrum can then be used to form tomographic reconstructed images and retrieve the spatial details of the samples, enabling the early form of MRI. Later, more complicated methods were introduced to reconstruct MRI images more conveniently [17], namely amplitude adjustable phase-encoding.

2.2 SAR and FDTD Algorithm

The RF transmit coil is designed to generate a time-varying magnetic field which excites the sample/patient. The sample then gives a response, a time-varying magnetic field, which is detected by a RF receive coil. According to Maxwell's equation, an electric field is also generated together with the time-varying magnetic field:

$$\nabla \times \mathbf{E} = -j\omega \mathbf{B}; \nabla \times \mathbf{H} = j\omega \mathbf{D} + \mathbf{J}$$

Electric fields generate currents in conductive media, which in turn generate heat. A measure of the rate at which energy is absorbed by the human body when exposed to an electromagnetic field is called the specific absorption rate (SAR), computed from [18]:

$$\text{SAR} = \frac{\sigma E^2}{\rho}$$

The commonly specified limit for SAR is usually averaged either over the whole body, or over a small sample volume (typically 1 g or 10 g of tissue). The FDA specifies the limit on the maximum specific absorption rate (SAR) that can be applied to a human body or to extremities [18]. Therefore, in an MR experiment, it is important to predict an upper limit on the SAR generated from the RF coil.

Due to its excellent ability to model complicated material in three dimensions, finite-difference time domain (FDTD) has become the gold standard for predicting SAR produced by RF coils/antennas [19, 20]. The method is a time-domain numerical electromagnetic method. It discretizes Maxwell's equation in both space and time, and computes the electric and magnetic field in a leapfrog manner, converging to a steady-state solution of the problem [21, 22]. In this doctoral work, a FDTD-based software 'Remcom XFDTD v7.5' was used to calculate the SAR for different coils evaluated.

2.3 Seven Tesla MRI

2.3.1 Benefits and Challenges

Since the development of MRI, great research has been undertaken towards raising the main magnetic field strength, with the main driver being the approximately linear relationship between signal to noise ratio (SNR) and field strength [4].

$$SNR_v = \frac{|V_{sig}|}{V_{noise}} = \frac{\sqrt{2\gamma B_0 \Delta V M_0 |B_t|}}{\sqrt{4kT \Delta f R}}$$

Where M_0 is the net magnetization, B_t is the transverse magnetic field (B_1), and γ is gyromagnetic ratio.

SNR can be traded for higher spatial resolution or faster scan time [4] – which are the limitations of clinical MRI. Nowadays most of the MRI systems in hospitals employs a 1.5 T or a 3T superconducting magnet.

Several 3T MRI/MRS experiments have concluded that higher sensitivity is needed [23], and 7T MRI/MRS has the potential to provide more diagnostically useful information because of the expected improvement in SNR.

However, the advance of 7T does not come without challenges. The most prominent challenge is on the RF side - As stated before, the Larmor frequency is linearly proportional to the field strength. As the frequency goes up, the RF wavelength shortens. At 7T, the wavelength in the body becomes significantly shorter than the dimension of abdomen. Additionally, dielectric resonance effect or simply wave interference effects becomes more prominent, which adds to the contrast of the image, bringing challenges to diagnoses [24].

Furthermore, the RF losses increases with frequency [25], and therefore imaging objects that are deeper in the body is challenging due to power limitation. The limitation occurs either in the available peak power (output from the power amplifier), or in the maximum SAR (heat absorbed in the patient).

2.3.2 Parallel Transmission

In higher fields (3T and above), the dielectric resonance behavior become increasingly apparent [26, 27], and therefore it is hard to either create an overall homogeneous excitation field pattern or maintain transmit efficiency over a given region. Parallel transmission is analogous to the concept of parallel receive (often referred to as

parallel imaging). It appears in two forms: B_1 shimming [28] and spectral-spatially tailored excitation pattern [29, 30]. The former uses an array of independent coils and adjusts the amplitude and phase of each coil to obtain uniform excitation or optimum transmit efficiency; the latter also uses an array of independent coils, together with carefully-designed RF pulses and gradient waveforms to spatially select the area to be excited. To function well, both methods require the coil elements to have independent profiles. Although powerful, especially in high field, the method is very expensive due to the price of high power RF amplifiers, and is often not available at clinical sites to date. Coupling between transmit element is difficult to overcome, which will be discussed in detail in section 2.4.

2.4 Challenges in 7T Breast and Spine Imaging

2.4.1 Challenges in 7T Breast Imaging

7T bilateral breast imaging requires a relatively large field of view (FOV). A naïve solution is to use a sufficiently large loop to encompass both breasts. However, a loop of this size will exhibit highly inhomogeneous excitation pattern, and will be highly inefficient due to its size and the associated radiation losses. A more appropriate design is to use two identical coils, one surrounding each breast [31]. To create a homogenous field pattern in the anterior-posterior direction (y direction in MRI system), a Helmholtz pair is a viable option. In this configuration, the distance between elements is very small, and using a multi-element array volume coil means that a method is needed to either decouple

these elements, or minimize the impact of coupling. Decoupling transmit elements from each other is a difficult task, and will be covered in section 2.4.

Furthermore, although bilateral imaging is more clinically useful [32], sometimes it is desirable to only investigate a single breast, avoiding while heat deposition in the other one. Furthermore, this will allow more power to be focused in the breast that is of interest, or with lesion. In other words, the $B_1/\sqrt{\text{input_power}}$ is higher in the unilateral configuration, and may benefit power-hungry applications such as proton-decoupled second nuclei spectroscopy [33].

2.4.2 Challenges in 7T Spine Imaging

7T spine imaging is also demanding, especially on the transmission side. The length of the spine requires a long FOV in the head-foot direction (z direction in MRI system) [34]. The depth of the spine also varies along its length, with the thoracic spine at the surface of the back and the cervical spine and lumbar spine deeper in the body. This requires good RF penetration. The length of patients' spines can also vary significantly, calling for a length-variable design.

Long dipoles can be used to provide good sagittal coverage and good RF penetration (radiation), as is shown in [35]. However, the current falls off towards the dipole edge, together with the B_1 field. In the end the $B_1/\sqrt{\text{SAR}_{10\text{g_max}}}$ performance is poor towards the edge. One solution is to use multiple segments along the z direction, with each of them being able to be switched on and off. This can be achieved through using multiple power amplifiers and parallel transmission [11]. However, this will be an extremely expensive solution considering the cost of high power RF amplifiers. Furthermore, when

using multiple segments to construct a long spine coil, the coupling between the small segments still needs to be addressed, as with breast imaging.

2.4.3 Coupling Between Elements in an Array

It is commonly known that electromagnetic resonators couple with each other, as is depicted in Fig. 1. For MRI RF coils, the resonators are often designed to produce magnetic field, with the electric field being a side product. The coupling appears in the form of inductive coupling:

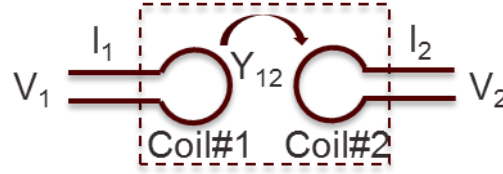


Fig. 1. Two coupled coils

Equation 1 Coupling equation between two coils

$$\begin{aligned} I_1 &= Y_{11}V_1 + Y_{12}V_2 \\ I_2 &= Y_{22}V_2 + Y_{21}V_1 \end{aligned}$$

As shown in Equation 1, when mutual coupling exists, the current of each coil is a function of the excitation voltage from the other coil, complicating the control of current. The situation is different between receive coil decoupling and transmit coil decoupling. For receive coil decoupling, the low-input impedance preamplifier decoupling method has become the gold standard due to its good decoupling performance and scalability without adding too much complexity to coil design [15, 36]. On the transmit side however, this method cannot be directly applied.

Coupling between transmit array elements causes complicated excitation patterns, difficulty in tuning, as well as compromised efficiency. For an array either used for parallel transmission, or just simply functioning as a volume coil, the coupling between its elements needs to be addressed. Coupling between elements in an array can be mitigated using a variety of techniques: Overlapping adjacent loop elements can achieve a net flux of near zero and alleviate inductive coupling, however the method only works up to a three-element array; A network of passive elements consisting of capacitors or inductors can be used to diagonalize the coupling matrix [37-39], reducing the mutual coupling effect. This adds to the complexity of coil design. For elements separated far apart, it is difficult to add such a network between them effectively [37-41]; In certain applications, an element geometry that has intrinsically low mutual coupling, such as a microstrip/transmission line of a certain wavelength can be used [42]. However, the B_1 pattern of these elements may not satisfy the needs of some applications; A decoupling element, based on induced current compensation, can be placed between adjacent elements to cancel mutual inductance or impedance[43, 44]. But this method is also limited to nearest element decoupling.

Some of the methods above are limited to two or three element decoupling [37-41, 43, 44]. Others pose limitations to element geometry or array configuration [37, 38, 40-42]. Approaches that allows easier channel count scaling, which do not depend on coil geometry have also been presented: A ‘forced current excitation (FCE)’ method uses one power amplifier and odd multiples of quarter-wavelength transmission lines to excite multiple elements to achieve equal current across the array[45]. The method allows current

replication without added amplifiers and provides an easy way to tune a multi-element array, but it does not provide B_1 shimming capability on its own. This method will be discussed in detail in this dissertation and will be used with a breast coil and a spine coil.

An active feedback technique can be used to cancel out induced currents, but this has significant bandwidth requirements [46]. Amplifiers can also be designed to mitigate coupling, for instance: a current source amplifier avoids induced current by presenting a high output impedance towards the coil; Similarly, a low output impedance amplifier can be designed to provide a high impedance to the coil and avoid mutual coupling. Although they have limited operational bandwidth and some designs have significant reductions in output power [47-49].

CHAPTER III

FORCED-CURRENT EXCITATION

3.1 Introduction

In this chapter, the Forced-Current Excitation method-FCE, is discussed in detail. In section 3.2, the benefit from using FCE on multi-element arrays is explained. ABCD matrix analysis is performed to explain the method; In section 3.3, the issues of simulating FCE coils in FDTD is discussed, and several simulations is performed to decide a proper source impedance; In section 3.3, the loss associated with FCE feeding network is analyzed, and some conclusion is reached as to how to minimize it; In section 3.4, an easy method of detuning FCE coils is introduced and tested on bench; Finally in section 3.5, the detuning method is used to enable the switchable FOV feature with the help from additional PIN diodes. This configuration still maintains the FCE feature.

3.2 Benefit from FCE

FCE is a technique that has been used in antenna phased arrays. By forcing the feed current to be equal, it alleviates the problem from mutual coupling between closely spaced antenna elements. Because of its unique feature, it has found its use in MRI coil designs, especially in high field MRI where multiple elements are used more often. In [45], the theory behind FCE is explained by relating the excitation source (a voltage source) and the load current of several elements. Here, a more generalized expression is presented by using a two-port network analysis and ABCD matrix calculation. It is also

pointed out that the excitation source could be replaced by a passive load, if the purpose is only to maintain equal current between coil elements.

Each coil element is fed directly from a quarter-wave transmission line, where the other ends of the transmission lines are connected together in parallel at a common-voltage point (CVP), as shown in Fig. 2. A single matching network, located after the CVP, is used to match and tune the entire coil structure.

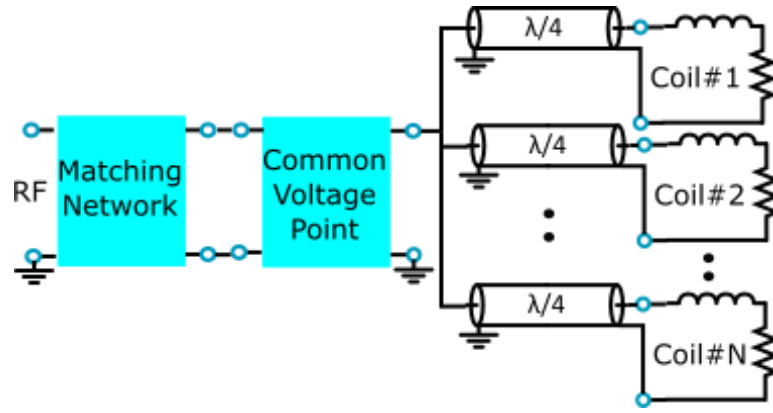


Fig. 2. FCE driven, multi-element array

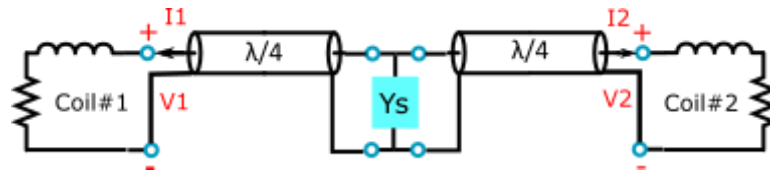


Fig. 3. Matrix representation of the FCE configuration

The relation between I_1 and I_2 , as well as V_1 and V_2 (as shown in Fig. 3), can be calculated from series connected ABCD matrix:

$$\begin{aligned}
\begin{bmatrix} V_1 \\ I_1 \end{bmatrix} &= \begin{bmatrix} A & B \\ C & D \end{bmatrix} \begin{bmatrix} V_2 \\ -I_2 \end{bmatrix} \\
&= \begin{bmatrix} 0 & jZ_0 \\ j/Z_0 & 0 \end{bmatrix} \begin{bmatrix} 1 & 0 \\ Y_s & 1 \end{bmatrix} \begin{bmatrix} 0 & jZ_0 \\ j/Z_0 & 0 \end{bmatrix} \begin{bmatrix} V_2 \\ -I_2 \end{bmatrix} \\
&= \begin{bmatrix} -1 & -Z_0^2 Y_s \\ 0 & -1 \end{bmatrix} \begin{bmatrix} V_2 \\ -I_2 \end{bmatrix} \Rightarrow
\end{aligned}$$

$$I_1 = 0 \times V_2 - (-1) \times I_2 = I_2$$

That proves that: In this configuration, despite what value the Y_s takes, the current of all elements are the same. Y_s can be a excitation source, or a passive load (or just an open circuit) if the coil is fed from somewhere else.

3.3 FDTD Simulation for FCE Coils

FDTD method is widely used in MRI coil design and SAR calculation, due to its outstanding ability to model complex anatomical structures as well as predicting B_1 and E field distribution. However, commercial FDTD software packages are often not equipped with the ability to model coaxial transmission line in 3D models, e.g Remcom XFDTD 7.4, and therefore cannot model the FCE configuration. Instead, a source need to be placed at each coil element to provide excitation directly. For standard RF coil modeling, it is common to use a complex conjugate-matched source impedance to achieve easy impedance matching, or a 50 ohm source impedance to study the coupling between coil elements and the transmit system. These types of source do not model the FCE feature by nature, as the delivered voltage/current to the coil can be altered by the load as well as

voltage/current from other element due to coupling. If the equal current condition is not modeled correctly, the B_1 field pattern and the SAR results will be invalid.

It is not difficult to conclude that a current source works better than a voltage source in our case, as the FCE is tied with input current. The question is the value of the source impedance.

In FDTD algorithm, two coil elements and their current sources can be modeled as in Fig. 4:

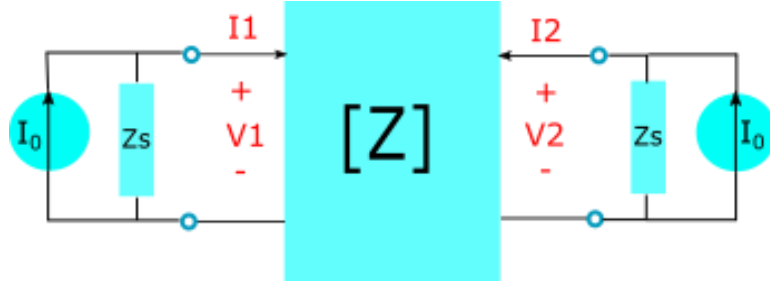


Fig. 4. Coupling matrix and current source representation

I_0 and Z_s together constitute the current source in FDTD algorithm. The Z matrix represents the two coils, with Z_{12} representing the coupling coefficient between them.

$$V_1 = (I_0 - I_1)Z_s = Z_{11}I_1 + Z_{12}I_2;$$

$$V_2 = (I_0 - I_2)Z_s = Z_{21}I_1 + Z_{22}I_2;$$

It can be calculated that
$$\frac{I_1}{I_2} = \frac{1 + \frac{Z_{22} - Z_{12}}{Z_s}}{1 + \frac{Z_{11} - Z_{21}}{Z_s}}.$$

To simulate a forced-current condition, I_1/I_2 needs to be 1. Two circumstances could satisfy this condition: 1. $Z_{22}-Z_{12}=Z_{11}-Z_{21}$, which leads to $Z_{11}=Z_{22}$ ($Z_{12}=Z_{21}$ in a passive network). This requires the self impedance of the coil to be the same, which is often not the case in asymmetric loading situations; 2. Let Z_s be much higher than $Z_{11}-Z_{21}$ and $Z_{22}-Z_{12}$. This can be achieved from the modeling.

Based the calculation above, it is better to use an ideal current source (one with infinite source impedance). At the same time however, it is known that a high impedance mismatch factor causes FDTD algorithm to converge slower [50, 51]. In FDTD algorithm, a source resistance helps dissipate the unwanted mode, thus reducing time steps required to converge. In a time-domain pulse excitation, the unwanted mode is introduced by the spectrum of the pulse; In a steady state excitation (frequency-domain), the unwanted mode is introduced by the starting of the pulse (from zero to the sine wave). In the case where $R=0$, or being too large, high percentage of the power is reflected from the circuit, and can only rely on lossy load and radiation to dissipate. So it is of interest to study quantitatively how high the source impedance needs to be in order to simulate FCE.

A Helmholtz pair breast coil at 7T is investigated here. Each loop has an inner diameter of 16 cm and an outer diameter of 17.2 cm, with a concentric RF shield of an outer diameter of 19.2 cm. Each loop has 12 breaks with the segmentation capacitor value of 11 pF. The shield has two breaks on opposite side with the segmentation capacitor value of 1800 pF. Each element in the Helmholtz pair is excited by a current source. The excitation current is set to be 1A for each source, and the actual current delivered to the loop is represented by I_1 and I_2 , respectively.

When there is no load present, the Helmholtz pair is a symmetrical structure. With a 50-ohm source impedance I_1/I_2 reaching 0.9996. However, when asymmetric load is present, much higher source impedance is required to maintain equal current. The asymmetric load is modeled the same way as in [52], where the thorax has a conductivity of 0.77 S/m, and a dielectric constant of 58.2, and the breast tissue has a conductivity of 0.04 S/m, and a dielectric constant of 5.64. The model is shown in Fig. 5

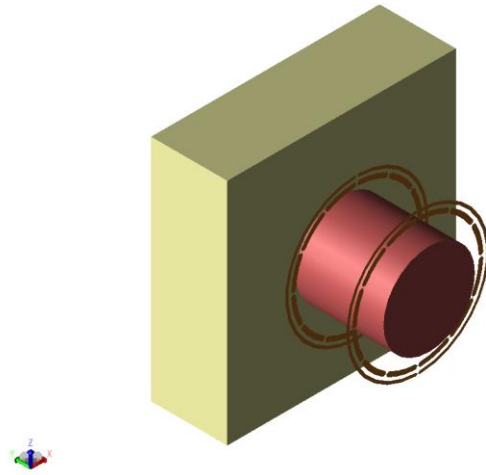


Fig. 5. A Helmholtz pair with fat (pink) and muscle (yellow) as loading. Modeled in XFDTD

Under asymmetric loading condition, varying the source impedance of the two current sources changes the ratio between I_1 and I_2 :

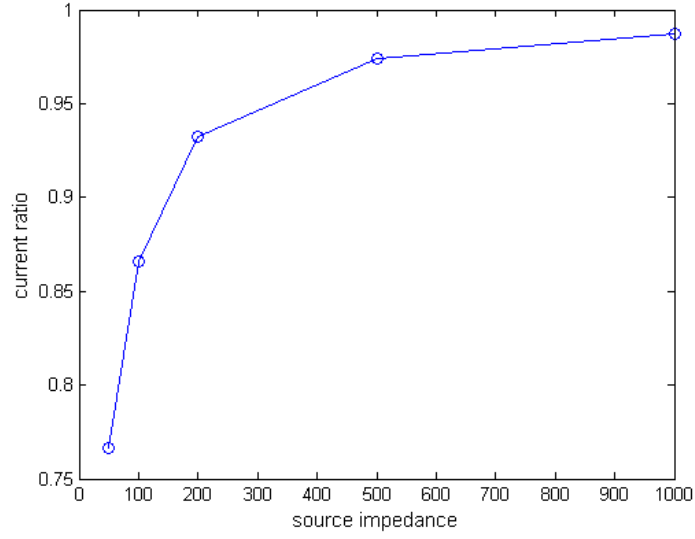


Fig. 6. Current ratio between I_1 and I_2 vs. current source impedance

As can be seen in Fig. 6, higher source impedance leads to higher agreement between I_1 and I_2 . In this case, a 1000-ohm source impedance is enough to maintain a current ratio of 0.98.

Ideally, an ideal current source should be used to represent a source impedance of infinity. However, such setup causes serious convergence issue in FDTD algorithm. The results in Fig. 7 underscores that problem of a high impedance mismatch factor.

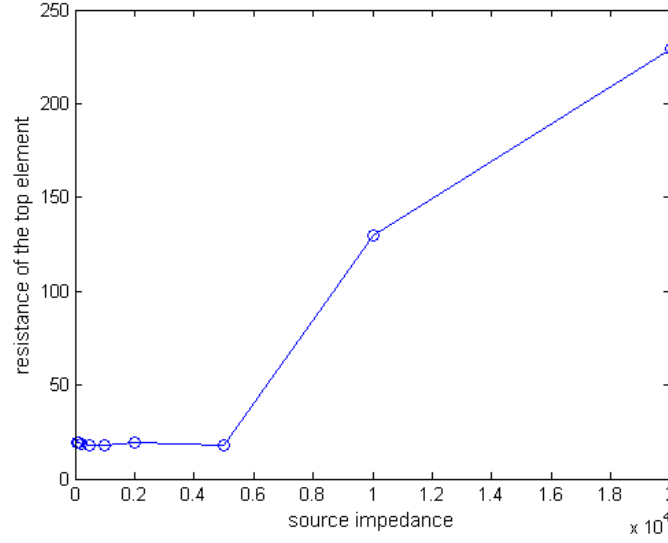


Fig. 7. Resistance of the top loop, after convergence vs. source impedance

A convergence factor of -40 dB was used in the simulation. Although the convergence detection routine found convergence for all simulation within the defined simulation time limit, the results achieved with source impedance larger than 10000 ohms are obviously wrong, considering the size of the coil. It indicates that a real convergence was not achieved within the given time. In this case, a 1000-ohm source impedance already satisfy our need, so there is no reason to go beyond that and reduce convergence rate.

In other cases where higher self-impedance is present, even higher source impedance might be required to minimize the $\frac{Z_{22} - Z_{12}}{Z_s}$ and $\frac{Z_{11} - Z_{21}}{Z_s}$ terms. The convergence issue will need to be carefully investigated, however.

3.4 Losses in FCE Coils

In most cases, coaxial cables used as the quarter-wave cables for the FCE coils are low loss cables. Their loss factor is in the range of 5~16 dB/100 m at the frequency of interest (298 MHz for 7T), therefore one would expect that the addition of these cables will not cause a significant change to $B_1/\sqrt{\text{input_power}}$ efficiency.

However, the above expectation assumes that the coil is matched before the coax. This unfortunately, is not true in our case. In the FCE configuration, the transmission lines are inserted between the coil elements and the matching network, inducing standing wave on the cables, which increases the loss from the cable.

In a transient view, the RF signal is reflected from the coil feed due to the mismatch. When the reflected wave reaches the matching circuit, the matching circuit reflects it back and put it in phase with the incident wave. This process continues until all power is consumed. Therefore, the wave effectively travels multiple times on the cable. The total loss in the cable can be quantitatively determined from the equation given by Pozar (2.94) [53]:

$$P_{\text{loss}} = P_{\text{in}} - P_L = \frac{|V_0|^2}{2Z_0} [(e^{2\alpha l} - 1) + |\Gamma|^2(1 - e^{-2\alpha l})]$$
$$P_L = \frac{|V_0|^2}{2Z_0} (1 - |\Gamma|^2)$$

Where P_{loss} is the loss occurred in the transmission line, and P_L is the power delivered to the load. As can be seen, the loss is determined by the attenuation of the cable,

as well as the reflection coefficient at the coil elements. The relationship between these factors can be plotted together:

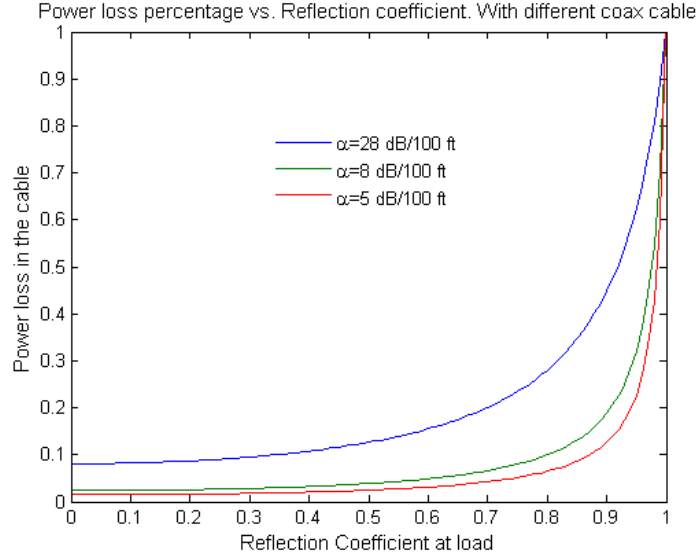


**Fig. 8. Power loss percentage vs. reflection coefficient and attenuation factor.
Length of the cable is 40 cm**

As shown in Fig. 8, a cable with lower loss have significantly lower total loss than a cable with higher loss. As the reflection coefficient goes up, the power loss increases- In the extreme case where all power is reflected at the coil, all power is lost on the cable. In a well-matched case (reflection coefficient smaller than 0.1), minimal power loss is observed, as is predicted previously.

Reflection coefficient is ultimately determined by the coil impedance. In the case where the coil has low resistance and that the impedance is close to the wall of the Smith chart, the FCE loss could be the dominating component in the total loss. However, in cases

where the coil impedance is closer to the center of the smith chart, the loss from FCE cables is may not be significant compared to the loss from the coil itself.

As a conclusion, using FCE introduces additional loss from the standing wave on the transmission line. The loss is related to the coil impedance. When coil impedance is naturally matched to 50 ohm or close, the loss will be minimal. However, when the coil impedance causes high reflection at the feed, the loss is substantial. This disadvantage makes FCE a valid option for transmit, when there is enough transmit power. It is not recommended to use FCE as receive, as it will degrade SNR due to this loss.

There are ways that can potentially reduce the FCE-induced loss. Based on the calculation, the loss increases with 1. Cable length; 2. Attenuation of the transmission line; 3. The reflection coefficient at the element feed. Using a cable with lower loss could reduce the attenuation rate; Partially matching the element before the transmission line could reduce the reflection coefficient. However, to maintain the FCE function no shunt element should be used for matching; The use of lumped element to replace transmission lines also has the potential to reduce loss, but a high quality-factor component is required.

3.5 Detuning FCE Coils

FCE uses odd multiples of quarter-wave transmission lines ($\lambda/4$ T.L.s) to excite elements through a common-voltage point (CVP). The coil elements are fed directly by the $\lambda/4$ T.L.s without a tuning capacitor at the feed point.

Many decoupling methods are designed to create an open-circuit at the coil feed to reduce induced current, such as the use of current source amplifiers [47] and the low-

output impedance power amplifier [48]. The most classic implementation of this method is the use of low-input impedance preamplifiers on receive arrays [36]. The use of $\lambda/4$ T.L.s in the FCE configuration gives us a straight forward way to for decoupling: Having a PIN diode at the CVP controlled by a DC biasing signal. According to transmission line theory, a short circuit will be transformed to an open circuit by a $\lambda/4$ T.L. When forward-biased, the PIN diode creates a short circuit at CVP, which is then transformed into an open-circuit at the coil element by the FCE feed lines. A simple experiment was used to validate this, as is depicted in Fig. 9:

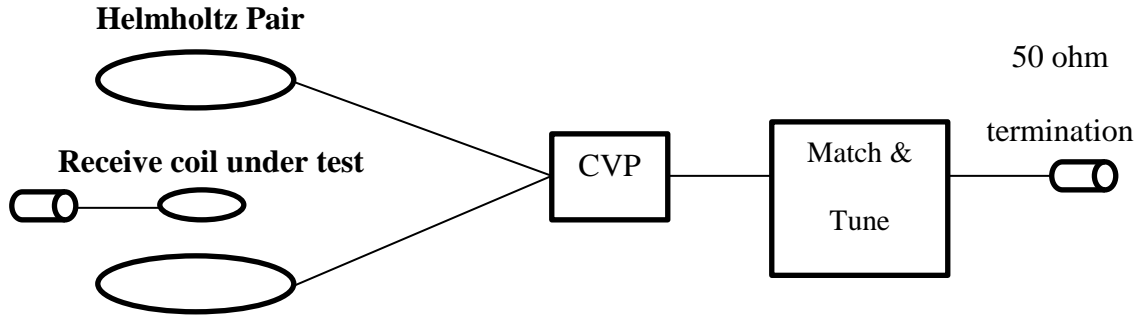


Fig. 9. Detuning test setup

A test receive coil was inserted between a Helmholtz pair transmit coil. Its return loss curve was compared in Fig. 10 with the PIN diode on the CVP turned on and off.

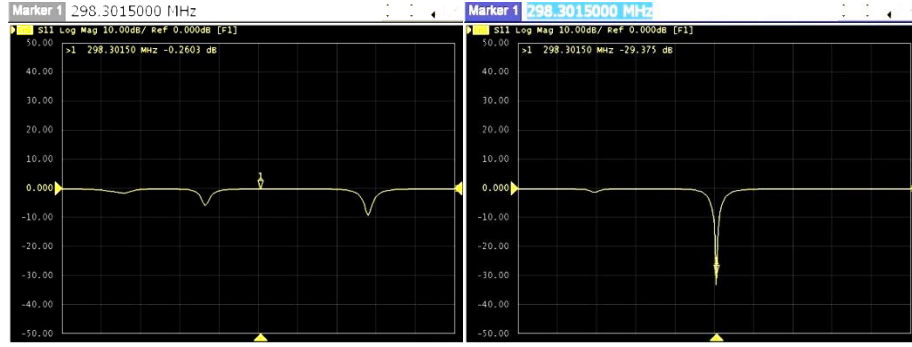


Fig. 10. S11 of receive coil, Left: PIN diode reverse biased (12V) (frequency span: 50 MHz). Right: PIN diode forward biased (100 mA)

When the PIN diode is reverse biased, there is an obvious mode split across the frequency span (50 MHz), which is a clear indication of coupling [41]. When the PIN diode is forward-biased, the mode splitting was degenerated into one mode resonance, indicating successful detuning of the coil.

The idea of this detuning method in FCE driven coils have been implemented in a quadrature unilateral breast coil at 7T used for transmission only (with a 16 channel receive array insert) [52].

3.6 FCE with Switchable Field of View

As stated in section 3.4, the FCE method brings extra loss to the system, and the loss is dependent on the reflection from the coil, therefore it is very important to preserve the power efficiency wherever possible. A switchable FOV design will allow more concentrated power when needed. Meanwhile, a switchable FOV coil can also avoid unnecessary heat deposition into other part of the body, when desired.

With the detuning capability of the FCE coil explained in section 3.5, it is realized that a reconfigurable-FOV design can be implemented based on that. At the CVP, a PIN diode can be put in series with the RF signal to control the flow of RF. If an element in the array is unwanted, this can be done to prevent the RF being injected into that element. However, this alone will not decouple that element from the system. Because of the close distance between elements in our coil configurations, mutual coupling between them will still put power onto the unwanted element.

Therefore, a shunt PIN diode needs to be added to the CVP, to actively detune the unwanted element, as is done in section 3.4. Biasing of the two diodes (a series and a shunt) requires careful design of the biasing network, which will be discussed in detail in the next chapters.

CHAPTER IV

FCE BILATERAL BREAST COIL AT 7T*

4.1 Introduction

Breast MRI is challenging due to two major reasons: 1. The electrical property of the chest, which is mainly composed of muscle, is very different from that of the breast, which is a combination of fiber glandular tissue and fat tissue. This causes asymmetric loading in the Anterior-Posterior (A-P) direction; 2. It is impossible to use a birdcage-like structure in breast imaging, and therefore the design of a breast RF coil typically involves the use of multiple elements. Closely-spaced elements have heavy mutual coupling, which complicates the tuning, and causes unpredictable current distribution.

In [52], FCE was used on a 7T unilateral breast coil. The method was shown to alleviate the asymmetric loading issue and create a homogeneous field pattern.

A bilateral study is of higher clinical value due to easier clinical planning and interpretation of result, and therefore a bilateral coil is desirable. A bilateral coil requires even more elements to be used, and suffers from high mutual coupling between these elements. The use of FCE on a bilateral coil is investigated in this chapter. It was acknowledged that FCE brings extra loss through its feeding network, and therefore in applications that need very high peak power [33] (e.g proton-decoupled spectroscopy, CEST-MRI), it is necessary to enable a unilateral mode which saves half of the power and

*© [2015] IEEE, Reprinted, with permission, from [Jiaming Cui, John C. Bosshard. C, Joseph V. Rispoli, Ivan E. Dimitrov, Sergey Cheshkov, Mary Preston McDougal, Craig Malloy, Steven M. Wright, A Switched-Mode Breast Coil for 7 T MRI Using Forced-Current Excitation. *IEEE Transactions on Biomedical Engineering.*, 07/2015].

enables higher $B_1/\sqrt{\text{input_power}}$ efficiency. Therefore, the FCE with switchable FOV method is of high value in breast imaging. In this chapter, several coils and methodologies are discussed. In section 4.2, a switched-mode bilateral breast coil is designed for 7T [54, 55]. The coil employs FCE and can switch between unilateral and bilateral mode electronically. The bilateral mode has large FOV while the unilateral mode provides higher power efficiency; In section 4.3, a modified version is implemented specifically for bilateral transmission that allows high channel receive array integration [56]; One problem for the switchable FOV design is the require of retuning when switching modes, especially between bilateral and unilateral mode. In section 4.4, a potential method that can partially address that problem, is presented. A test coil was tested on bench for proof of concept, and positive results are obtained.

4.2 Switched-mode Bilateral Breast Coil at 7T

4.2.1 Introduction

As is described in chapter two, efforts have been made to translate existing MR technologies to 7T to capitalize on the improved sensitivity and signal-to-noise ratio (SNR) [24, 57-60]. Several clinical 7T breast studies have demonstrated the feasibility and the advantage of utilizing high field [58, 61-66]. Operating at high fields, however, presents a number of engineering challenges. Transmitting at a higher Larmor frequency creates a shorter radio frequency (RF) wavelength in the body, often resulting in B_1

inhomogeneity and non-uniform sensitivity [26, 67, 68]. When designing high field coils with multiple elements, the shorter RF wavelength also causes more complex element-to-element interactions, complicating coil tuning. A number of research groups have employed parallel RF transmission to address the high field inhomogeneity problem [29, 69-72]. This method utilizes multiple transmit channels, individually controlling the current on each coil element, to achieve a uniform excitation. However, the high channel count needed to implement this technique is often expensive and available at a few research sites only, hence single-channel techniques are still needed. In the past, our group has successfully applied the FCE method on high field multi-element coil designs to obtain some of the advantages of a two-channel transmitter at much lower complexity and cost. The FCE technique exploits transmission line properties to ensure that equal currents are delivered to the feedpoints of all elements [45]. This approach has been shown to mitigate inhomogeneity arising from the asymmetric coil loading encountered in breast imaging [73].

In clinical practice, a bilateral study is preferred as it simplifies planning and interpretation of the results [32, 66, 74, 75]. Comparing images from both breasts can reduce false positive detection in dynamic contrast enhancement (DCE)-MRI. Additionally, studies indicate that in women recently diagnosed with unilateral breast cancer, additional cancer lesions are sometimes detected in the contralateral breast [76]. Several 7T breast studies have indicated a need for bilateral coil design [63, 66]. On the other hand, in some applications, e.g., proton decoupling in second-nuclei applications, a unilateral coil may be preferred, since it enables judicious use of the available total proton

decoupling power in a single breast [33, 77, 78]. Our group has reported a unilateral, quadrature FCE breast coil previously [73]. Here, we describe the extension of the unilateral coil to a new switched-mode coil. The new coil can be configured for either bilateral operation or unilateral operation for either breast. By extending the FCE approach to both sides of the array, the mutual impedance between the left and right arrays is also mitigated, eliminating potential asymmetries caused by mode splitting. The switched-mode coil was evaluated on the bench and through MRI experiments in its different configurations. Efficiency comparison was made on bench with the previously reported unilateral coil.

4.2.2 Coil Design

In designing the switched-mode coil, we initially duplicated a previous unilateral coil construct [73] and added a switching network to enable selectable bilateral and unilateral (left/right) operation. The switching network was designed to enforce the FCE condition in all modes. All coil conductors were etched from copper-clad FR-4 PCB.

Each quadrature unilateral coil consisted of a Helmholtz pair and a saddle pair, as previously described in [73]. In brief, the two identical loops comprising the Helmholtz pair had 16 cm i.d. and 17.2 cm o.d and were coaxially separated by 8 cm in the vertical y-direction. Each element was segmented by eleven 10 pF capacitors. A concentric coplanar shield surrounded each loop, with 18 cm i.d. and 18.7 cm o.d; the addition of coplanar shields has been shown to reduce E-field radiation from the coil [73]. To prevent eddy currents, each shield was segmented in two locations by 1800 pF capacitors. The saddle pair coils were affixed on opposite sides of a 15.2 cm i.d. acrylic tube and centered

inside the Helmholtz pairs. The elements were rectangular with inner measurements (when flat) of 15.3 cm width and 8.1 cm height and outer measurements of 16.5 cm width and 9.4 cm height. When mounted at radius 7.6 cm, each saddle produced an angular aperture of 120° . Analogous to the coplanar shields on the Helmholtz elements, rectangular shielding conductors of 0.4 cm width were spaced 0.5 cm outside of the saddles. Each coil element was segmented by eleven 12 pF capacitors, and the shield was segmented at two locations by 1800 pF capacitors.

To enable bilateral operation, the unilateral coil was duplicated and the two coils were spaced 19.2 cm, center-to-center in the x direction. In this paper, we define the term “left coil” as the coil used to image the left breast of a patient ($-x$), and “right coil” as the coil to image the right breast ($+x$). Photographs of the coil are shown in Fig. 11



Fig. 11. Switchable bilateral quadrature coil closed in a housing (left) and with covers removed (right) forms

The close proximity of the two quadrature coils raised concerns of potential B_1 field cancellation in the bilateral configuration. Two 4feeding schemes were available: with the B_1 field having the same direction (Fig. 12 (a)); with the B_1 field having the opposite direction (Fig. 12 (b)). The first arrangement provided better SNR in simulations and was chosen for the final design.

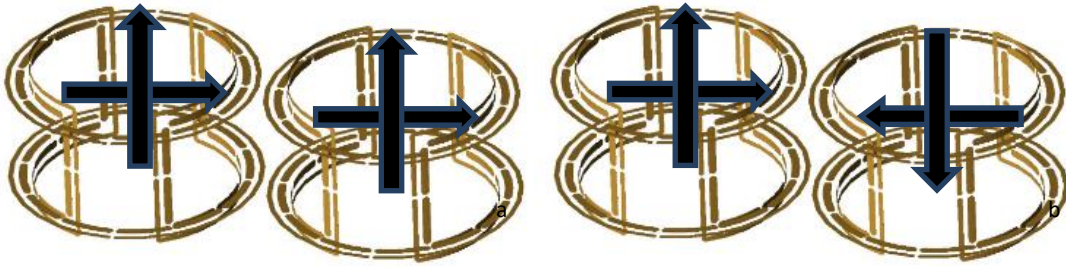


Fig. 12. Possible quadrature B_1 field arrangements (a): with the B_1 fields in the same direction; (b): with the B_1 fields in opposite directions. The arrangement on the left was chosen based on numerical simulations.

4.2.3 Forced-Current Excitation and Mode Switching

The theory behind the FCE method has been explained in the previous sections. In brief, in a single-channel multi-element array design, the elements are connected to a common voltage point (CVP) through quarter-wavelength transmission lines. The resulting current at the feed point of each element is equal despite differences in loading and mutual impedance between elements [79]. In this coil, all four elements in the two Helmholtz pairs were connected to one CVP through quarter-wavelength segments of

semi-rigid coaxial cable, and all four elements in the two saddle pairs were connected to a second CVP using the same method.

The circuit boards for the CVP included PIN diode switching networks allowing unilateral/bilateral mode selection. Four operating modes were possible: Both coils activated (bilateral mode, mode 1); Left coil activated with right coil detuned (mode 2); Right coil activated with left coil detuned (mode 3); Both coils detuned (mode 4). Modes 1-3 were utilized for Transmit/Receive configurations, and mode 4 was included for potential future use with receive array inserts. To control mode switching of the two coils, we assembled a power supply switching device to provide two DC supply signals which can be switched between +12 V and -12 V; positive polarity activates the corresponding coil whereas negative polarity effectively disconnects and detunes the coil.

A simplified schematic of the switching circuit with coil connections is presented in Fig. 13. RF chokes on the DC bias lines and current limiting resistors are omitted for clarity.

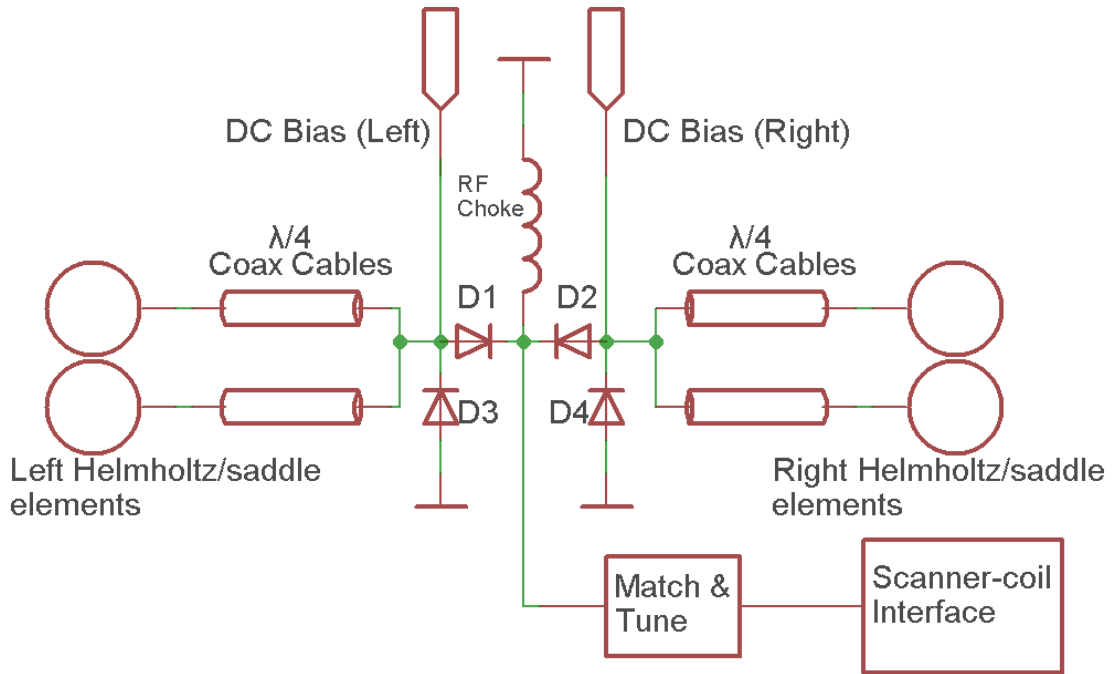


Fig. 13. Schematic of switching network for operating mode control of the Helmholtz/saddle pairs. The same DC signals for switching are routed to the Helmholtz and saddle switching network.

The path for the RF is determined by the status of PIN diodes D1 and D2 (UM9415, Microsemi, Lowell, MA, USA). A +12V/-12V signal forward/reverse biases D1 or D2, which connects/disconnects the corresponding coil elements to/from the RF chain. In unilateral mode, it is necessary to detune the non-active coil. The FCE implementation provides a straightforward method to detune a coil: when D1 or D2 is reverse-biased, D3 or D4 is forward-biased by the same DC signal, essentially creating a short circuit at the CVP. According to transmission line theory, the quarter-wavelength coaxial lines transform the short circuit to an open circuit at the feed of the coil elements, consequently detuning those elements. When D1 or D2 is forward-biased, D3 or D4 is reverse-biased by the same DC signal and does not affect the RF chain. The switching network is followed

by a single match/tune board after which the matched coil is connected directly to one port of the scanner quadrature coil interface box, which provides the RF preamplifier and Transmit/Receive switching. The apparatus and signal paths shown in Fig. 13 is duplicated for the other set of coils (Helmholtz or saddles).

To summarize, by combining the FCE method and the diode switching network, equal current is forced at the coil elements within the same coil (modes 1-3), as well as the left and right coils (mode 1). In mode 2 and 3, the unused coil is detuned.

Because the quarter-wavelength coaxial lines connecting the left and right elements to the CVP boards share a common ground at the boards, upon implementing the bilateral design the shields of these cables were found to support additional half-wavelength dipole modes, which degraded performance and affected left-right symmetry. These cable modes were largely mitigated by placing two identical, parallel copper shields in the transverse plane, superior and inferior to the coils, spaced 1 cm from the outer conductors. Each shield has dimensions of 40.7 cm (x) by 10.3 cm (y). The shields were segmented along the x- and y-directions to mitigate the effect of eddy currents, with four evenly spaced y-directed cuts, and one central x-directed cut which skips the middle area where the switching circuit boards were mounted.

4.2.4 Electromagnetic Modeling

FDTD simulation software (Xfdtd 7.4, Remcom, State College, PA, USA) was used to perform electromagnetic simulation to calculate B_1 and Specific Absorption Rate (SAR) generated by the coil. The phantom previously utilized in [73] was used for comparison purposes. This phantom included a cylinder consisting of breast fat material

($\sigma = 0.033$ S/m and $\epsilon_r = 5.54$) and a rectangular block consisting muscle material ($\sigma = 0.77$ S/m and $\epsilon_r = 58.2$). The dielectric properties of the different materials were obtained from [80]. The coil was simulated in modes 1-3. For each mode, the active coil elements were fed with high impedance (1000 ohm), 1 A steady-state current sources to simulate the FCE drive condition. 0 and 90 degree phase offsets were added to the Helmholtz and saddle feeds, respectively, to create quadrature excitation. The non-active coil elements in mode 2-3 are left open circuited at their feed points.

The 3D model of the coil and breast phantom is shown in Fig. 14. B_1 field maps and 10g averaged SAR maps at the Larmor frequency (298.03 MHz at 7 T MRI) were obtained in the central axial plane in mode 1-3, and are shown in Fig. 15. All modes had 1 watt total power applied.

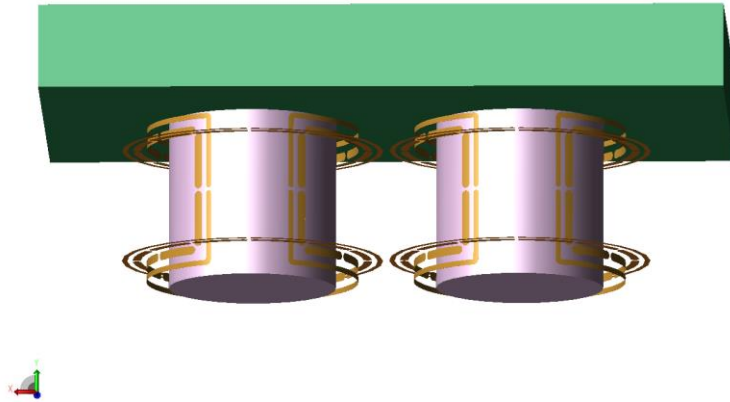


Fig. 14. Coil and phantom model. The RF shields are not shown for clarity

As expected, higher B_1 as well as SAR are generated in the active coil in unilateral mode as compared to bilateral mode for the same amount of input power. The B_1 in the non-active coil in unilateral mode is suppressed by approximately 20 dB as compared to the active coil. In all three modes, highest SAR is observed in the chest wall.

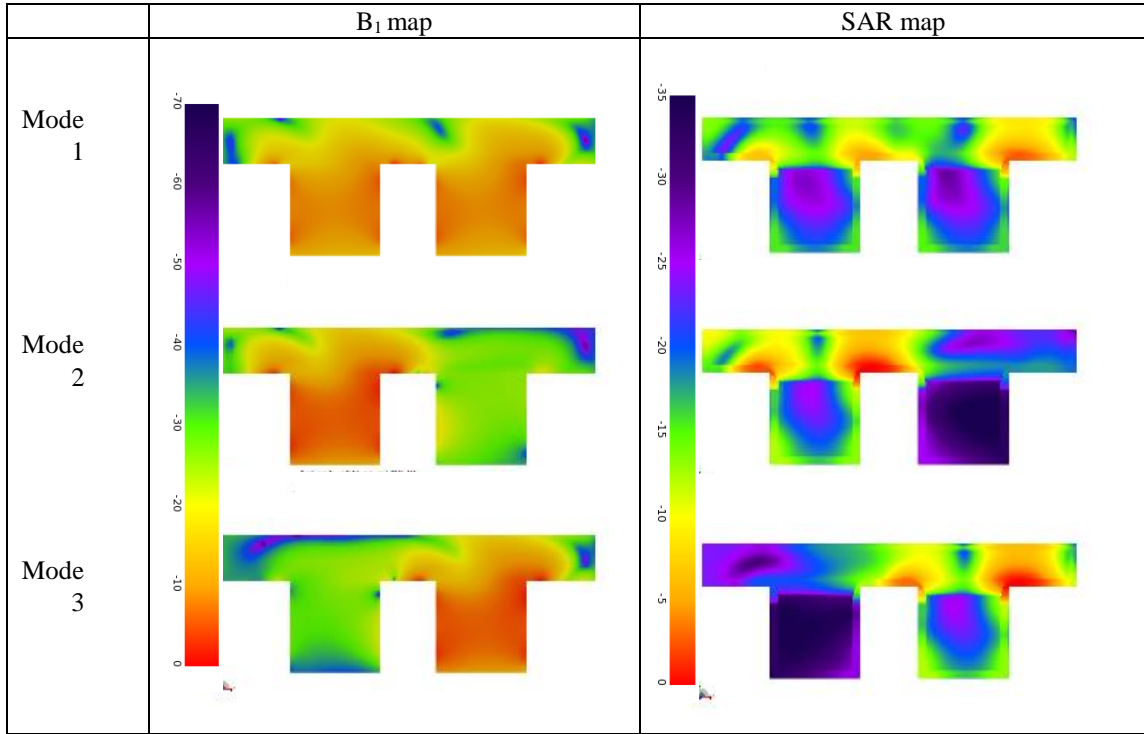


Fig. 15. Central axial plane B_1 and 10g averaged SAR maps in modes 1-3. The results were scaled to 1W total input power to the coil. 0 dB corresponds to 1.97 μ T and 0.99W/kg in the B_1 and SAR maps, respectively.

In unilateral mode the unused coil is detuned and does not produce significant SAR, therefore the $B_1/\sqrt{\text{total_SAR}}$ is higher in unilateral mode. This is useful in cases where the peak power or total SAR is limited. Accordingly, the SNR is also higher in

unilateral mode, by reciprocity. Of course, since the left and right coils are identical, $B_1/\sqrt{\text{SAR}_{10g_max}}$, was found to be very close (within 0.3 dB) in the active coil for all three modes. Thus the mode does not change peak SAR performance. Therefore, enabling the unilateral mode may be advantageous in applications like proton decoupling if the peak available power is limited.

4.2.5 Coil Testing - Bench Measurements

The $B_1/\sqrt{\text{input_power}}$ efficiency of the switched-mode coil was initially evaluated on the bench in all three modes. A prototype Helmholtz pair bilateral coil was also tested on bench to analyze the effect of FCE on tuning and homogeneity.

FCE vs. non-FCE performance

When the switched-mode coil operates in bilateral mode, the coupling between the two closely spaced quadrature coils creates multiple modes with different relative current amplitudes and phases in the elements. This complicates the coil tuning and affects the field homogeneity. To evaluate the impact of using the FCE method in such a scenario, a prototype Helmholtz pair bilateral coil with slightly smaller dimensions (14.8 cm i.d for each coil) was tested on the bench. FCE vs. non-FCE performance was evaluated. In the non-FCE case, $3\lambda/8$ coax cables, instead of $\lambda/4$ were used to excite the Helmholtz pair elements after the CVP. The following comparison data was collected: 1) S_{11} response of the bilateral coil over a 50 MHz span centered at 298 MHz; 2) Field profiles at 298 MHz along the central axis in the left coil using a shielded pickup loop; 3) Field strength measured as the S_{21} response between the coil and the same pickup loop located at +1 cm on the central axis of the left coil (0 cm represents the isocenter of the coil, and positive

values represent positions towards the bottom of the coil), over a 50 MHz span centered at 298 MHz;

The FCE vs. non FCE performance was evaluated on the prototype Helmholtz pair bilateral coil. In both cases, the coil was tuned to 50 ohm at 298 MHz-the resonance frequency at 7 T. The S_{11} response of the bilateral coil, the field profile along the central axis of the left coil at 298 MHz measured with a pickup loop, and the S_{21} between the coil and the pickup loop located at +1 cm on the central axis of the left coil, was recorded and compared for the two cases, as shown in Fig. 16.

In the FCE case, presented with blue curves and symbols, the coil behaves well despite the presence of four closely-coupled elements: the S_{11} response shows a single mode in the span (a), the field profile is uniform indicative of equal currents in the elements (b), and the response peaks at the desired frequency (c). In the non-FCE case, the S_{11} response indicates the presence of multiple modes. Since the coil elements are not tuned independently and equal currents are not enforced, the resulting field profile (b) is highly inhomogeneous. The $3\lambda/8$ feedlines (non-FCE condition) did not ensure equal currents, and indeed represented a “free” voltage excitation case in which the mutual impedance between elements must be accounted for to ensure operation in the proper mode [81]. In this case, that would require more degrees of freedom in tuning the coil than just a single matching network. This behavior is reflected in the rapidly varying field intensity with frequency in the non-FCE mode shown in Fig. 16(c).

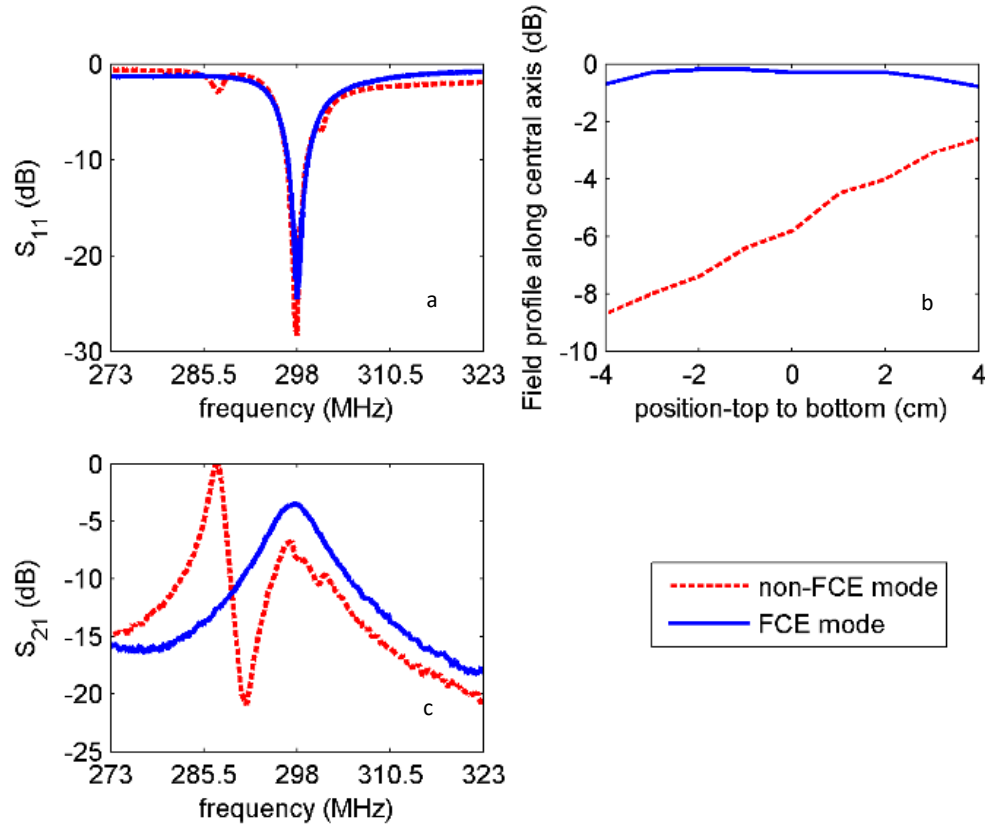


Fig. 16. Comparison between FCE mode and non-FCE mode. (a) S₁₁ of the bilateral coil over a 50 MHz span, good matching was achieved at the coil port for both cases; (b) Normalized field profiles along the central axis of the left coil at 298 MHz, presented in decibels. In non-FCE mode the coil exhibits field inhomogeneity even when unloaded due to capacitor tolerances in the elements, both of which are connected to a common tune capacitor. When operated in FCE mode, the coil shows much better homogeneity; (c) Normalized S₂₁ over a 50 MHz span at +1 cm on the central axis of the left coil. When operated in FCE mode, the desired mode (equal currents) appears at 298 MHz, giving a uniform field plot. When operated in non-FCE mode, the coil shows a more complex mode structure, and does not provide equal currents in the coil elements resulting in an inhomogeneous field.

Switched mode coil-efficiency comparison of the three modes

As discussed above, one potential advantage of allowing unilateral operation on the switched-mode coil is higher power efficiency over the bilateral mode. The incoming

RF signal, as represented in Fig. 13, should divide evenly into the two coils in bilateral mode owing to the symmetric circuit structure. When switching from bilateral mode to unilateral mode, the input power flows into the active coil only and a 3dB higher $B_1/\sqrt{\text{input_power}}$ efficiency is expected. To evaluate the coil efficiency in modes 1-3 (bilateral, unilateral-right only, unilateral-left only), the Helmholtz pairs and saddle pairs were tuned to 50 ohms at their feedpoints and excited in quadrature mode. One dimensional field profiles were measured along the x axis through both coils using a measurement system dedicated for RF coil characterization [82] and a quadrature shielded pickup loop. The measurements were repeated for modes 1-3 and the B_1 profiles were plotted together to compare efficiency. To fully evaluate the coil performance under potential coupling between the multiple elements, the coil was tested unloaded where the highest quality factor was achieved. Additionally, the insertion loss of the switching circuit was measured to evaluate the effect of the diodes in the RF path. The impact of such loss on the coil was then evaluated on bench by comparing the efficiency of the coil in unilateral mode to the purely unilateral coil described earlier[73].

The B_1 profiles of the switched-mode coil operating in modes 1-3 are plotted in Fig. 17. In unilateral mode (mode 2, 3), the inactive coil was detuned. Since the two coils were closely spaced, the active coil has some sensitivity over the region within the detuned coil. This detected residual signal decreases towards the outer edge of the detuned coil and is primarily due to the natural sensitivity of the “on” coil, as shown below.

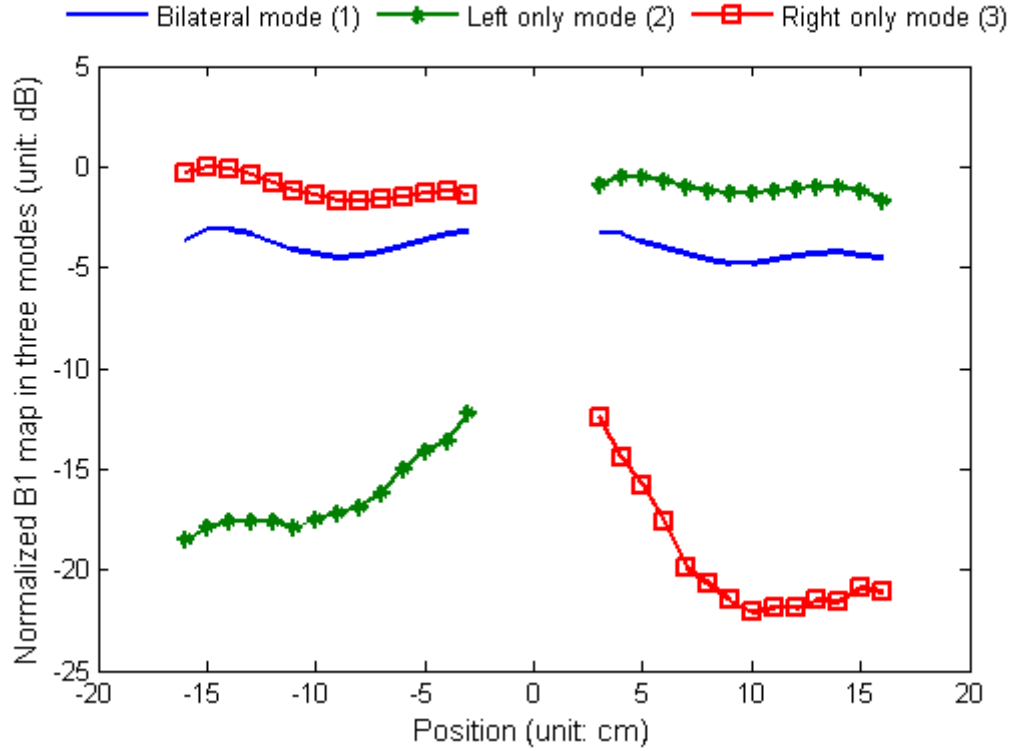


Fig. 17. One dimensional B_1 profiles across the ROI, along x direction. The data measured in modes 1-3 are normalized to a global maximum and plotted together for comparison. When operated in unilateral mode, the active coil has around 3 dB higher sensitivity than when operated in bilateral mode. The non-active coil has much lower sensitivity (9-20 dB lower than the active coil), which indicates successful detuning.

When switching from bilateral mode to unilateral mode, a 1.8-3.5 dB increase in $B_1/\sqrt{\text{input_power}}$ efficiency was observed within the activated coil, with an increase of approximately 3 dB at the central region of the coil. Enforcing equal currents in the left and right coils results in symmetric fields despite high mutual impedance between the two coils and slight differences in components and the fabrication process. When operated in unilateral mode, the non-active coil has 9-20 dB lower sensitivity than the active coil.

The insertion loss of the switching circuit was found to be 0.6 dB at 298 MHz, which is mainly caused by the series diodes. The power efficiency of the switched-mode coil in unilateral mode was measured to be 0.6 dB (13%) worse than that of the purely unilateral coil, which does not have the diode switching circuit.

4.2.6 Coil Testing - MRI Experiments

The switched-mode coil performance was evaluated on a whole-body 7 T scanner (Achieva, Philips Medical Systems).

The phantom was constructed out of a container shaped as a tapered cylinder, 13.4 cm diameter at the top decreasing to 10.8 cm diameter at the bottom. Two such containers were filled with canola oil to mimic lipid properties of the breast and were placed inside the two quadrature coils, with the top of the phantom container at 1 cm above the top Helmholtz loop.

Phantom images were acquired in coil modes 1-3. The coil efficiencies of modes 1-3 were compared by recording the peak transmit drive scale required to achieve a 90 degree tip angle over a rectangular region in the center of the phantom.

Phantom images were acquired with the switched-mode coil. All images were acquired with a same set of scan parameters and the same phantoms. Fig. 18(a)-(c) are the images acquired with the switched-mode coil in the three modes (For a discussion of the *in vivo* images, please see the next section). When the switched-mode coil operates in unilateral mode (modes 2-3), the residual signal received by the detuned coil was predominantly suppressed, with the maximum signal in that region only 10% of that in the

active coil. This is consistent with the bench results in Fig. 17. It is evident that the inactive coil in the switched mode coil is effectively detuned by the switching network.

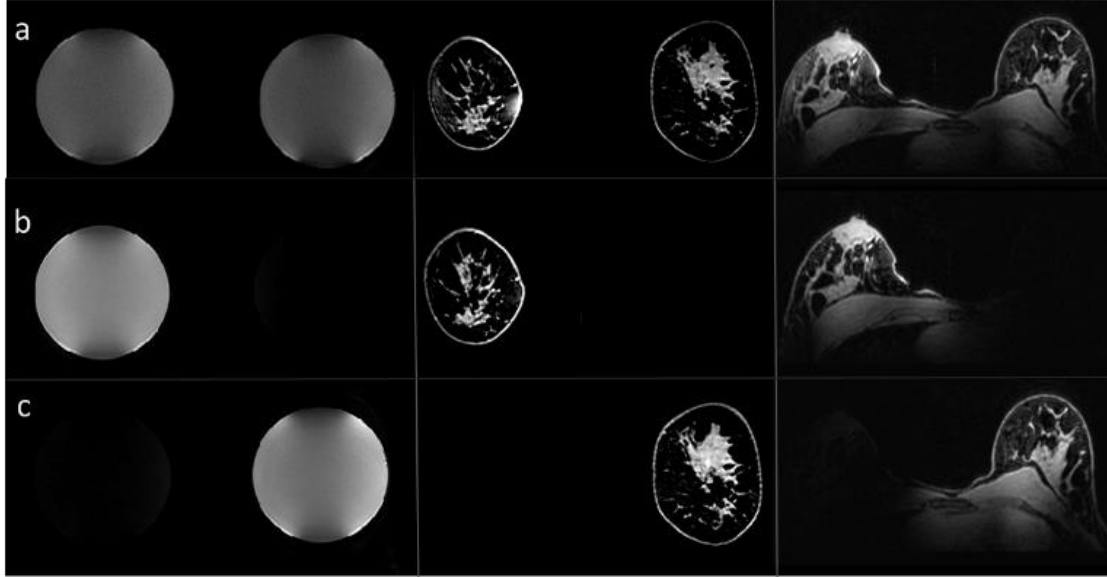


Fig. 18. Coil mode performance as illustrated by phantom and *in vivo* imaging: (a, top row) switched-mode coil: bilateral mode; (b) switched-mode coil: right only mode; (c) switched-mode: left only mode. Original *in vivo* acquisition (coronal) and reconstructed (axial) images are shown in the middle and right columns, respectively. Symmetric performance is observed in the bilateral mode, while excellent signal localization is seen in the unilateral modes.

On the 7 T Philips Achieva scanner, the output voltage of the power amplifier is linearly proportional to the transmitter drive scale, so the output power is proportional to the square of the drive scale. The drive scale (DS) for a 90 degree tip angle using the switched-mode coil was recorded during the transmit gain calibration phase in modes 1-3 is shown in Table 1, along with relative output power of each case, scaled to 0 dB for the bilateral mode 1. The coil was also compared on the bench by measuring the S_{21} between the coil and a pickup loop in the center of the active coil in all modes. In each case the coil

was tuned to 50 ohms, and the power required to obtain the same field strength at the pickup loop was recorded and scaled to the result of mode 1. The bench result is consistent with the MR measurements.

Table 1 Transmitter (TX) drive scale (DS), transmitter relative output power, and bench measurement of the three modes

Mode	TX	TX	Bench
Bilateral-Mode	0.512	0 dB	0 dB
Left only-Mode	0.352	-3.3 dB	-3.5 dB
Right only-	0.334	-3.7 dB	-3.2 dB

The results in Table 1 demonstrate that the switched-mode coil, when in unilateral mode, is approximately twice as efficient as its bilateral mode, which may be useful for certain applications, such as chemical exchange saturation transfer (CEST) or proton decoupling, that requires high transmit field intensity.

To test coil performance two volunteers with different breast cup size were scanned under an Internal Review Board approved protocol and after signing an informed consent. *In vivo* bilateral coverage and fat suppression uniformity were tested by acquiring coronal 3D T1-weighted fast gradient echo (THRIVE) images with and without fat suppression. Additional *in vivo* imaging parameters were as follow: FOV 370 x 285 x 150 mm (RL x FH x AP), resolution 1 x 1 x 1 mm (overcontiguous), TR/TE/FA: 4.0 ms/1.6 ms/8°, SPAIR with TI = 150 ms (for fat saturation), partial Fourier acquisition of 0.7 (halfscan) in the first phase encoding direction, for a total scan time of 1:22 minutes (no

fat saturation) and 3:44 minutes (with fat saturation). The original coronal images were also reconstructed in the axial plane as 1-mm projections. Coil excitation homogeneity was evaluated using B_1 mapping with a dual TR acquisition [83] with nominal flip angle of 50 degrees, $TR_1 / TR_2 = 35 / 140$ ms, and resolution $3 \times 3 \times 2$ mm³.

Like the phantom experiments, *in vivo* images were acquired with the switched-mode coil in all three modes, Fig. 18. Original *in vivo* acquisition (coronal) and reconstructed (axial) fat-suppressed images are shown in the middle and right columns, respectively. Excellent signal localization is seen in the unilateral modes, with less than 10% of the signal being excited in the non-enabled coil. Fig. 19 shows *in vivo* images in bilateral mode with and without fat suppression (top and middle rows, respectively). While the volunteers presented different breast cup sizes (left: C/D, right: A/B), the bilateral mode produced uniform excitation, as seen from the images and from the B_1 field maps (bottom row). The volunteer *in vivo* images demonstrate good bilateral coverage and uniform fat suppression. Good coverage of the chest wall and the axilla is also seen.

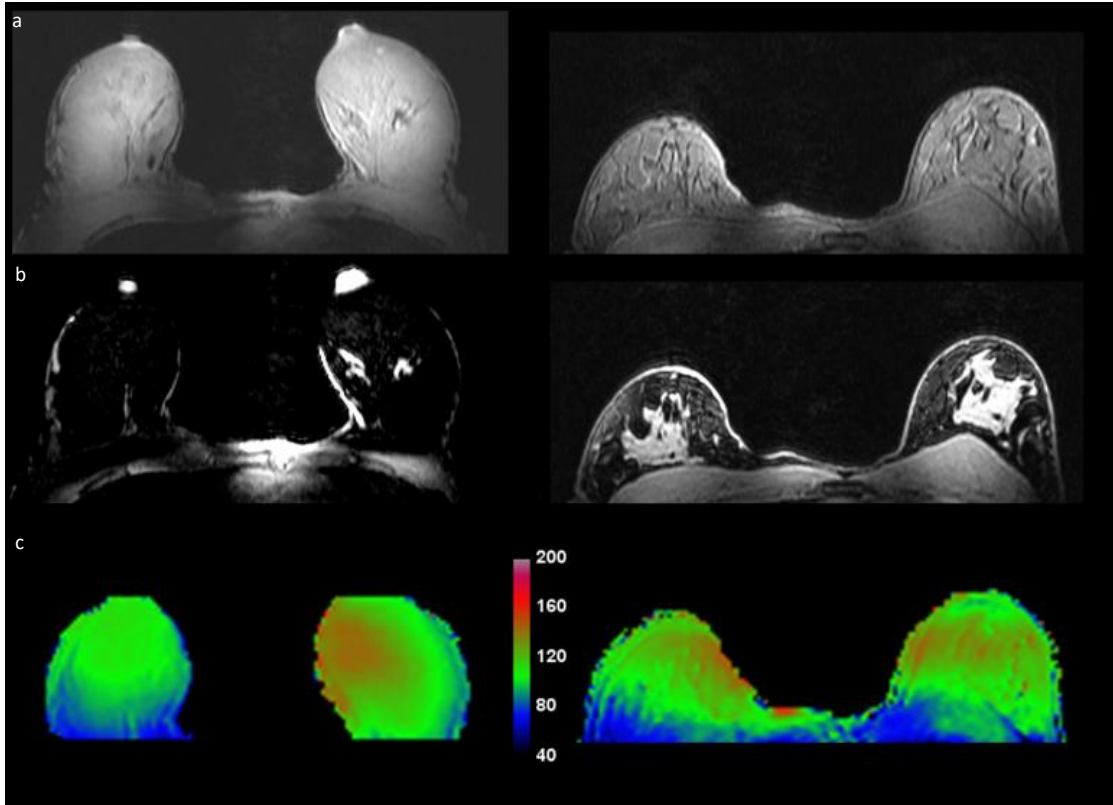


Fig. 19. (a./b.) In vivo 3D THRIVE images (first two rows, with and without fat suppression, respectively) in bilateral mode demonstrate coil performance for varying breast sizes. Good coverage of both breasts and the chest wall is seen, along with uniform fat suppression attesting to the transmission homogeneity of the coil. (c.) Flip angle maps demonstrate sufficient homogeneous excitation over the bilateral FOV.

4.2.7 Summary

At 7T, forced current excitation is one approach to overcoming B_1 inhomogeneity as demonstrated in a unilateral breast coil [73]. Since clinical breast imaging requires a bilateral coil, the use of FCE was extended to the operation of two unilateral coils simultaneously, or individually. A switched-mode coil operated at 7T introduces significant challenges due to the high coupling between two closely-spaced unilateral quadrature coils when operated simultaneously. This coupling will introduce additional

unwanted modes, making it difficult to ensure operation in the desired mode and with the desired current distribution. In addition, it is desirable to have a coil that is relatively insensitive to the uneven and variable coil loading presented by the general population. By using the FCE method, the current at feed points of each coil element was forced to be equal within the same coil, as well as the left and right coils (when operated in bilateral mode). This addresses the complication in tuning a multi-element coil and achieves better field homogeneity. The switched-mode performance was also evaluated. Bench measurements and MR experiments largely agreed and indicated that the switched-mode coil is around 3 dB more efficient in unilateral mode than bilateral mode. This advantage in power efficiency has the potential to facilitate high-power applications such as proton-decoupled second-nuclei applications. In vivo breast imaging in the bilateral mode demonstrated good bilateral coverage and uniform fat suppression, which are both required for clinical research studies.

4.3 Modified Bilateral Breast Coil for Receive Array Insert at 7T

4.3.1 Introduction

A quadrature unilateral breast coil for 7T has been reported previously [52]. The coil employed FCE method to mitigate effects due to asymmetric loading, producing a homogeneous field pattern. This made the coil an excellent choice for use as a transmit coil with receive array insert, which was implemented and tested together with a 16 channel receive array [84]. In addition, the quarter wavelength transmission lines used in the FCE method make the configuration naturally suited for detuning or mode switching,

and a switchable bilateral version of the coil was designed and constructed, as is described in the section 4.2 [85]. This section describes a modified version of the earlier FCE bilateral breast coil, modified for the insertion of a bilateral 32-channel receive array for ^1H imaging and spectroscopy at 7T.

FCE requires the use of quarter wavelength transmission lines ($\lambda/4$ T.L.) to drive each coil element. The currents delivered to each element are forced to be equal, regardless of loading difference and mutual coupling between the closely-spaced elements. The FCE bilateral coil consisted of two quadrature coils, each comprised of a Helmholtz pair and a saddle pair. In the previously reported switchable bilateral coil, standard coax cables are used as the $\lambda/4$ T.L. In this design, loop coils with concentric RF ring shields are employed. The element, apparently, is a balanced structure. Feeding a balanced coil element with an unbalanced structure (coax) requires the use of balun. A RF shield was employed on both sides of the coil for two reasons. 1) The shield was connected to the outside shield of the $\lambda/4$ T.L. on the CVP side, and left open on the coil side. A short circuit will be transformed into an open circuit by the $\lambda/4$ T.L. formed by the outside shield of coax and the RF shield. Doing this has the same effect as putting a balun on the coaxial cables; 2) The connected $\lambda/4$ T.Ls forms a $\lambda/2$ T.L, the outside shield of the coaxial cable then forms a ‘dipole-mode’ that could couple to the coil. The RF shield employed isolates the cables and the ‘dipole’ from the coil. While effective, the shielding is too restrictive for the insertion of a receive array and the associated hardware and cabling.

One option to overcome this difficulty is to use traditional baluns as was done in the unilateral transmit coil. However, as stated above, connected baluns could form a

‘dipole’ mode that potentially affect the coil performance. Furthermore, the bulky LC baluns still requires a lot of space, which is a big concern for 32- channel receive array installation.

In this design modified for array insertion, shielded twinaxial cables (RG108), instead of traditional coaxial cables are used as the $\lambda/4$ T.Ls. The shielded twinaxial cables allow balanced signal transmission and therefore eliminate the need for integrated baluns or RF shields, allowing space for the receive array integration. Care needs to be taken, however, to balance the signal in the twinaxial cables.

4.3.2 Coil Design

The design of the coil itself, including the Helmholtz pair and the saddle pair follows the same principle as the previously reported unilateral quadrature coil [52]. The Helmholtz pair consists of two loops, each with 160 mm i.d. and 172 mm o.d. 12 equally-spaced breaks of 2 mm distance segmented each loop. One capacitor across each break (except for the feed point) has a value of 11 pF. Passive-Plus 1111C 1.5 kV capacitors are utilized.

A concentric coplanar shield surrounds each loop, with 180 mm i.d. and 187 mm o.d., and has two 2 mm breaks, 90° and 270° from the coil feed point. 1800 pF capacitors are used to avoid eddy current.

The two loops are coaxially spaced 80 mm apart, with each loop’s copper and components facing the center of the coil volume. Each loop element is fed from a CVP by a length of RG108 (Pasternack) shielded twinaxial cables. The length of each is about 16.5 cm.

The match and tune board included three capacitors: two for balanced match and one for tune. Two of these capacitors—the tune capacitor and the match capacitor in series with the feed cable’s center conductor—are Sprague-Goodman SGNMNC1206E 2-20 pF 6 kV variable capacitors. The third capacitor—the match capacitor in series with the feed cable’s shield—was an ATC 100C 7.2 kV 11.0 pF fixed capacitor, approximately equal to the value of the variable match capacitor when the coil was loaded. In order to decouple the transmit coil during receive, PIN diodes (MA4P7441F-1091T) are added onto the CVP.

The saddle coils are mounted on the inside of a 152 mm i.d. acrylic tube, with copper and components facing outward. Designed to have an angular aperture of 120° on the 76 mm radius, the coil follows a rectangular shape with inner measurements (when flat) of 153 mm wide x 81.4 mm tall, outer measurements (when flat) of 165.2 mm wide x 93.6 mm tall, and a shielding conductor of 3.8 mm trace width spaced 4.5 mm outside of the coil rectangle. 12 breaks of 2 mm distance segments each rectangle: four breaks each on the top and bottom, and two breaks each on the sides. One capacitor across each break (except for the feed point) has a nominal value of 13 pF. Passive-Plus (rebranded Dalian Dalicap) 1111C 1.5 kV capacitors are utilized.

The shielding conductor has two 2 mm breaks, adjacent to the left- and right-side coil breaks. 1800 pF capacitors are placed across the gaps to avoid gradient-induced eddy current.

The match and tune board includes three capacitors: two for balanced match and one for tune. Two of these capacitors—the tune capacitor and the match capacitor in series

with the feed cable's center conductor—are Sprague-Goodman SGNMNC1206E 2-20 pF 6 kV variable capacitors. The third capacitor—the match capacitor in series with the feed cable's shield—is a Passive-Plus 2225C 7.2 kV 13 pF fixed capacitor, approximately equal to the value of the variable match capacitor when the coil is loaded. In order to couple DC power to the PIN diode, RF chokes (Bourns, 8230-14-RC) are added parallel with the matching capacitors.

In order to shield the E field from the distributed capacitor, a 1 cm x 0.8 cm copper patch adhere to the other side of the PCB, under each segmentation capacitor. The feed position does not have a copper patch to avoid disturbing the Forced-current condition.

Each loop element is fed from a CVP by a length of RG108 (Pasternack) shielded twinaxial cables. The length of each cable is about 16.5 cm.

In order to decouple the transmit coil during receive, PIN diodes (MA4P7441F-1091T) are added to the CVP.

4.3.3 Transmission with Shielded Twinaxial Cable

Twinaxial cables (RG 108, Pasternack) are used to connect the coil elements and the matching network, including the quarter-wave length cable and another short cable that compensates for the impedance variation.

Traditionally, coax cables are used for MRI coil transmission and reception. In FCE coils, however, the coil elements are balanced devices, and the cable used to excite the coil needs to be balanced. On the unilateral quadrature breast coil we used coax cable (EZ-form-86) to excite the coil element, and a LC type can balun was included to avoid common-mode current radiation.

In constructing the switched mode bilateral/unilateral breast coil we've determined that the two consecutively-connected quarter-wave baluns forms a dipole mode. This is because the balun is designed to create an open circuit close to the coil, so looking at the outside shield, the equivalent circuit is as Fig. 20:

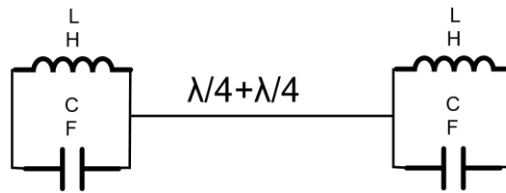


Fig. 20. Dipole mode formed by the baluns on connected FCE coaxial cables

With the bilateral coil the situation become more complicated due to the inclusion of multiple quarter-wave cables. So, in the switched-mode coil a shield is inserted between the coil and the quarter-wave cables. As described before, the shield blocks the space needed for 32 channel receive array insert. The unilateral breast coil also has bulky LC can baluns integrated on the coax that limits the space available.

On the modified coil, we use the shielded twinax cable to connect between coil elements and matching network. The twinax cable chosen is RG108 from Pasternack. The cable has a characteristic impedance of 78 ohms. With the twinax cable the signal is transferred in a balanced manner and there is no return path (a third conductor) as does the coax cable. There is no need to integrate balun/cable trap on the twinax cable. The twinax

cable selected are flexible cables that makes the installation of receive array much easier. Using twinax cable would also require the matching circuit be balanced.

However the benefit from using twinax cable does come with a cost. Twinax cable typically has higher loss at high frequency. Compared to the coax we used previously- EZ-form-86, it has slightly higher loss as shown in Table 2:

Table 2 Losses of different cables (twinax vs. coax)

	Loss	frequency
RG 108 twinax	16.2 dB/100 ft	400 MHz
EZflex-86	15 dB/100 ft	500 MHz

The amount of difference in loss is not likely to make a big difference given the very short cable length being used. Furthermore, a twinaxial cable that has even lower loss may be found.

In order to couple DC biasing signal to the PIN diode, two bias tees, one for the Helmholtz pair and one for the saddle pair, were included. The isolation between DC and RF ports on the bias tee was measured to be -50 dB, which is sufficient for normal operation. Should the DC port and RF port be designed orthogonal to each other on the layout, higher isolation may be achieved, which should be considered in the future. The insertion loss is less than 0.1 dB

The ¹H elements were initially tested without the addition of bias-T circuitry or the presence of receive array elements.

4.3.4 Coil Testing-Bench Measurement

The impedance of the Helmholtz pair loop is provided in Table 3, when unloaded:

Table 3 Modified bilateral transmit coil-impedance of all Helmholtz pair element

Loop location	Z
Left top	$7.1+j24.7$
Left bottom	$7.4+j25$
Right top	$7.4+j26$
Right bottom	$7.4+j26.7$

The impedance of the saddle pair loop is provided in Table 4, when unloaded:

Table 4 Modified bilateral transmit coil-impedance of all saddle pair elements

Loop location	Z
Left-left loop	$21+j100$
Left-right loop	$20+j98.3$
Right-left loop	$19+j102$
Right-right loop	$20+j98.5$

The B field produced by the bilateral coil was measured at five places at each coil (left and right): top loop center, coil center, bottom loop center, left loop center, right loop center. Quadrature combiners (ZX10Q-2-3-S+, Minicircuit) were used on the transmit side and the receive side, together with RF cables with same length, to characterize the quadrature excitation and reception capability. The measurement was taken with a

shielded quadrature probe on network analyzer HP4195A and the result is provided in Table 5.

Table 5 S21 measurement at different locations inside the transmit coil, measured with a shielded probe

S21 data (in dB)	Top loop center	coil center	bottom loop center	left loop center	right loop center
Left coil	-32.5	-33.7	-33.7	-35.3	-34.4
Right coil	-32	-33	-31.5	-34.6	-34

Good homogeneity is achieved from the Helmholtz pair. The most significant inhomogeneity is brought by the saddle pair.

The coupling between Helmholtz pair and saddle pair was determined through a S_{21} measurement. The S_{21} measurement between Helmholtz pair and saddle pair when matched and tuned shows a coupling of -22 dB.

4.3.5 Detuning

The method for detuning a FCE coil has been shown in section 3.4. In order to decouple the transmit coil during receive, PIN diodes (MA4P7441F-1091T) are added to the CVPs. -5V/detune signal and +12 V/tune signal was provided on bench. In section 3.4, a S_{11} based mode-splitting method was used to qualitatively measure the decoupling performance. For this coil, a double-loop probe S_{21} measurement method is used to

quantitatively assess the decoupling performance. The size of the probe needs to be large because of the relatively low sensitivity of the large coil, as is shown in Fig. 21.

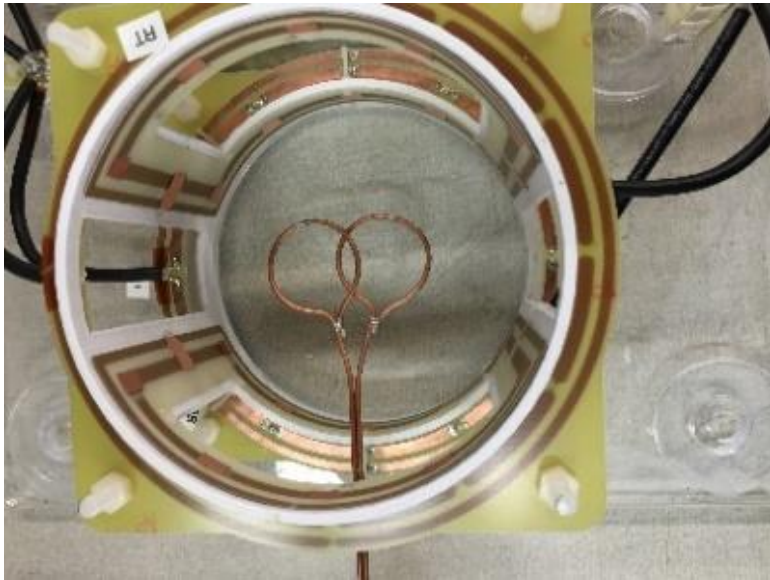


Fig. 21. Photo of the double-probe detuning setup

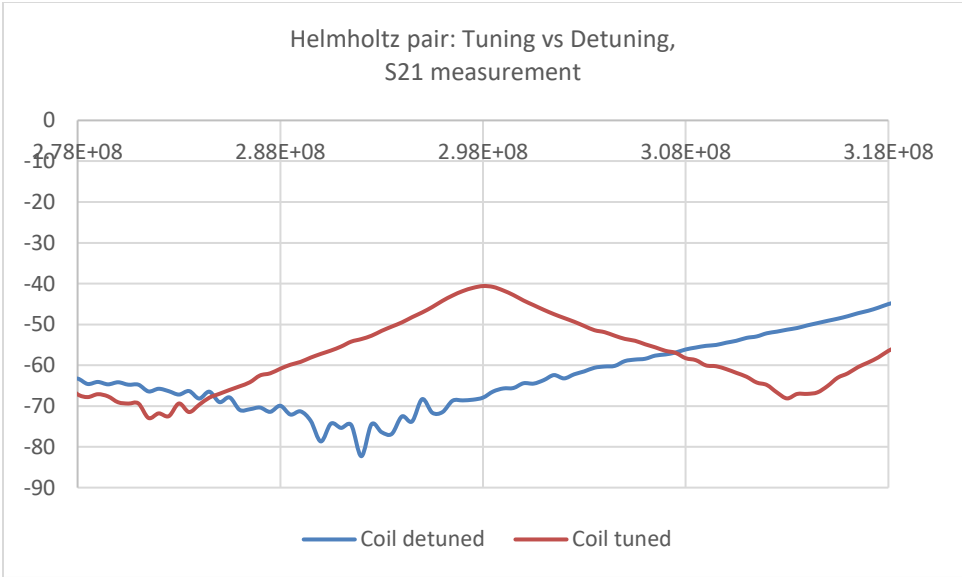


Fig. 22. S₂₁ measurement: Tuning vs. Detuning. Helmholtz pair

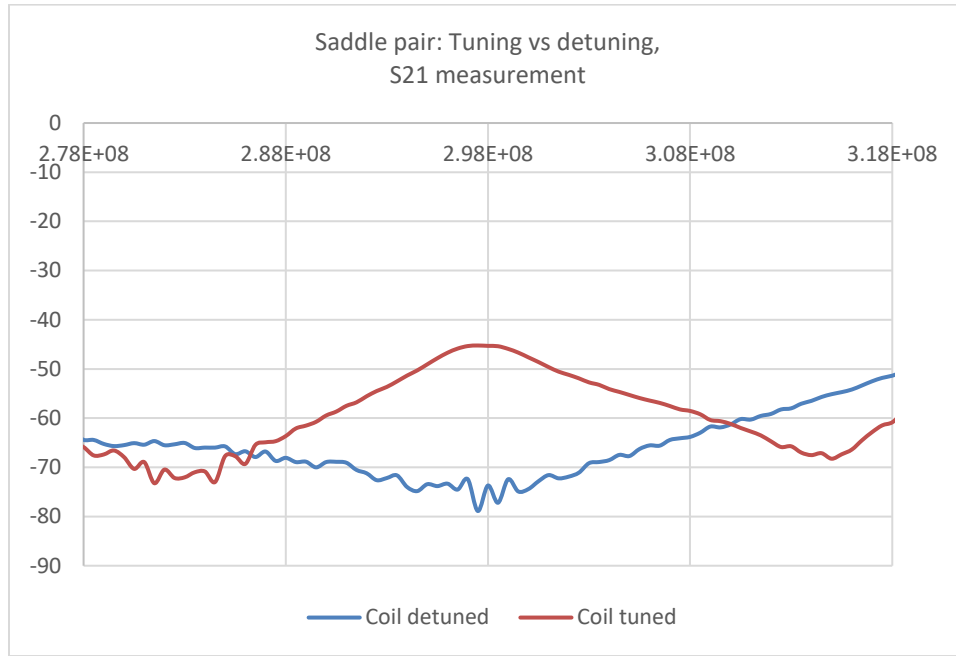


Fig. 23. S₂₁ measurement: Tuning vs. Detuning. Saddle pair

In both cases (Fig. 22 and Fig. 23), the isolation at coil center achieved through detuning is above 25 dB. At the edge of the coil conductor, the isolation is lower but is kept below 15 dB.

Detuning is also verified with a loop coil with 7 cm diameter (roughly the size of the 32 channel receive element). By looking at the return loss, any coupling can be easily visualized as a mode split. When positioned inside the transmit coil, the loop coil heavily couples to both the Helmholtz pair as well as the saddle pair. When detuning signal is applied, there is still a frequency shift of the resonance, however the mode split degenerate to a single resonance.

4.3.6 Coil Testing – MRI Experiments

The coil is compared with the previous design (operated in bilateral mode) on the bench using an S_{21} measurement between the coil and a shielded quadrature probe input to a quadrature combiner. Imaging of a canola oil phantom was performed on a Philips 7T Achieva system, with the transmit coil operating in transmit/receive mode (THRIVE w/o fat suppression, FOV: 150 mm \times 286 .452mm \times 370 mm (AP \times FH \times RL), resolution: 372 \times 368, TR: 4.0 ms). The 32 channel receive array was designed by others, for insertion into the transmit coil with detachable boards on each element that include the active detuning network, match and tune capacitors, and a balun.

The bilateral coil modified for array insertion is shown in Fig. 24, with dimensions and the twinaxial cable addition labeled. The quadrature S_{21} bench measurement comparison indicates an improvement of 1.2 dB in efficiency over the previous shielded version. This is at least partially due to the fact that the modified version does not include PIN diodes for switching to unilateral operation. The phantom images acquired from the coil in T/R mode are shown in Fig. 25, demonstrating homogeneous excitation. The Philips drive scale required for a 90-degree tip angle is 0.45 as compared to 0.51 for the shielded version, in agreement with the improvement in efficiency predicted by the bench measurements. The array is shown successfully integrated into the bilateral FCE coil in Fig. 26. The bilateral coil easily matched and tuned over the range required with and without the array inserted.

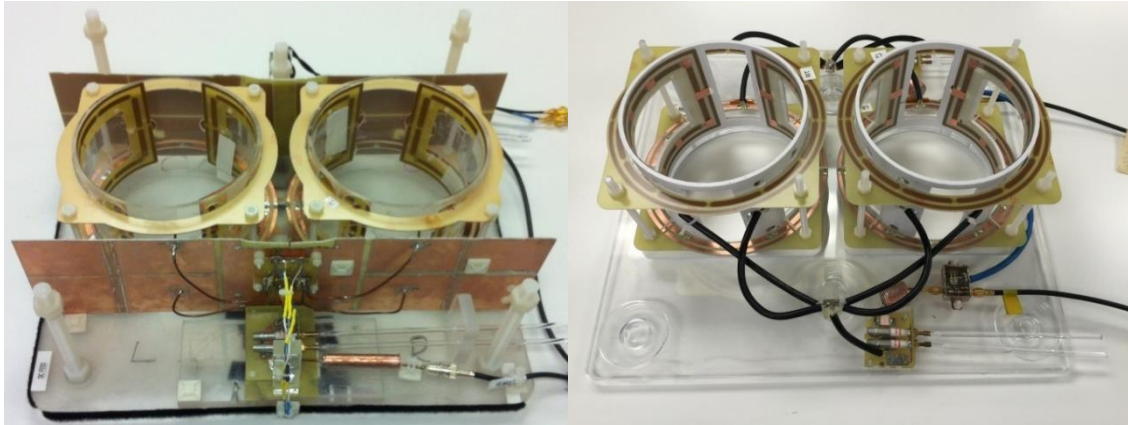


Fig. 24. (Left) The switched-mode bilateral breast coil reported earlier; (Right) Modified FCE bilateral coil for receive insertion. Each Helmholtz pair consists of two 166mm loops spaced 80 mm apart, with a concentric coplanar shield surrounding each loop. Each saddle pair consists of two 165 x 94 mm rectangular coils mounted inside a 3D printed cylindrical tube with an inner diameter of 152mm. Reprinted with permission from [56].

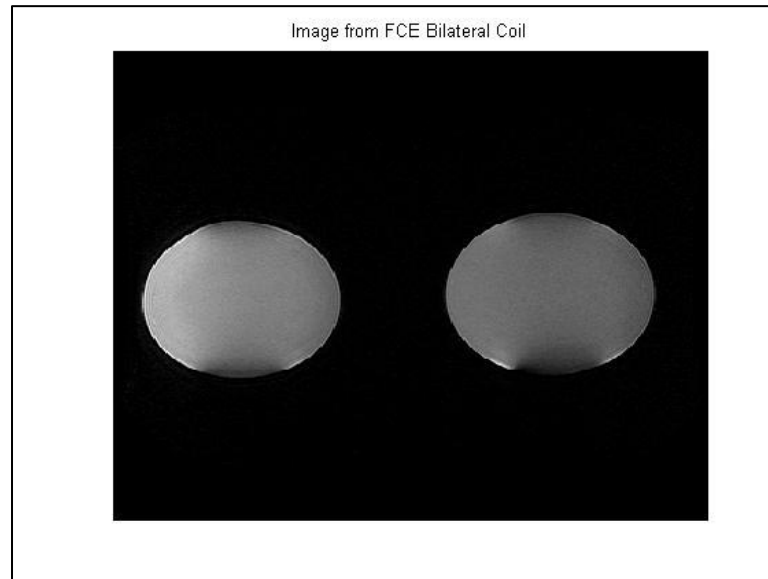


Fig. 25. MR Image (coronal) taken from FCE bilateral coil. Homogeneous excitation is achieved. Reprinted with permission from [56].

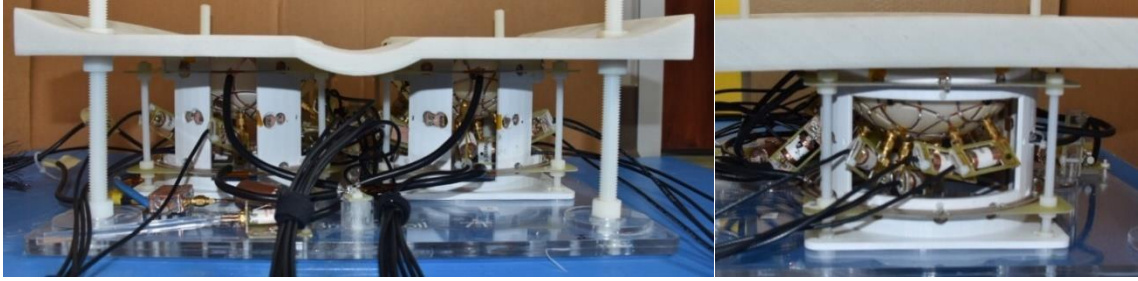


Fig. 26. Bilateral FCE transmit coil with 32- channel array coil. A) front view of the bilateral coil with array coil integrated. The $\lambda/4$ T.L. are connected from the two Helmholtz pairs to a CVP, then from CVP to the match and tune network (M/T). B) side view of the integrated coil and array. Reprinted with permission from [56].

4.4 Method for Simultaneous Tuning in Switched-Mode FCE Coils

Previously we have designed a 7T bilateral/unilateral breast coil using the FCE+switchable FOV concept [54]. In bilateral mode uniform excitation is achieved; In unilateral mode signal in the unused coil is successfully suppressed to avoid patient's exposure to heat. However, the difference in loading causes the coil to render different impedance in different modes. Although the difference in impedance between unilateral modes is often similar and does not require retuning, that between unilateral mode and bilateral mode is not to be overlooked, and therefore require retuning. This is inconvenient and time consuming during a clinical scan. Here, we explain a design that can potentially eliminate the need for retuning.

The method is to have the two symmetric coil elements sharing a tunable reactive element:

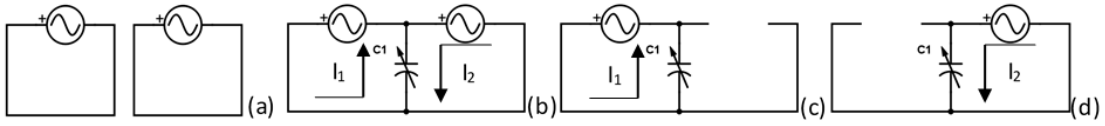


Fig. 27. Equivalent circuit for different modes

Equivalent circuit for different modes. (a) shows the original design where two coil elements are isolated. (b-d) shows the proposed design in different modes

In dual mode (Fig. 27 (b)), no net current flows through C_1 because equal current is forced to the two symmetric coil elements using FCE. Tuning C_1 will not affect coil impedance. In single mode, however (Fig. 27 (c)-(d)), the unused element is detuned. In this case, current flows through C_1 instead of the detuned element, and tuning C_1 will change the impedance of the coil. Therefore, carefully choosing C_1 can reduce the difference in impedance of different modes and avoid retuning between mode switching.

For proof of concept, two loop coils (7cm x 8cm, separated by 2cm) were built. Each element breaks up at four places for placing segmentation capacitors and the tunable capacitor C_1 . Mode switching is controlled using two power supplies. Impedance at CVP and the coil return loss was measured at 200MHz (Larmor frequency for 4.7 T) before and after adopting the proposed modification. Additionally, B_1 profile of the proposed design was measured at 2cm away from the coil, in three modes (Fig. 28).

The results show that by having two coil elements sharing a tunable reactive element, minimal difference between return loss in three modes can be achieved, and retuning can be avoided. The B_1 map shows the expected field pattern for different modes.

Impedance and return loss before and after proposed modification is provided in Table 6.

Table 6 Impedance and return loss before and after the modification

	Single mode-coil 1	Single mode-coil 2	Dual mode
Impedance at CVP, before modification (in ohm)	$2.2+j33.4$	$2.4+j36.5$	$1+j17.5$
Impedance at CVP, after modification (in ohm)	$4+j53.6$	$4.9+j54.6$	$5.8+j53.7$
Overall return loss, before modification (in dB)	-21.7 dB	-10.2 dB	-0.6 dB
Overall return loss, after modification (in dB)	-21.8 dB	-25.9 dB	-21.7 dB

When measuring return loss, coil was tuned for Mode 1. Coil was not retuned after mode switching. As can be seen, the proposed modification reduced the difference between impedance of different mode and eliminate the need for retuning.

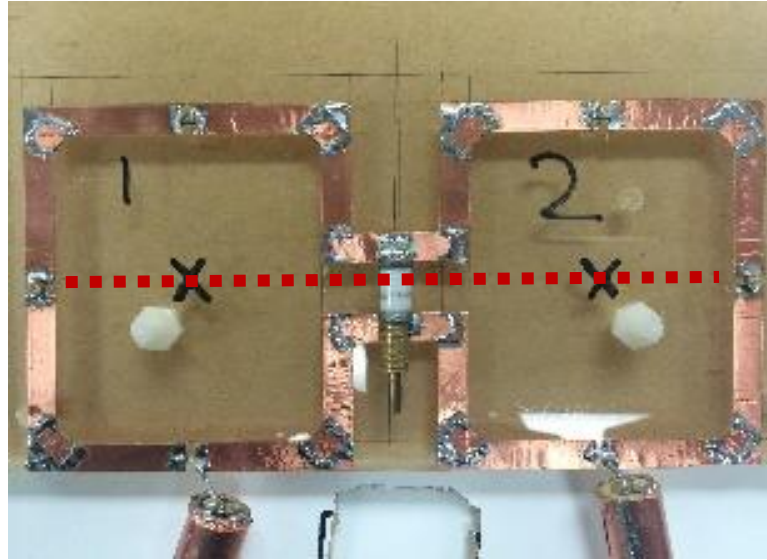


Fig. 28. Photo of the FCE coil modified for simultaneous tuning

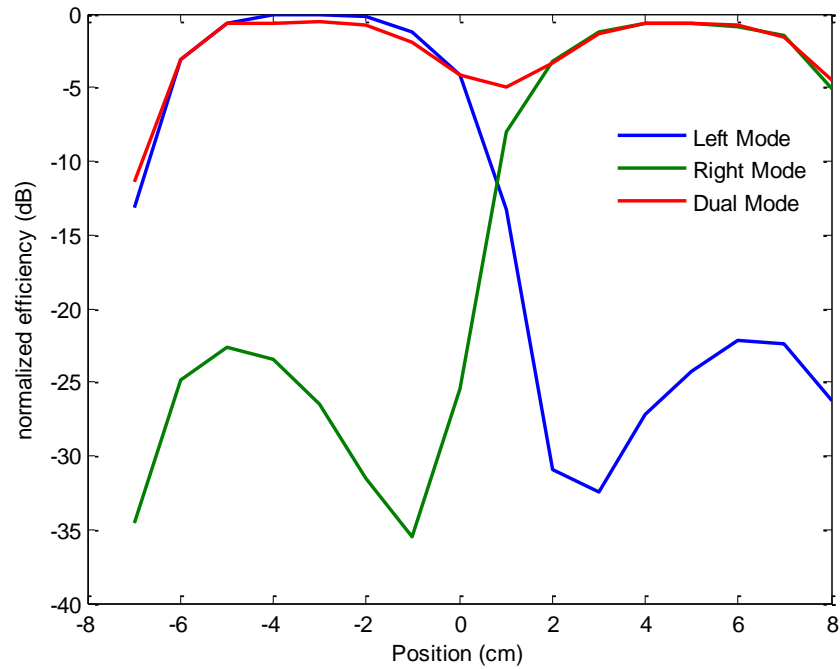


Fig. 29. Profile across the coil in different modes, after the modification. Values are scaled to the global maximum.

Photo of the coil with the proposed design and B_1 map across the coil in three modes are shown in Fig. 28 and Fig. 29, respectively. The dashed line in the photo indicates the position of measurement. In dual mode uniform excitation is achieved, while in single mode sufficient suppression of the detuned coil is observed as before the modification.

This method could be useful for rung element based coil too. However, it may not be applicable to elements such as dipoles, as there is not return path for current.

A limitation of this method is that the added component can only make up for the reactance difference between the two modes, but not the resistance difference. If the resistance is wildly different, the method may not work as well. However, for low-Q cases, the return loss may not be very different even when resistance is not close, between the two modes.

CHAPTER V

SWITCHABLE TRANSMIT ELEMENT FOR SPINE IMAGING AT 7T

5.1 Introduction

MRI is frequently used in clinical routines for diagnosing diseases in the spine cord [86-90]. Examples include tumor staging, multiple sclerosis and vascular malfunctions. High field spine imaging is difficult due to the large field of view (FOV) required. Given the varying depth of the spine within patients' body, it is especially difficult on the RF transmission side due to its requirement on both the length and the depth of the B_1 field. The traditional design involves the use of a long structure, taking the form of either dipole or microstrip transmission line.

However, in many cases, it is desirable to excite only part of the spine while redundant power decomposition in other places is avoided. An example of this is the axial acquisition of the spinal cord. Therefore it is of interest to use the FCE+switchable FOV principle on spine coil design.

In this chapter, the switchable FOV 7T spine coil design is investigated using a variety of methods, including simulations, bench measurements, and MR experiments. The first goal is to choose a suitable element that gives the highest $B_1/\sqrt{SAR_{10g_max}}$ efficiency at 5cm deep [35], with uniform excitation pattern. In section 5.2, rung elements with different configurations are compared in terms of $B_1/\sqrt{SAR_{10g_max}}$ efficiency and $B_1/\sqrt{input_power}$ efficiency. The height of the rung and the configuration of the ground is discussed and optimized. In section 5.3, a switchable rung element for 7T spine imaging

was implemented for the proof of concept and was tested on bench; In section 5.4, the possibility of using multiple short dipoles to form a switchable spine coil is investigated. The effect of using a short dipole on transmit efficiency is discussed. Although this topic is briefly discussed in [91, 92], the discussion is limited in a few geometries and is based on FDTD simulations only. Here several numerical methods are used to validate the comparison; In section 5.4, a segmented element design using Forced-Current Excitation and a switching circuit is presented. Comparison is made between a rung and a dipole. Also in this section, a few more configurations/element designs are considered, and a segmented dipole design was chosen as the final design. The segmented dipole was implemented and tested on bench and through MR experiments with a 7T body scanner. Large FOV is obtained when the segmented dipole is in long mode, and improved $B_1/\sqrt{SAR_{10g_max}}$ efficiency is found when the dipole is in short mode.

5.2 Rung Element Configurations for Spine Imaging at 7T

A rung element, as presented in [52], can be designed to be long enough to provide coverage for the spine. A switchable rung element that contains three short rung elements can be designed to provide switchable FOV. Many different configurations are possible to provide such capability. Meanwhile, there are parameters that need to be adjusted to find the best performance candidate (e.g, the height of the rung). As a first step, some initial configurations of rung elements are modeled and compared in this chapter.

5.2.1 Initial Trials

In the first trial, the phantom is extracted from [91], which is 50 cm x 50 cm x 50 cm, with dielectric constant of 34 and conductivity of 0.4 S/m. The switchable rung element can be made separate or consecutive, as shown in Fig. 30. When only one of the elements are excited, all other elements are open-circuited at the feed point, as explained in section 3.6.

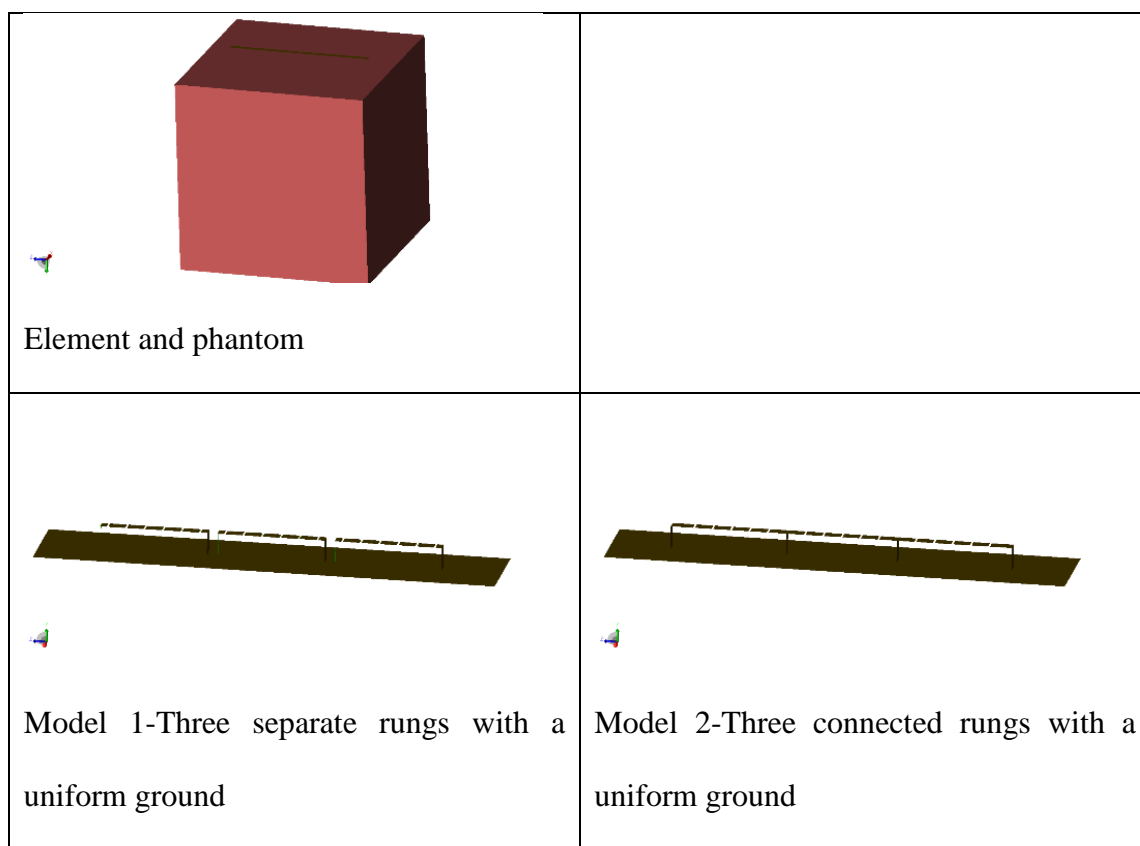


Fig. 30. Model rendering for rungs and dipoles in different configurations

B_1 is calculated in the central sagittal planes (Fig. 31), with all cases scaled to 1W input power.

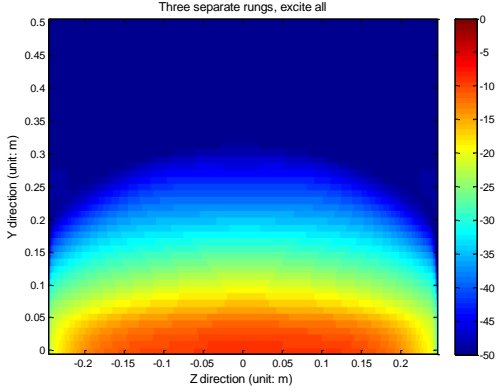
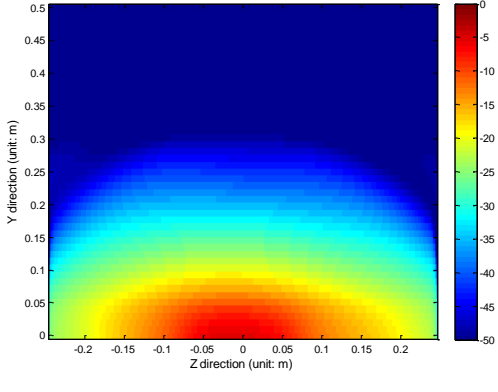
	B_1 map, calculated at central sagittal plane (in dB, reference to global maximum)	Maximum 10g averaged SAR
Three separate rungs, Excite all elements		0.86 W/kg
Three separate rungs, Excite only the middle element		1.54 W/kg

Fig. 31. B_1 pattern and maximum 10g averaged SAR in each case

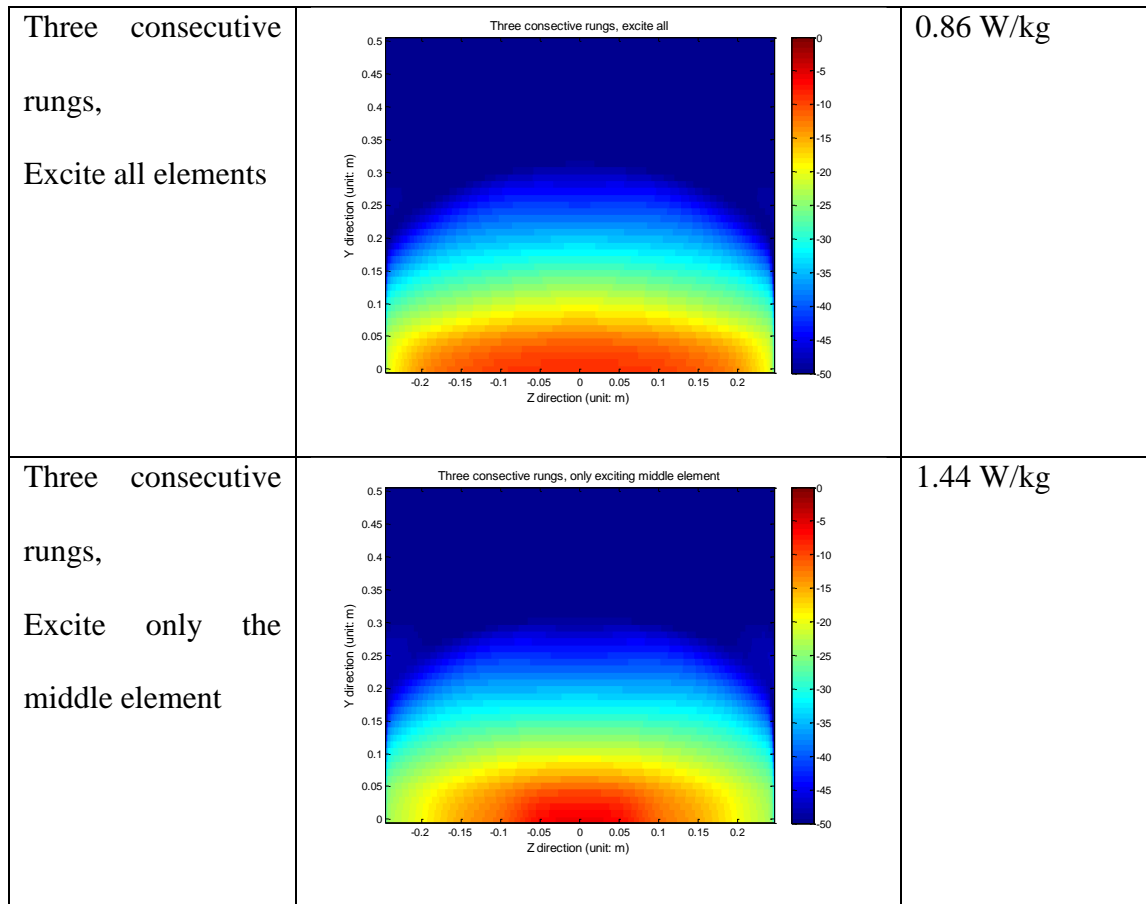


Fig. 31. Continued

The $B_1/\sqrt{\text{input_power}}$ profile as well as $B_1/\sqrt{\text{SAR}_{10\text{g_max}}}$ efficiency along y direction for all cases, are plotted in Fig. 32 and Fig. 33, respectively:

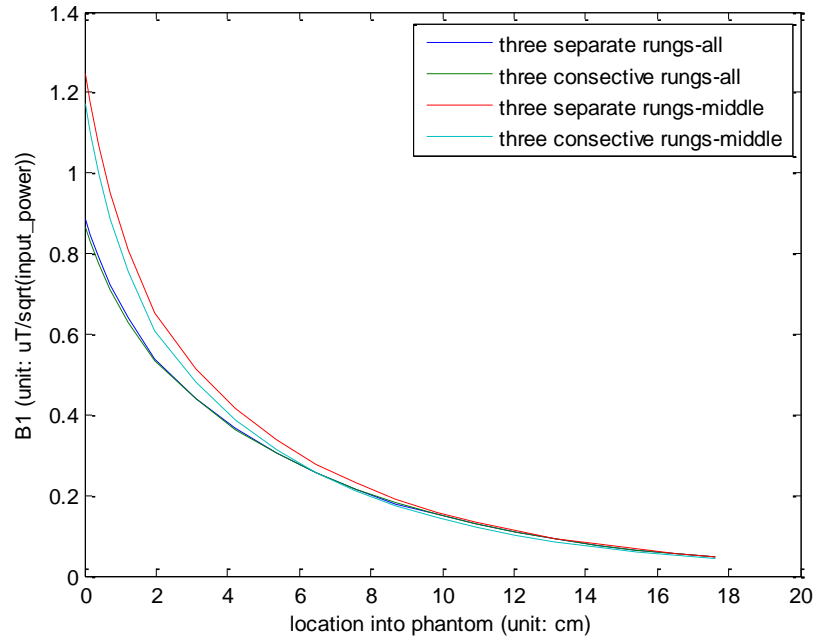


Fig. 32. $B_1/\sqrt{\text{input_power}}$ efficiency comparison between separate rungs and connected rungs, in different modes

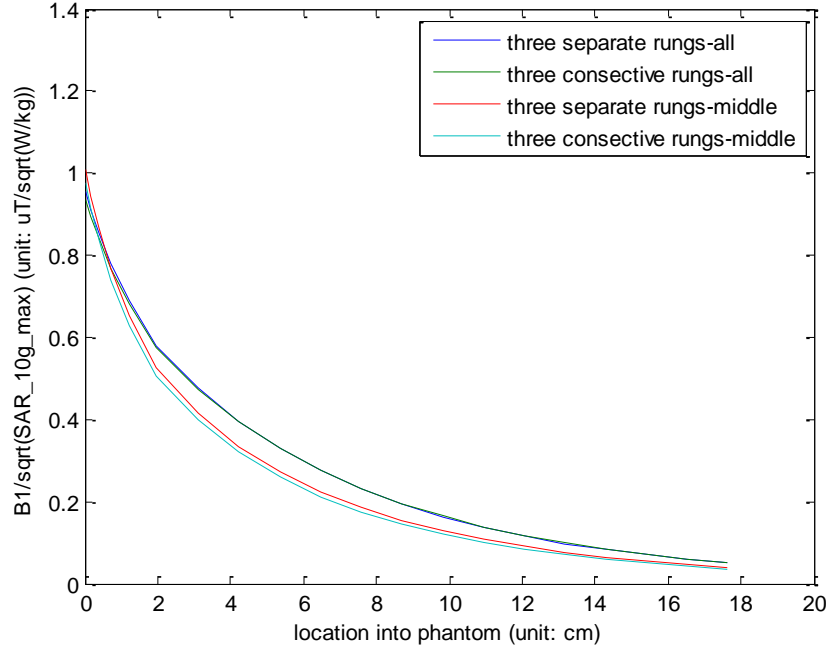


Fig. 33. $B_1/\sqrt{\text{SAR}_{10\text{g_max}}}$ efficiency comparison between separate rungs and connected rungs, in different modes

From the B_1 patterns, it is shown that in the long mode, the rung provides long and uniform excitation in the z direction. Also noticed is that the significant residual signal at the ‘detuned’ elements. It shows that those elements are not effectively detuned, which is not expected. As a result, the short mode (when only one element is excited) does not have the expected $B_1/\sqrt{\text{input_power}}$ efficiency advantage over the long mode (when all elements are excited). This, is suspected to be due to the continuous ground shared by the three elements, which promoted longer current distribution along z .

The different configurations do not show significant difference in terms of $B_1/\sqrt{\text{SAR}_{10\text{g_max}}}$ efficiency or $B_1/\sqrt{\text{input_power}}$ efficiency. For simplicity of the design,

the separate rung configuration should be used due to its unbalanced structure. The need for balun is avoided in this configuration.

5.2.2 Uniform Ground vs. Separate Ground for Rung Element

In the last section, it was noted that the residual signal from the detuned elements is still significant, as is shown in Fig. 34.

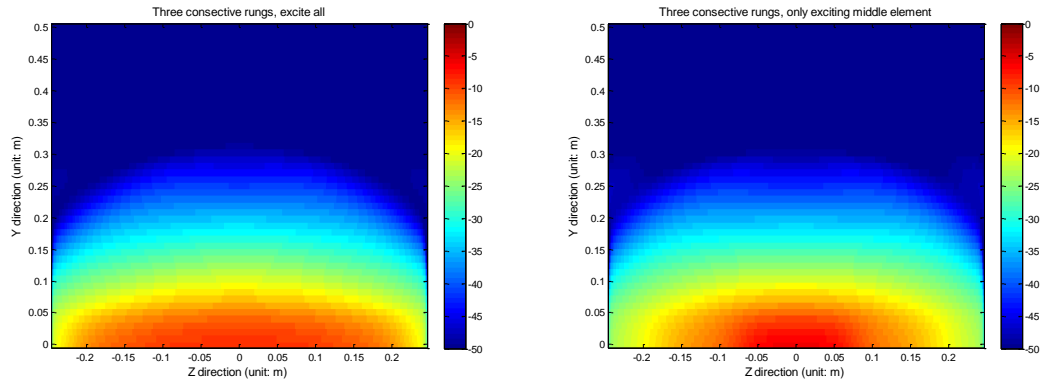


Fig. 34. Three short rungs - middle only vs. all three excited

Even when only the middle rung is excited, the field distribution is very widely spread across the imaging region.

It is suspected that when using a uniform ground across three elements, the current on the ground extends to the area where the ‘detuned’ elements are located, resulting in the residual signals as shown in Fig. 34. After a serious of investigation using simulation, it is concluded that each short rung need to have a dedicated ground plane to have more focused field distribution, as shown in Fig. 35:

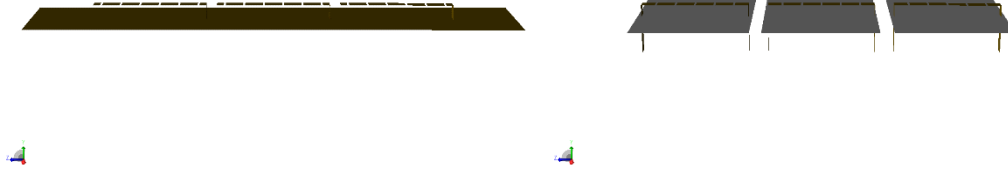


Fig. 35. Three short rungs configuration-a uniform ground vs. three separate grounds

When using separate grounds the residual signal from the ‘detuned’ elements is largely suppressed, as shown in Fig. 36:

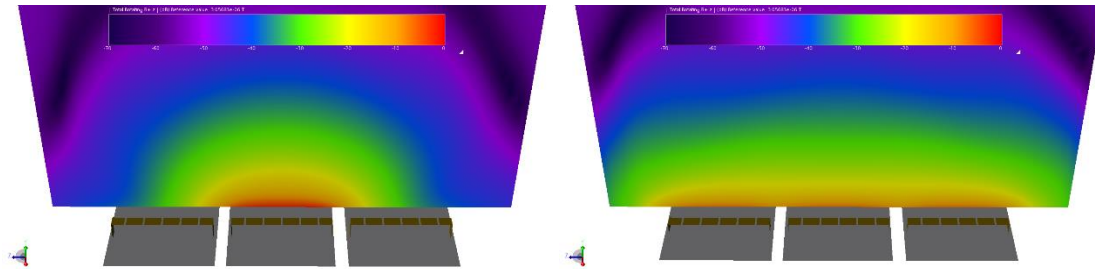


Fig. 36. Pattern from the configuration where separate grounds are used

5.2.3 Height of the Rung

Initially it was assumed that having a larger height could improve the penetration of the rung, as the opposing current on the signal and on the ground are further separated. EM simulations were performed on the same phantom, with the distance between signal and ground varying. $B_1/\sqrt{\text{input_power}}$ with different height is compared along the central y direction in Fig. 37:

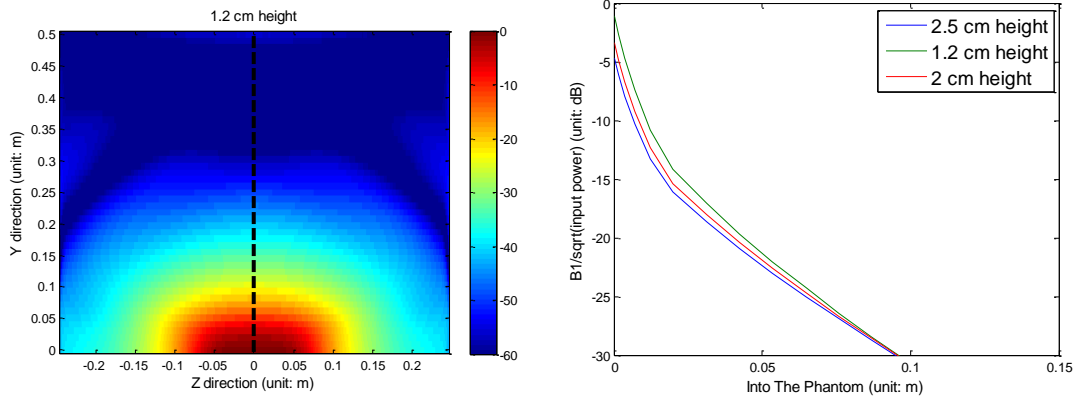


Fig. 37. Sagittal B_1 pattern for rung element of different height

There is no significant difference in efficiency at 5 cm into the phantom. The efficiency was found to be highest when height = 1.2 cm. This is convenient since the half-inch acrylic is about the thickness. The width of the shield was set at 10 cm at first, but was increased to 15 cm after optimization of the B_1 efficiency.

Dipole has been used for 7T spine imaging [35]. The transverse B_1 field pattern is different between rung and dipole elements. Although the sagittal plane and coronal plane field pattern of the rung looks reasonably uniform, there is an obvious asymmetry in the transverse pattern (Fig. 38). This is one of the disadvantages of the rung when compared to the dipole.

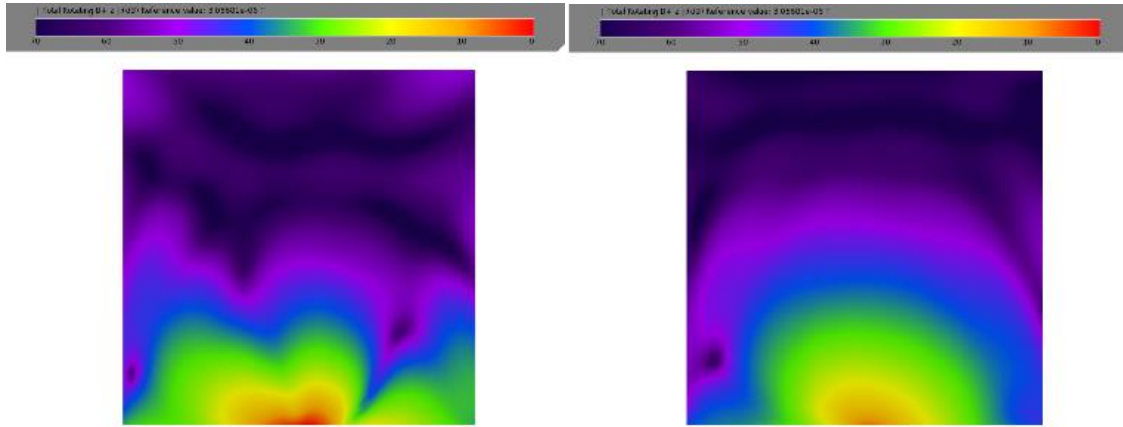


Fig. 38. Transverse field pattern comparison - rung vs. dipole

This is a known problem with regular element at 7T when a return path of the current is found. The B_1 field pattern of the dipole looks more simple and uniform. This, as proved by Raaijmakers et al [91], may facilitate the development of parallel transmit array system without complicating the mutual coupling problem. Further quantitative comparisons between the rung and the dipole is provided elsewhere in this dissertation (section 5.5):

5.3 A Segmented Rung Element with FCE and Selectable FOV

Although studied in detail using electromagnetic simulation, as is described in the previous sections, it is desirable to build a switchable FCE spine coil element for the proof of concept.

As is briefly described in the introduction section, the large field of view (FOV) for spine imaging requires a long RF coil for surveying the spine. At lower field a body

coil can be used for transmission with an array for reception. However most 7T system does not have a body coil. Additionally, at 7T it may be desirable to tailor the RF coil length such that only the desired portion of spine, e.g. cervical, thoracic or lumbar zone is excited while redundant power deposition into other part of the body, is avoided. Qi et al has reported a segmented coil design at 7T where the FOV can be adjusted to a certain degree [93]. However the design requires the dipole to be fed from the very middle of the entire structure, and does not allow the user to select the FOV near the edge of the coil, therefore is limited in terms of flexibility. As a proof of concept a switchable length rung design using a straightforward design which can provide uniform field distribution as well as enhanced flexibility for varying the FOV, are designed. A similar concept has been demonstrated previously with a switchable unilateral/bilateral 7T breast coil [54]. In this work, the design is scaled to three elements on a 37 cm long rung intended for use in a spine coil.

Based on the simulation results from section 5.2, three short current rungs, 11cm each and with 2 cm gap between them, are aligned in the z direction to form a 37 cm long spine coil. Each rung is segmented every 2cm with a 33pF capacitor. A ground plane, serving as the current return path, lies 1.2 cm beneath each current rung. According to the simulation results in section 5.2, the ground planes need to be separated between the three elements to enable successful FOV switching, and the 1.2 cm height was chosen according to B_1 efficiency. The rungs are fed from the side with $\frac{3}{4}$ wavelength coax cables with very low loss semi-rigid cable (EZ form-141). Three DC signals are generated from a power

supply module to control the switching circuit: a +15V bias activates the corresponding rung, while a -15V bias detunes it. The photo of the coil is shown in Fig. 39.

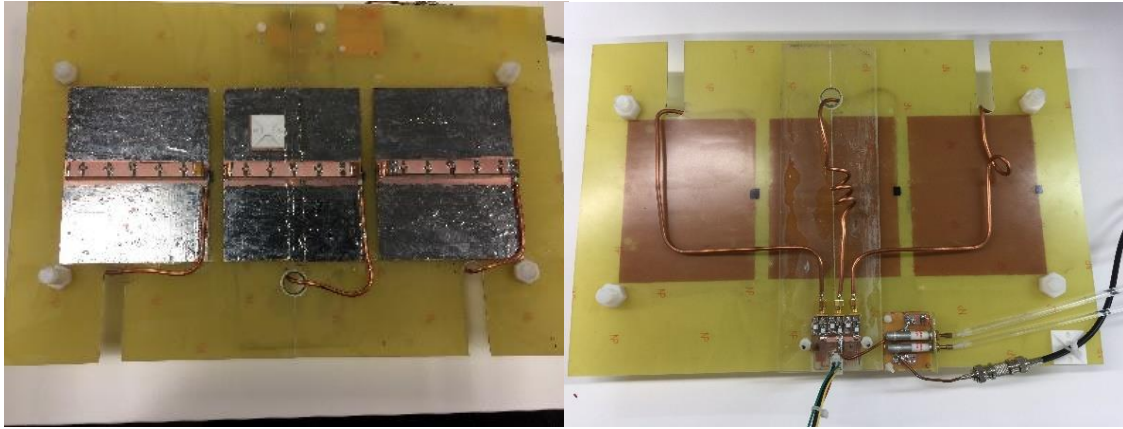


Fig. 39. (Left) Front side of the coil. The rungs are fed from the side. (Right) Back side of the coil, with the switching circuit, the coax cable, and the matching circuit. Reprinted with permission from [94].

With the ability to enable or detune each of the three elements, the coil is equipped with eight different operating modes in total, with one of the modes being ‘all off’, reserved for future integration of a receive array. Depending on the region of interest, the user can pick from any of the eight modes for imaging. The design is especially useful for continuous axial image acquisition of the spine cord, if equipped together with smart devices such as a Raspberry-pi Microprocessor. The coil was tested on bench in four modes. With the same input power applied, the efficiency of the coil in the four modes were measured using a shielded probe and a network analyzer with S21 method. The

measurement was taken along z direction with 1cm resolution, at 4cm away from the coil in the y direction at 298 MHz, which is the larmor frequency at 7T.

The four modes being tested are left coil only (Mode A), middle coil only (Mode B), right coil only (Mode C) and all coils (Mode A+B+C). The B_1 maps were plotted together and scaled to the global maximum in Fig. 40. Mode A+B+C demonstrate uniform excitation across a large FOV, which results from an equal current distribution achieved at each rung. Modes A-C demonstrate higher power efficiency in the corresponding area: The efficiency of mode A-C is 3.5-4 dB higher than that of Mode A+B+C, in the corresponding region. Additional modes, with two of the three rungs excited were possible but not presented.

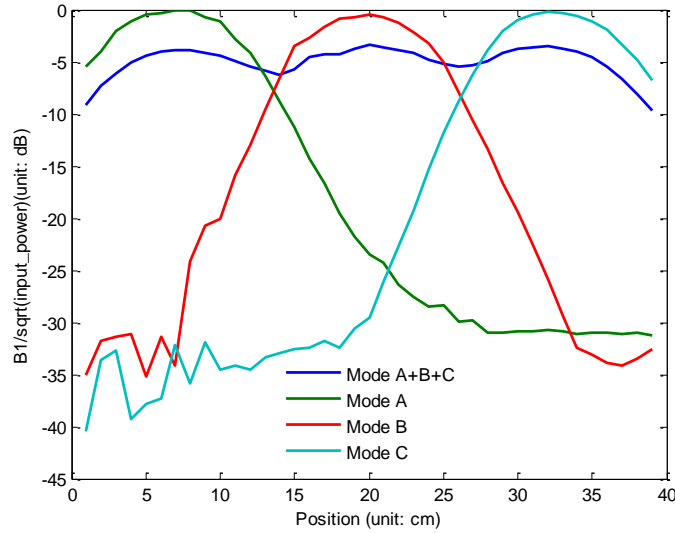


Fig. 40. Bench measurement in four modes. Mode 4 demonstrates uniform excitation across large FOV, while mode 1-3 demonstrate higher $B_1/\sqrt{\text{input_power}}$ efficiency (3.5-4 dB) at the corresponding region. Reprinted with permission from [94].

As a proof of concept, this work uses current rung as the basic element due to its simplicity, however as described by the simulation result, this method can be used for any type of coil element. In fact, in section 5.5, a segmented dipole design is proposed and more quantitatively analysis is provided. In addition, the coil structure can be divided into more elements (more than three) if smaller FOV and higher B_1 efficiency is required.

In this design, FCE is used to excite a three-element spine coil. It is also configured such that each small coil segment can be activated or detuned through electronic control, giving flexible FOV variation. A large FOV gives large coverage while a smaller FOV allows more focused RF power, potentially important in some applications requiring either low whole-body SAR or localized high B_1 values. In addition, when multiple elements are activated, the FCE method ensures uniform current delivery to the different element and prevents mode splits due to coupling. The previously reported switchable unilateral/bilateral demonstrated the ‘FCE+selectable FOV’ being applied to two elements (the left breast coil and the right breast coil). This rung element designed for spine imaging also proves the scalability of the ‘FCE+variable FOV’ concept, through the use of three closely spaced elements. This ‘extendable rung’ design will be used as the element in a two-element spine array, as will be described in the following section.

Furthermore, the choice of the basic element, will be studied more carefully in section 5.5.

5.4 The Effect of the Length of a Dipole on Transmit Efficiency

5.4.1 Description

As described in the previous section, long dipole has been used in 7T spine imaging. However, to have a switchable FOV spine coil we need to use multiple shorter element that can be individually turned on and off. Unlike loop element, which is well-understood, the impact from the length of the dipole on the efficiency and penetration remains unclear. There has been only a few publications that studied the size of dipole in high field MRI [91, 92]. In order to further validate the feasibility of using a short dipole as a RF coil, numerous simulations as well as analytical methods on short dipole vs. long dipole is presented in this section. The idea is that smaller dipole should render better B_1 efficiency than the long one, and can be used as a RF coil for MRI.

5.4.2 Electromagnetic Simulation

First the simulation was performed in XFDTD, the 37 cm regular dipole and the 11 cm dipole (three of them in a row in the z direction, with a gap of 2 cm between elements) are modeled. The elements are placed 4 cm away from the phantom. The phantom has an electrical property of ($\epsilon_r = 59, \sigma = 0.79 \text{ S/m}$) as in the paper where the long dipole is used for spine imaging [35]. The simulation is at 298 MHz. Input power is scaled to 1W in all cases. Since the goal here is to get a general idea whether a short dipole can be used as a feasible RF coil, the depth where the investigation is initially made is 10 cm, unlike other comparisons in this dissertation regarding spine imaging where 5 cm is of interest. The rendering of the model is in Fig. 41 and the result is provided in Table 7.

Later in this section, the depth of interest is changed to 5 cm in accordance with literature [35].

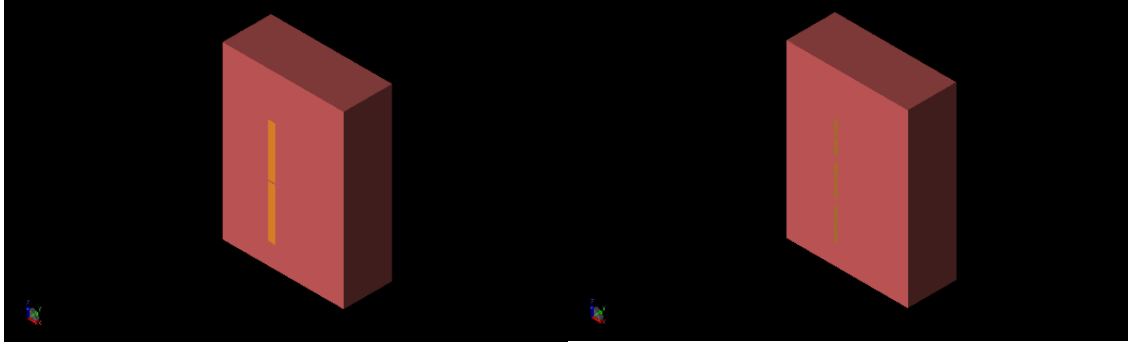


Fig. 41. Long dipole and three short dipoles as modeled in Remcom XFDTD

Table 7 Impedance, B_1 and SAR results calculated from XFDTD with three cases: Long dipole; Three short dipoles (excite all); Three short dipoles (excite only the middle one)

Model	37 cm dipole	11 cm dipole, only center one turned on	11 cm dipole, all turned on
Impedance	29.8-j4.3	1.9-j477.4	3-j461.3, 2.9-j446, 3-j461.3
1g maximum SAR	0 dB	4.5 dB	-0.5 dB
B_1 @ 10 cm into the phantom	0 dB	2.9 dB	-1.8 dB
$B_1/\sqrt{SAR_{1g_max}}$ @ 10cm into the phantom	0 dB	-1.6 dB	-1.3 dB

According to the simulation, the shorter dipole actually has better $B_1/\sqrt{\text{input_power}}$ efficiency, given the more concentrated power distribution. The performance in $B_1/\sqrt{\text{SAR}_{\text{lg_max}}}$ efficiency of the short dipole however, decreases with depth. This may be due to the fact that the longer dipole, which is closer to resonance length, can radiate better than the short dipoles. However, the feasibility of using short dipole as RF coil is still proved considering the two efficiency comparisons together.

5.4.3 Numerical Validation-Methods

Two more numerical approach was used to compare the B_1 and impedance of the two cases. These numerical methods can predict $B_1/\sqrt{\text{input_power}}$ efficiency but not $B_1/\sqrt{\text{SAR}_{\text{lg_max}}}$ (except the method-of-moment based simulation software), and therefore only $B_1/\sqrt{\text{input_power}}$ result is presented.

Method#1: Analytical approach, using derived analytical expressions from Harrington's electromagnetic text book and Balanis' text book [95, 96], which assumes sine-wave distribution on the dipole:

$$I_e(z') = \begin{cases} I_0 \sin \left[k \left(\frac{l}{2} - z' \right) \right], & 0 \leq z' \leq l/2 \\ I_0 \sin \left[k \left(\frac{l}{2} + z' \right) \right], & -l/2 \leq z' \leq 0 \end{cases}$$

$$R_r = \frac{2P_{\text{rad}}}{|I_0|^2} = \frac{\eta}{2\pi} \{ C + \ln(kl) - Ci(kl) + 1/2 \sin(kl) \times [Si(2kl) - 2Si(kl)] \}$$

$$+ \frac{1}{2 \cos(kl)} \times [C + \ln \left(\frac{kl}{2} \right) + Ci(2kl) - 2Ci(kl)]$$

$$\text{And } R_{in} = \left[\frac{I_0}{I_{in}} \right]^2 R_r$$

$$X_m = \frac{\eta}{2\pi} \left\{ 2Si(kl) + \cos(kl) [2Si(kl) - Si(2kl)] - \sin(kl)[2Ci(kl) - Ci(2kl)] - Ci\left(\frac{2ka^2}{l}\right) \right\}$$

$$X_{in} = \left(\frac{I_0}{I_{in}}\right)^2, X_m = \frac{X_m}{\sin^2(kl/2)}$$

$$A_z = \frac{1}{4\pi} \int_{-\frac{L}{2}}^{\frac{L}{2}} \frac{I(z') e^{-jk|r-r'|}}{|r-r'|} dz'$$

$$\text{Where, } |r-r'| = \sqrt{r^2 + z'^2 - 2rz' \cos \theta}$$

$$\mathbf{E} = -j\omega\mu\mathbf{A} + \frac{1}{j\omega\epsilon} \nabla(\nabla \cdot \mathbf{A})$$

$$\mathbf{H} = \nabla \times \mathbf{A}$$

The radius of antenna wire is assumed to be 5 mm.

Method#2: Use the 4NEC2 simulation program available online. (<http://www.qsl.net/4nec2/>). Here, the radius of antenna wire is assumed to be 1.5 mm (due to segmentation limitations from the software).

Method#3: A full-wave simulator developed by Dr. Steven Wright based on Method of Moment

5.4.4 Numerical Validation-Results

An 18.4 cm dipole was added to the comparison, to setup possible design of segmented dipole (which will be described in a following section). The comparison results are provided in Table 8-10.

Table 8 Impedance comparison in different simulation environments and analytical approach. Comparison is made between dipoles of different length

	Analytical	4NEC2	Remcom	MoM (SW)
L=11 cm	2.38-j464.3	1.87-j795	1.96-j 487.11	3.3-j750
L=37 cm	32.4-j116.1	34.1-j171	45.26-j 15.88	34.5-j128
L=18.4 cm	6.9-j346	NA	4-j247	5.97-j370

Table 9 Calculated B₁ field scaled to input current. Comparison is made between dipoles of different length at 4 cm away

	Analytical	4NEC2	Remcom	MoM (SW)
L=11 cm	2.66 uT	N/A	1.98 uT	2.15 uT
L=37 cm	4.52 uT	N/A	4.08 uT	4.15 uT

Table 10 Calculated B₁ field scaled to input power. Comparison is made between dipoles of different length at 4 cm away

	analytical	4NEC2	Remcom	MoM (SW)
L=11 cm	2.44 uT	N/A	2.00 uT	1.67 uT
L=37 cm	1.12 uT	N/A	0.82 uT	1 uT

The resistance agrees well between the three approaches. Reactance is different because 4NEC assumes the antenna to be cylinder but Remcom modeled it to be flat.

The field is slightly different, which could be due to the same reason, plus the fact that Remcom uses copper instead of PEC.

It is clear that the small dipole shows better efficiency than the long dipole in terms of raw $B_1/\sqrt{\text{input_power}}$ efficiency, due to the more local power distribution. It is also shown that the $B_1/\sqrt{\text{SAR}_{10\text{g_max}}}$ of a short dipole is also comparable to that of the long dipole in depth of interest. And therefore, the short dipole is a viable option as a transmit element for spine/body imaging at 7T.

It needs to be noted that the $B_1/\sqrt{\text{input_power}}$ comparisons made in this section is taking into account the element only, and is not considering the potential losses in the matching network.

5.5 A Segmented Dipole Design with FCE and Selectable FOV for 7T Spine

Imaging

5.5.1 Introduction

Recently, a 37 cm dipole transmit element was demonstrated for spine imaging at 7T [35]. The design provides a large field of view (FOV) and demonstrates good radio frequency (RF) penetration. However, the current distribution on a dipole follows a sinusoidal distribution, and most of the power, in the form of magnetic field or electric field, is concentrated in the phantom underneath its center.

B_1 per unit maximum 10g averaged SAR ($B_1/\sqrt{\text{SAR}_{10\text{g_max}}}$) is an important figure of merit in high field RF coil design, and is extensively studied in multiple 7T research articles [91, 92, 97]. Because of its power distribution, the $B_1/\sqrt{\text{SAR}_{10\text{g_max}}}$ is intrinsically low towards the end of a long dipole. In other words, in order to get sufficient B_1 field towards the edge, one may have to allow high E field under the center of the dipole. The

length of patients' spine can vary significantly [98]. In order to investigate potential lesions at different locations on a spine without moving the patient, it is important to increase the $B_1/\sqrt{\text{SAR}_{10g_max}}$ efficiency at the edge of a long dipole. Furthermore, in 7T spine imaging it is often desirable to tailor the length of the coil, such that only the desired part of the spine (e.g. cervical, thoracic or lumbar zone) is excited, while redundant heat decomposition into other parts of the spine is avoided. To address these challenges, a segmented approach that allows adjustable FOV and reconfigurable power allocation can be utilized.

Although it is possible to use multiple power amplifiers and parallel transmission method to achieve adjustable field of view, the method is difficult to scale [30, 99]. For example, if we want to have two elements under the patient's spine, and have each of these elements segmented into three short elements in the z direction, the number of power amplifiers required is six, which is often not available at clinical sites. Even with enough power amplifiers, one still needs to consider decoupling strategies, which is a complicated topic by itself for dense transmit array [37, 38, 40-44, 46-48, 100, 101]. Instead, an approach that allows for adjustable FOV without the need for additional power amplifiers is desired.

A segmented dipole that uses PIN diode at various locations along the dipole has been reported, and has the capability to alter FOV [93]. However, the design requires the dipole be fed from the center of the entire dipole, limiting the variety of FOV that can be achieved. Previously we have reported a breast coil at 7T that allows switchable FOV [54, 55]. In this paper, using a similar principle, we present a design that provides a large FOV,

but also allows flexible FOV and power allocation switching. The method utilizes FCE, a method that guarantees equal current delivery to multiple elements [45]. With properly designed modification, the method enables switchable FOV, while maintaining the feature of FCE [54]. FCE feeding network has extra loss in the feed cables, but does not affect $B_1/\sqrt{\text{SAR}_{10g_max}}$ since the loss is not in the phantom.

Two types of coil element were compared in electromagnetic simulation to target for optimum $B_1/\sqrt{\text{SAR}_{10g_max}}$ efficiency for spine imaging. One of the elements was chosen as the final design, and was implemented and tested both on bench. The element was also tested with a phantom in a 7T body scanner.

5.5.2 Element Comparison

General description

Radiative dipole has been shown to have advantages over traditional elements such as loop coils and microstrip elements, in terms of $B_1/\sqrt{\text{SAR}_{10g_max}}$ efficiency or excitation pattern [97]. When it comes to spine imaging, element that is sufficiently long along the z direction is required. A long dipole, such as the one reported in [35], or a rung element, such as the one reported in [52], are possible candidates. Both elements can be segmented to enable switchable FOV. In this design, three segments along the z direction are used, with each element having their own feed.

The two types of elements, dipole and rung, were modeled and compared using full-wave electromagnetic simulation (Remcom XFDTD). In section 5.2, we already considered a few configurations with the rung element and determined that separate ground is required to achieve good decoupling. And for the dipole we only considered the

configuration where three short dipole are separated. In this section, two different configurations were considered: Having three separate short dipoles, separated by a smaller gap (same as section 5.2), or having adjacent dipoles sharing a leg. Separate dipoles and segmented dipoles were compared between themselves before being compared to the rung element.

To sum up, there are four cases that need to be compared before finalizing the design, as shown in Fig. 42:

- Case#1-Long dipole (Fig. 42(a)): A standard 37 cm long dipole [35], with 1.2 cm width and 2 mm gap between the legs, was modeled as the reference.
- Case#2-Separate rung element (Fig. 42(b)): Three separate rungs, each 11.6 cm long and 1.2 cm wide, was modeled. The total length of the structure is also 37 cm, same as reported in [94]. Each rung is 1.2 cm above a corresponding ground plane of the size 11.8 cm (z) x 15 cm (x). Each rung was segmented by 33pF distributed capacitors every 2cm.
- Case#3-Separate dipoles (Fig. 42(c)): Three separate dipoles, each 11.6 cm long and 1.2 cm wide, separated by 1.1 cm, was modeled. The total length of the structure is also 37 cm. All dipoles were fed from the middle.
- Case#4-Segmented dipoles (Fig. 42(d)): A 37 cm long, 1.2 cm wide dipole was segmented at three equally spaced locations, forming four pieces of conductors separated by three 2 mm gaps. In this case, each dipole segment is 18.4 cm, and the neighboring dipole elements share a mutual leg. Each dipole is fed from the corresponding gap.

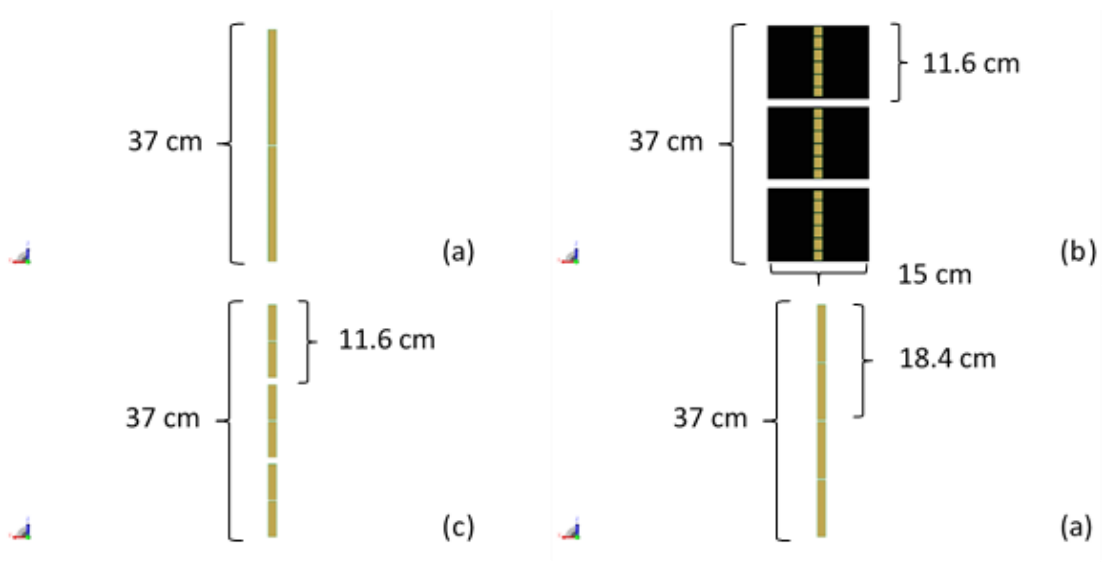


Fig. 42. Four different designs with the same overall length (37 cm), top view. Case 1 (a): standard dipole; Case 2 (b): separate rungs (ground is displayed as black); Case 3 (c): separate dipoles; Case 4 (d): segmented dipole

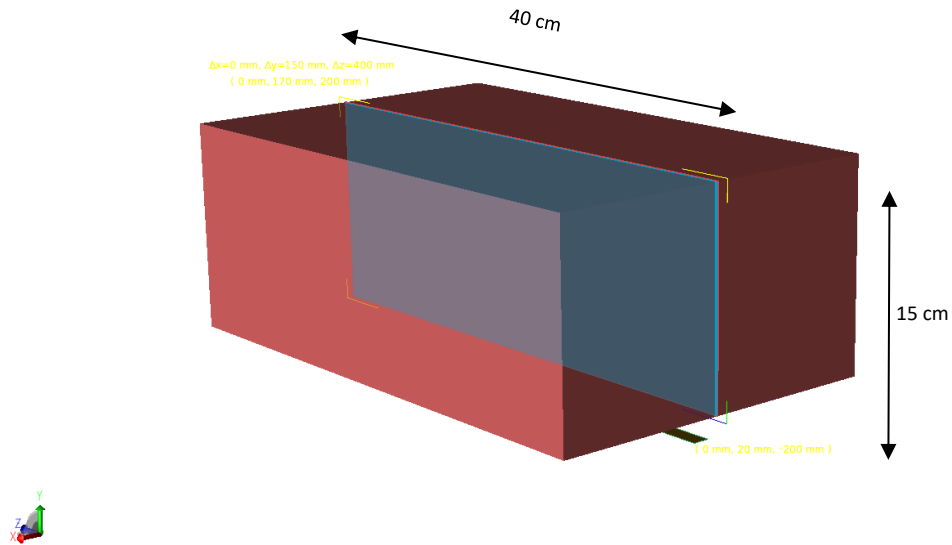


Fig. 43. Phantom model, and the sagittal plane where B_1 is calculated. The bore of the magnet is modeled but not displayed.

The phantom modeled is $25 \times 15 \times 40 \text{ cm}^3$ (X x Y x Z), with dielectric constant of 77 and conductivity of 0.6 S/m to approximate human muscle [97]. The phantom is placed 2 cm away in the y direction from the element (Fig. 43). The bore of the magnet, is model as a cylindrical copper sheet with a diameter of 59 cm.

In case# 2-4, the elements are designed to be driven by FCE. The FCE method uses quarter-wave transmission lines to connect from a common-voltage point to multiple coil elements. The current delivered to the coil elements are equal despite mutual coupling and difference in loading. In electromagnetic simulation, the feeds of the elements are modeled as high impedance (1000 ohm) current sources to simulate the forced-current condition. When simulating the coil in modes where only a few elements are used and the others are detuned, the activated elements were fed with the high impedance current source while the detuned elements are left open-circuited at their feeds, which also simulate the detuning capability of the FCE method [54, 84]. In case# 2-4, each element can be turned on or off and enables various modes: Namely, Mode A (-z element only), Mode B (z=0 element only), Mode C (+z element only), Mode A+B+C (all elements), as illustrated in Fig. 44.

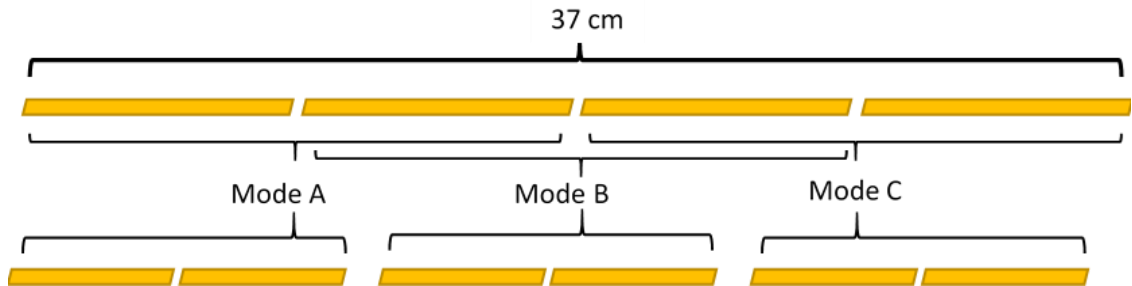


Fig. 44. Mode definition for segmented and separated configuration

In each case, B_1 field were calculated at the central sagittal plane, as is shown in Fig. 43.

Comparison between separated or segmented dipole

When using dipole as the element, we can either have the three short dipoles separated by a short gap, or have the adjacent dipoles sharing a leg. The two configurations have their own advantages and drawbacks.

The two different dipole configurations-separate and segmented were compared. The B_1 pattern in the central sagittal plane was calculated (Fig. 45).

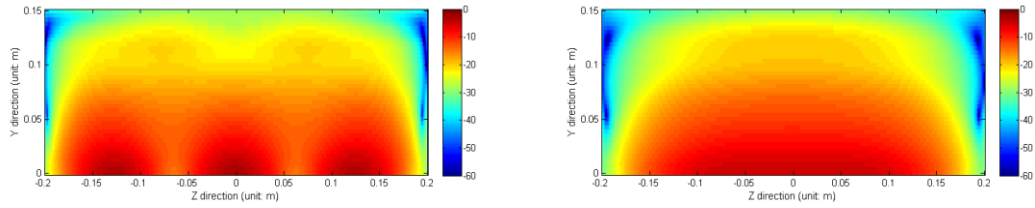


Fig. 45. (Top) Calculated B_1 pattern of the separate dipoles (case 3) and (Bottom) the segmented dipole (case 4) calculated from simulation. The segmented dipole provides a more continuous excitation pattern.

When mutual legs are shared between adjacent segmented dipoles, the current along the 37 cm dipole is more continuous and the B_1 field produced is more uniform, whereas the separate dipole configuration have current nulls between short dipoles. In this case, we chose the segmented dipole configuration over the separate dipole configuration for better B_1 pattern. However, it's worthy to note that the separate design allows more focused power decomposition in the short modes (Mode A, Mode B, Mode C), and therefore can achieve higher $B_1/\sqrt{\text{SAR}_{10g_max}}$ efficiency in local areas. Should the highest

$B_1/\sqrt{\text{SAR}_{10g_max}}$ efficiency be wanted in certain cases, the separate dipole configuration can still be a viable option.

Comparison between rung and dipole

A rung element operates in traditional quasi-static regime by breaking the long rung up by capacitors [52]. A dipole, on the other hand, was used due to its radiative behavior. Therefore, the two elements may behave differently in terms of RF penetration and field uniformity.

The $B_1/\sqrt{\text{SAR}_{10g_max}}$ efficiency was compared between the dipole and the rung element along the y direction. The comparison was made at the center location ($x=z=0$). In this comparison, the two elements are set to Mode B ($z=0$ element only). At this point the separate dipole configuration is no longer considered as an option for the final design, so the comparison to be made is between segmented dipole and rung element, which is case#2 and #4. $B_1/\sqrt{\text{SAR}_{10g_max}}$ efficiency vs. depth of case #2 and #4, operated in Mode B was compared at the center, as marked in Fig. 46.

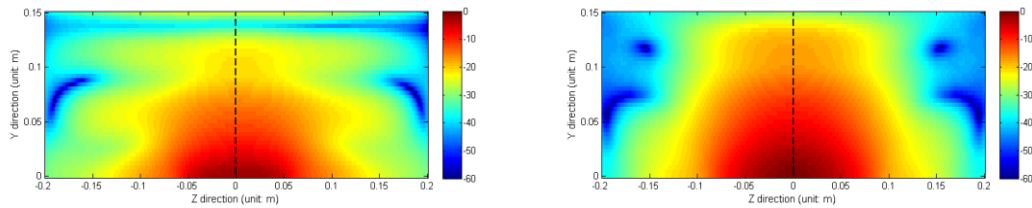


Fig. 46. Calculated $B_1/\sqrt{\text{SAR}_{10g_max}}$ pattern of the separate rung (Left) and the segmented dipole (Right) in the central sagittal plane. The y direction profiles where $B_1/\sqrt{\text{SAR}_{10g_max}}$ efficiency was compared are marked with dashed black line.

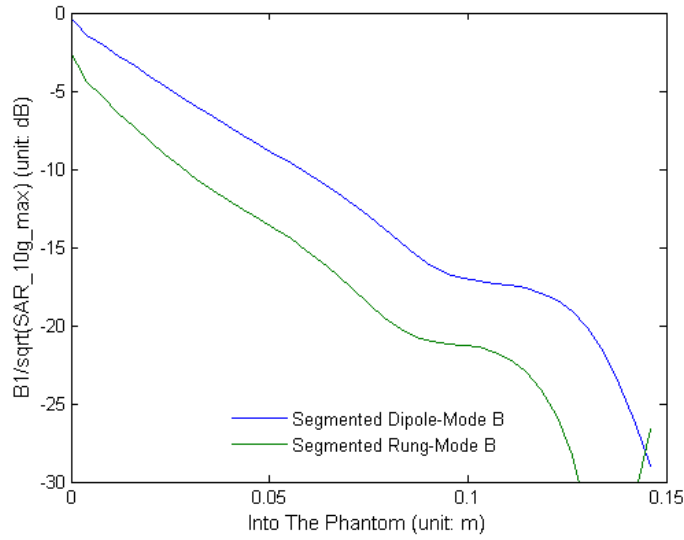


Fig. 47. Calculated $B_1/\sqrt{SAR_{10g_max}}$ efficiency comparison between the separated rung (Mode B) and the segmented dipole (Mode B). The profile position being compared was shown in Fig. 46.

Looking at the $B_1/\sqrt{SAR_{10g_max}}$ efficiency profile along the y direction vs depth, that of the rung element is significantly lower, especially at deeper locations. This is likely due to the current return pass provided by the ground plane and the B_1 field cancellation.

For the rung element, the field increased at the phantom-air interface. This is caused by the standing wave artifact, which appears to be more prominent with the rung element. For all other depth, the dipole has obvious advantage.

Accordingly, the segmented dipole, was chosen as the final configuration for the switchable transmit element.

Segmented dipole-Comparison between different modes

Once the segmented dipole was chosen as the final design, to demonstrate the effect from mode switching, the $B_1/\sqrt{\text{SAR}_{10\text{g_max}}}$ efficiency of the segmented dipole was compared to the standard dipole along the z direction at 5 cm deep into the phantom [35] in different modes.

A $B_1/\sqrt{\text{SAR}_{10\text{g_max}}}$ comparison was made in the z direction between all modes (Mode A~C, Mode A+B+C) and the standard dipole, as indicated by Fig. 48. The profile comparison is presented in Fig. 49.

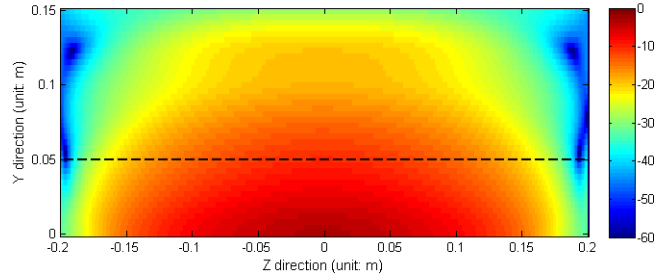


Fig. 48. Z direction profile being compared as marked in the calculated $B_1/\sqrt{\text{SAR}_{10\text{g_max}}}$ pattern of the reference standard dipole

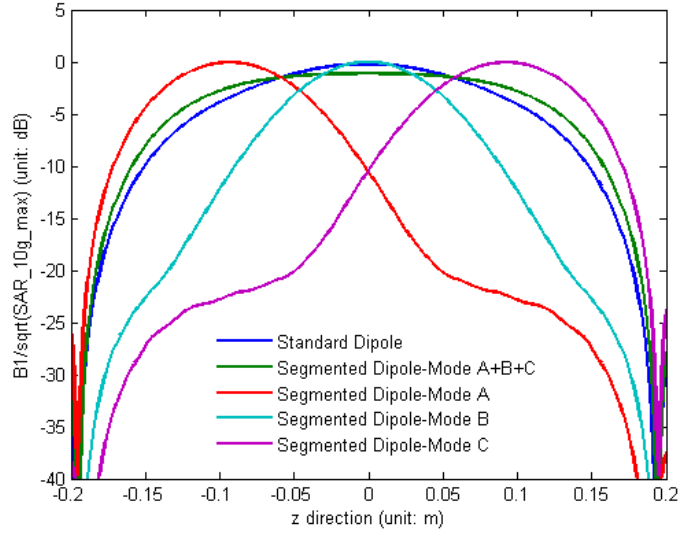


Fig. 49. Calculated z direction profile comparison at 5cm deep. Comparison was made between the segmented dipole in different modes and the standard dipole. The ability to switch FOV is observed.

The advantage of using a segmented design where each short element can be turned on and off, is obvious from Fig. 49. When switched to Mode A or C, the segmented design provides 0-4 dB higher $B_1/\sqrt{SAR_{10g_max}}$ efficiency than the standard dipole in the corresponding area.

5.5.3 Element Design and Implementation

The segmented dipole was etched on a 0.1" FR4 board, with the dimension described in Case#4. The common-voltage point (CVP) was upgraded to a PIN diode based switching circuit to enable mode switching.

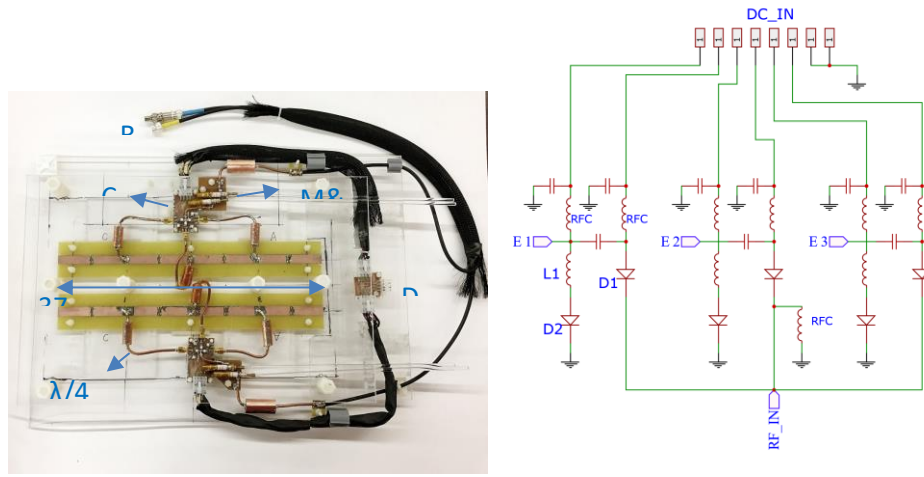


Fig. 50. Left: Layout of the coil, including the dipole, quarter-wave feedlines with baluns incorporated, switching circuit as well as matching circuit; Right: schematic of the switching circuit

The schematic of the switching circuit is provided in Fig. 50. The circuit determines the status (enabled or detuned) of each of the three coils through biasing two PIN diodes for each channel (take D1 and D2 for example). An external controller takes three ‘on-off’ digital signals and translates each one of them to two supply signals, which biases the two PIN diodes on the switching circuit. An ‘on’ signal drives a -5 V, 100 mA supply output and +35 V supply output, which forward biases D1 and reverse biases D2, respectively. D1 connects the quarter-wave feedline to the CVP, while D2 acts as an open circuit and does not affect the RF signal; On the other hand, a ‘off’ signal drives a +35 V supply output and a -5 V, 100 mA supply output, which reverse biases D1 and forward biases D2, respectively. D1 disconnects the quarter-wave feedline from the CVP, while D2 acts as a short circuit. The quarter-wave transmission line translates the short circuit to an open circuit at the coil feed, detuning that coil [54].

The layout of the switching circuit inevitably creates phase shift which will impact the FCE condition. The quarter wave coaxial lines (EZ-form-141), originally calculated as 17.6 cm, need to be shortened to compensate for that: The impedance at the CVP was monitored when a floating quarter wave feedline was connected to the switching circuit and an ‘on’, ‘off’, ‘off’ control signal was provided to channel A-C. The quarter-wave coax line was trimmed until a short circuit was observed on the network analyzer (HP 4195A). This process was repeated on all three feed cables.

D2 is designed to detune the unused coil by providing a short circuit at quarter-wave away from the coil. The impedance presented by D2 needs to be adjusted to compensate for the shortened quarter-wave cable: The trimmed quarter-wave coax line was connected to the switching circuit while the impedance at the other end of the cable is monitored. An ‘off’, ‘off’, ‘off’ control signal was provided to channel A-C. An inductor was added in series with D2, and its value was adjusted until an open circuit was observed on the network analyzer. This process was repeated on all three channels.

Capacitively terminated bazooka baluns were integrated onto the quarter-wave coax lines to reduce common mode current on its outside shield [102, 103]. A $\lambda/4$ bazooka balun is not used here because the actual length of the FCE feed cables are shorter than $\lambda/4$, as explained above. In order to reduce the coupling to the driven dipoles, the coax cables were arranged so that the majority of them lies on the equal-potential plane of the dipole (transverse plane in this case).

An identical segmented dipole element was later duplicated to target for better axial coverage, as is done in [35]. The spacing between the two coils is determined to be

6 cm according to [35]. Two standard dipoles [35] with the same dimensions were built for comparison.

5.5.4 Bench Measurement

The square root of SAR is linearly proportional to the electric field, and therefore $B_1/\sqrt{\text{SAR}_{10g_max}}$ efficiency of a coil is essentially a reflection of its $B_1/\max E$ field property [18]. The $B_1/\max E$ field of a coil is related to the performance of the coil element only, and is independent of its feeding network.

The FCE method introduces extra loss to the coil system due to the standing wave in the feed cables, which is not modeled in the simulation. It needs to be noted that the loss occurs in the feeding network, and does not affect the delivered $B_1/\max E$ field in the phantom.

The $B_1/\max E$ field was measured for the segmented dipole in Mode A, Mode B, Mode C, Mode A+B+C and for the reference standard dipole. The measurement was made at 5cm deep in the phantom (0.6 S/m saline water [97], same as used in the simulation) along the z direction, as is indicated in Fig. 48. The measurement was made using a shielded magnetic field probe [104], an E field probe [105] and a HP4195A network analyzer.

It is still of interest to know how much power is lost through the feeding network, so the $B_1/\sqrt{\text{input_power}}$ was also characterized for the elements compared, using a shielded magnetic field probe [104]. As opposed to $B_1/\max E$, when scaled to the same input power, the B_1 efficiency acquired is affected by the loss in the feeding network. The difference between the two measurements is the additional loss brought by FCE.

The $B_1/\max E$ field and $B_1/\sqrt{\text{input_power}}$ was measured for the segmented dipole in long mode, and was compared to the reference dipole. The difference between the two comparisons, was found to be 2.2 dB. This is the additional loss brought by the FCE feeding network, and is irrelevant to the $B_1/\sqrt{\text{SAR}_{10g_max}}$ or $B_1/\max E$ field performance.

The $B_1/\max E$ field measurement result is shown in Fig. 51. Due to the natural fall-off of the B_1 field around the edge of the standard long dipole, the segmented dipole in short modes exhibits 0~4 dB higher efficiency in the local area than the standard dipole. When set to the long mode, the segmented dipole has a flatter but longer profile than the standard dipole.

It is also obvious from the result that when operated in short mode, the other part of the segmented dipole is detuned. There is residual signal around the edge, due to the finite quality factor of the detuning circuit, but is at least 20 dB below the maximum signal. Therefore, unnecessary power decomposition into the unwanted area can be avoided.

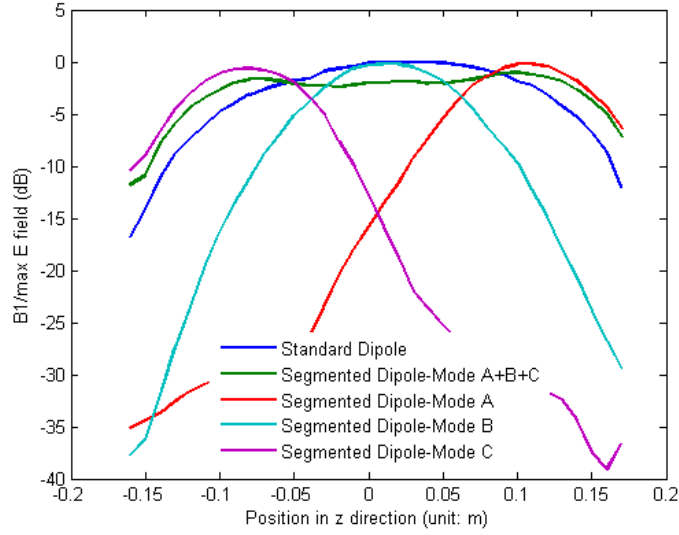


Fig. 51. $B_1/\max E$ results measured on bench at 5cm into the phantom. Comparison was made between the segmented dipole in different modes and the standard dipole

5.5.5 MR Experiment

As mentioned before, an identical segmented dipole element was duplicated to target for better axial coverage, as is done in [35]. The segmented dipoles were tested with a Philips 7T Achieva system in transmit/receive mode. The dipoles were loaded with 0.6 S/m saline water made into an agar gel phantom, placed 2 cm away from the dipoles.

It needs to be noted that although each segmented dipole was driven by FCE, the two dipoles together, were driven through a two-channel multi transmit system, where the phase of each dipole can be adjusted [35]. For the segmented dipole, the phase of the two channels were adjusted to find the optimum SNR at 5 cm into the phantom when the dipole was in Mode A. Once the optimum phase setting was found, the same setting was used for

all modes due to their intrinsic similarity. The same experiment was then repeated for the reference standard dipole set.

The segmented dipoles were tested in four modes-Mode A, Mode B, Mode C as well as Mode A+B+C. Mode A+B, Mode A+C and Mode B+C are possible but not measured. For each mode, sagittal T1-weighted fast gradient echo (THRIVE) images were obtained with the following scan parameters:

FOV 300 x 400 x 200 mm (RL x FH x AP), resolution 2 x 2 x 2 mm (overcontiguous), TR/TE/FA: 4.0 ms/0.97 ms/8°, for a total scan time of 0.58 minutes. The same experiment was then repeated for the reference dipole set.

In order to examine the $B_1/\sqrt{\text{input_power}}$ efficiency, flip angle series experiment was performed at a voxel of 2 x 2 x 2 cm³ at 5 cm into the phantom, directly underneath the center of the dipole set ($z=x=0$). This measurement does take into account the loss in the feeding network, and therefore is expected to be different than the $B_1/\sqrt{\text{SAR}_{10g_max}}$ results. The experiment was repeated for the standard dipole, the segmented dipole in the long mode (Mode A+B+C) and the short mode (Mode B). The drive scale (input power) was set to be a fixed value while the length of the RF excitation pulse was varied to search for the maximum response, which corresponds to a 90 degree flip angle. The TR used between RF pulses is 5 second to allow full T1 relaxation.

Axial coverage improvement by Multi-transmit

The segmented dipole has adjustable FOV and a large coverage in the long mode in the z direction, however its axial coverage is limited. Having two of them driven by two independent transmit channels greatly improves that. In optimizing the transmit phase for

the two channels, it was found that the maximum signal intensity at 5 cm into the phantom occurs with the phase setting of 0 and 90, which is in good agreement with the results presented in [35]. This applies to both the standard dipole and the segmented dipole. The improved axial coverage when driving two segmented dipoles is shown in Fig. 52.

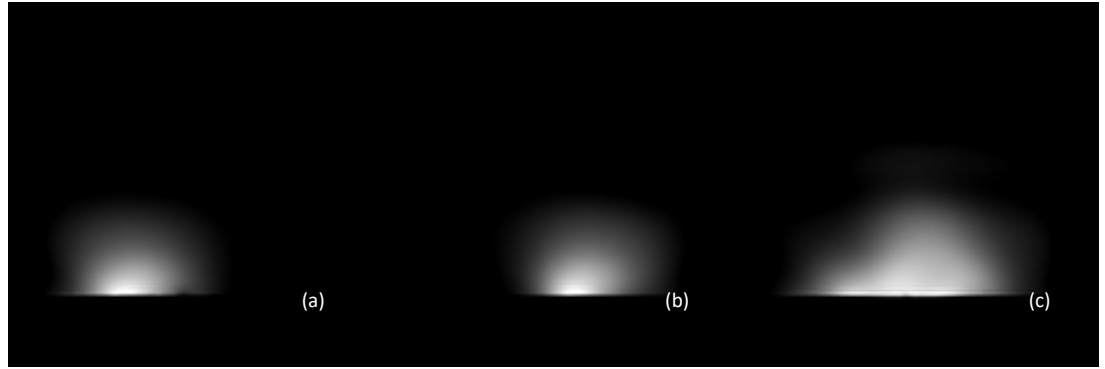


Fig. 52. Effect from using two dipoles together: (a) Axial image from segmented dipole element #1 (b) Axial image from segmented dipole element #2 (c) Axial image from two segmented dipoles transmitting at the same time. When two dipoles are used, the axial coverage is improved.

Sagittal images in all modes

The THRIVE images obtained in central sagittal plane under this configuration, is shown in Fig. 53.

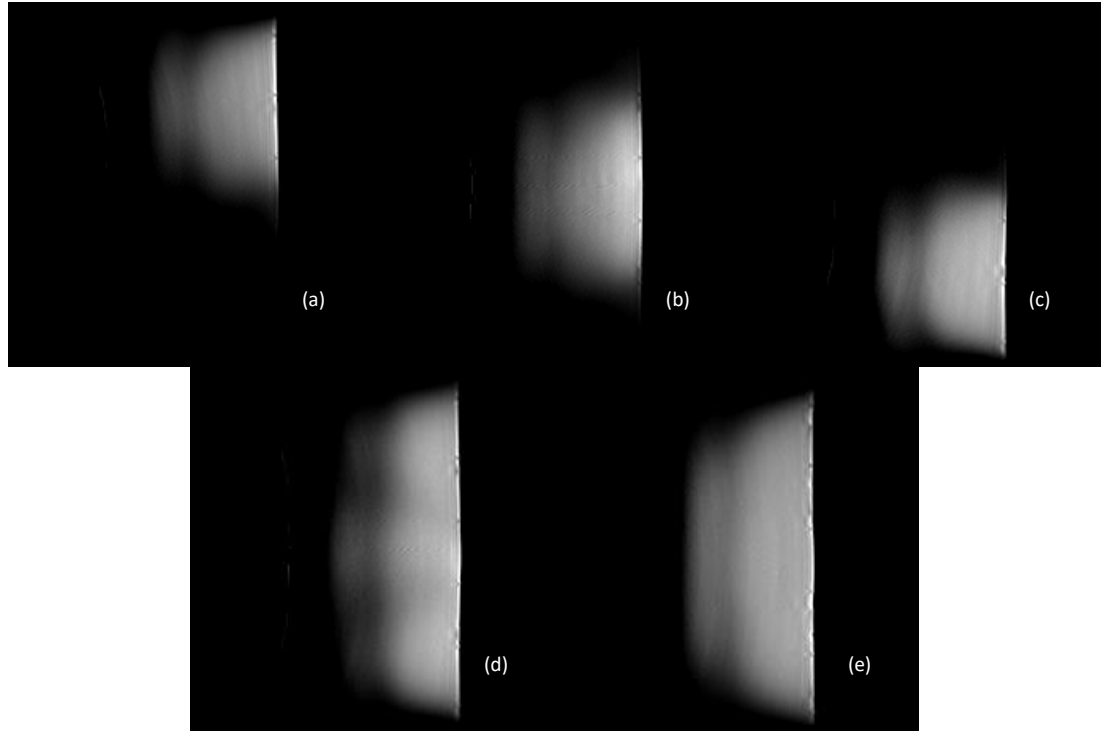


Fig. 53. Sagittal THRIVE images from the segmented dipoles (a-d) and the reference standard dipoles (e): (a) Segmented dipoles-Mode A. (b) Segmented dipoles-Mode B. (c) Segmented dipoles-Mode C. (d) Segmented dipoles-Mode A+B+C. (e) Reference standard dipoles. For the segmented dipole, in long mode, long coverage in z direction is achieved; In short mode, signal in the ‘off’ region is largely suppressed.

The axial images demonstrate good axial coverage in multi-transmit configuration. The sagittal images in different modes demonstrate successful mode-switching capability. In long mode, a large coverage in the z direction was obtained, and may be used as a survey mode in clinical applications; In short modes, the ability to smoothly shift the FOV is observed. The signal in the unwanted region is successfully suppressed.

The Flip angle series calibrating for a 90 degree flip angle at 5cm deep is performed on the segmented dipole (in long mode and in short mode) and the standard dipole. The drive scale (input power) was set to be a fixed value while the length of the RF excitation pulse linearly increases to search for the maximum response in each case. In each experiment, the length of the RF pulse increases linearly, giving a series of response spectrum. When the coil is more efficient, the maximum response (90 degree flip angle) would occur under a shorter RF pulse, at an earlier stage of the flip angle series. The result is presented in Fig. 54.

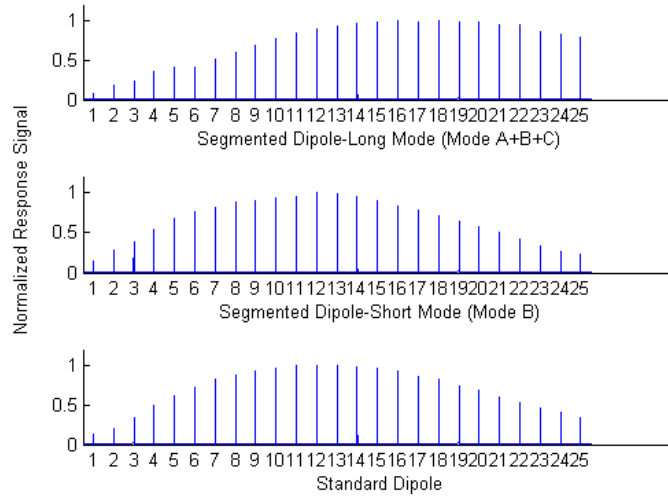


Fig. 54. Flip angle series experiment performed on the segmented dipole and the standard dipole. Horizontal axis indicates the pulse number in the series. The length of the RF pulse is linearly proportional to the pulse number. The maximum signal corresponds to 90 degree flip angle.

For the standard dipole, the 90 degree flip angle was found on pulse #12; For the segmented dipole, the 90 degree flip angle was found on pulse #18 for the long mode (Mode A+B+C), and on pulse #12 for the short mode (Mode B). Since the length of the RF pulse is linearly proportional to the pulse index, it can then be calculated that: In terms of $B_1/\sqrt{\text{input_power}}$ efficiency, the standard dipole is similar as the short mode in the segmented dipole, and is 1.5 times (3.5 dB) higher than the long mode in the segmented dipole. This difference includes the loss in the FCE network, and therefore is not the same as $B_1/\sqrt{\text{SAR}_{10\text{g_max}}}$, which was presented in Fig. 49 and Fig. 51.

5.5.6 Conclusions

Long dipoles have been used for spine imaging. The low $B_1/\sqrt{\text{SAR}_{10\text{g_max}}}$ efficiency towards the end of the dipole calls for a flexible design where segments of a long structure can be turned on and off to manipulate the power distribution.

In this work, several design options for a switchable FOV, long element targeted for 7T spine imaging were compared in simulation. A long dipole, segmented into three smaller, overlapping dipoles was chosen as the final design. The flexible design allows higher $B_1/\sqrt{\text{SAR}_{10\text{g_max}}}$ towards the end of the dipole. The segmented dipole was implemented by utilizing FCE and a PIN-diode switching circuit. Each segment of the dipole can be activated or detuned by an electronic control.

The segmented dipole was evaluated on bench and on a phantom in a 7T body scanner. It was also compared to the standard dipole that has been published. The FCE feeding network does bring extra loss to the segmented dipole, especially in the long mode. However, the loss is restrained in the circuit instead of the phantom, and therefore does

not affect the $B_1/\sqrt{\text{SAR}_{10\text{g_max}}}$ efficiency. The next step is to investigate methods to improve the raw $B_1/\sqrt{\text{input_power}}$ efficiency, which may require the use of bigger coaxial cables or partially matching the dipoles before the $\lambda/4$ cables.

The design of the FCE configuration and the switching circuit layout is independent of the coil element used. In other words, one can use any coil element desired. In this case, a segmented dipole configuration was selected to obtain uniform excitation and continuous FOV switching.

CHAPTER VI

CONCLUSIONS AND DISCUSSIONS

6.1 Conclusions

MRI/MRS at 7T faces many challenges. Reduced RF wavelength and phase interference often calls for the use of multiple elements in a coil. Controlling the current across the elements is challenging due to mutual coupling between them. 7T breast imaging and spine imaging is particularly challenging also due to the large FOV required. In addition, the ability to switch FOV without using multiple expensive power amplifiers is desired in these applications. Switching to a smaller FOV will improve power efficiency in the local area while avoiding power deposition in areas not of interest.

The theory of FCE is analyzed in this dissertation using ABCD matrices. The method delivers equal current to multiple elements despite mutual coupling. The upgrade of the FCE configuration enables each element to be turned on and off with the inclusion of PIN diodes and biasing circuits, enabling switchable FOV. The FCE feeding network introduces extra losses due to the standing wave formed in the cable. This loss can be quantified with known attenuation, cable length and coil impedance, and can potentially be compensated for by partially matching the coil, use low loss cables, etc.

A switchable unilateral/bilateral breast coil at 7T was designed and implemented under the ‘FCE+switchable FOV’ principle. The coil can be switched electronically between unilateral mode or bilateral mode. The coil was investigated through EM simulations, bench measurements and MR experiments. Uniform excitation was found in

all modes due to the use of FCE. In particular, symmetric performance was found in bilateral mode, and excellent signal localization is seen in unilateral mode with the contralateral signal largely suppressed. In unilateral mode, the coil is found to be about 3 dB more efficient than bilateral mode in terms of $B_1/\sqrt{\text{input_power}}$. This can potentially be useful in power-demanding applications such as proton-decoupled spectroscopy in a unilateral breast. $B_1/\sqrt{\text{SAR}_{10\text{g_max}}}$ efficiency of the coil does not change with mode switching, as the two coils have identical structures.

A modified version of the bilateral coil was implemented specifically for the insertion of a 32-channel receive array. Shielded twinaxial cables were used on this coil as the FCE feed cables to avoid the need for baluns or a RF shield, creating room for array insertion. This coil provides uniform excitation as tested through MR experiments and houses the receive array successfully.

A segmented dipole at 7T for spine imaging was designed and implemented under the ‘FCE+switchable FOV’ principle. A dipole was selected due to improved penetration, when compared to a rung. The segmented dipole has a total of three segments, with the adjacent elements sharing a mutual leg. Each element can be turned on or off by the switching network, giving a switchable FOV. The segmented dipole was investigated in simulation, on bench and through MR experiments using a phantom, and was compared to a regular dipole of the same total length. When operated in long mode, the segmented dipole provides large FOV due to FCE. In short mode, the signal other regions are largely suppressed, and the FOV can be smoothly shifted when switching between the short modes. The ability to switch FOV and adjust power distribution gives the segmented

dipole 0~4 dB advantage over the regular dipole in terms of $B_1/\sqrt{\text{SAR}_{10\text{g_max}}}$ efficiency. The use of FCE degrades the $B_1/\sqrt{\text{input_power}}$ performance due to the remote matching network. It was found that in the short mode, the segmented dipole is as efficient as the regular dipole in terms of $B_1/\sqrt{\text{input_power}}$ efficiency; In long mode, the segmented dipole is 3.5 dB less efficient due to the introduced loss. Of particular note is that the loss is restricted in the feeding network, not in the phantom, so the $B_1/\sqrt{\text{SAR}_{10\text{g_max}}}$ efficiency is not affected. Possible means of alleviating this loss is summarized in section 6.2.

6.2 Possible Improvements

As discussed in section 3.4, the FCE feeding network introduces loss to the system. Reducing this loss involves 1. Reducing the attenuation of the $\lambda/4$ transmission lines (Use lower-loss cables); 2. Reducing the reflection coefficient at the element feed. Partially matching the coil should drive down the reflection coefficient and reduce the overall loss. However, only a series element can be used for this purpose, given that a shunt element could cause the ‘forced current’ at the coil feed to be split between that and the coil.

With the switching capability integrated, it was found that coil in different modes could present different impedance to the matching circuit, requiring retuning in different modes. Section 4.4 describes a potential method to alleviate this effect by having two coils sharing a mutual reactive element. This may be employed in future FCE coils to avoid retuning. A further upgrade of the switched-mode coil may involve the use of smart devices, such as microprocessors, to automatically determine the desired mode based on

the coil location and the pulse sequence, and to provide the capability of switching during the sequence.

REFERENCES

- [1] A. Blamire, “The technology of MRI—the next 10 years?,” *The British Journal of Radiology*, vol. 81, no. 968, pp. 601-617, 2014.
- [2] J. Alvarez-Linera, “3T MRI: advances in brain imaging,” *European Journal of Radiology*, vol. 67, no. 3, pp. 415-426, 2008.
- [3] V. S. Lee, E. M. Hecht, B. Taouli, Q. Chen, K. Prince, and N. Oesingmann, “Body and Cardiovascular MR Imaging at 3.0 T 1,” *Radiology*, vol. 244, no. 3, pp. 692-705, 2007.
- [4] W. A. Edelstein, G. H. Glover, C. J. Hardy, and R. W. Redington, “The intrinsic signal-to-noise ratio in NMR imaging,” *Magnetic Resonance in Medicine*, vol. 3, no. 4, pp. 604-618, 1986.
- [5] R. Mekanle, V. Mlynárik, G. Gambarota, M. Hergt, G. Krueger, and R. Gruetter, “MR spectroscopy of the human brain with enhanced signal intensity at ultrashort echo times on a clinical platform at 3T and 7T,” *Magnetic Resonance in Medicine*, vol. 61, no. 6, pp. 1279-1285, 2009.
- [6] R. Brown, P. Storey, C. Geppert, K. McGorty, A. P. K. Leite, J. Babb, D. K. Sodickson, G. C. Wiggins, and L. Moy, “Breast MRI at 7 Tesla with a bilateral coil and T1-weighted acquisition with robust fat suppression: image evaluation and comparison with 3 Tesla,” *European Radiology*, vol. 23, no. 11, pp. 2969-2978, 2013.
- [7] A. G. van der Kolk, J. Hendrikse, J. J. M. Zwanenburg, F. Visser, and P. R. Luijten, “Clinical applications of 7 T MRI in the brain,” *European Journal of Radiology*, vol. 82, no. 5, pp. 708-718, 2013.
- [8] P.-F. Van de Moortele, C. Akgun, G. Adriany, S. Moeller, J. Ritter, C. M. Collins, M. B. Smith, J. T. Vaughan, and K. Ugurbil, “B1 destructive interferences and spatial phase patterns at 7 T with a head transceiver array coil,” *Magnetic Resonance in Medicine*, vol. 54, no. 6, pp. 1503-1518, 2005.
- [9] D. Hoult, and P. C. Lauterbur, “The sensitivity of the zeugmatographic experiment involving human samples,” *Journal of Magnetic Resonance (1969)*, vol. 34, no. 2, pp. 425-433, 1979.
- [10] L. Umutlu, S. Maderwald, O. Kraff, J. M. Theysohn, S. Kuemmel, E. A. Hauth, M. Forsting, G. Antoch, M. E. Ladd, H. H. Quick, and T. C. Lauenstein, “Dynamic Contrast-Enhanced Breast MRI at 7 Tesla Utilizing a Single-loop Coil: A Feasibility Trial,” *Academic Radiology*, vol. 17, no. 8, pp. 1050-1056, 2010.

- [11] B. Wu, C. Wang, R. Krug, D. A. Kelley, D. Xu, Y. Pang, S. Banerjee, D. B. Vigneron, S. J. Nelson, and S. Majumdar, "7T human spine imaging arrays with adjustable inductive decoupling," *IEEE Transactions on Biomedical Engineering*, vol. 57, no. 2, pp. 397-403, 2010.
- [12] E. R. Andrew, "Nuclear magnetic resonance," *American Journal of Physics*, vol. 24, no. 5, pp. 417-418, 1956.
- [13] J. L. Evelhoch, and J. J. H. Ackerman, "NMR T1 measurements in inhomogeneous B1 with surface coils," *Journal of Magnetic Resonance (1969)*, vol. 53, no. 1, pp. 52-64, 1983.
- [14] S. M. Wright, and L. L. Wald, "Theory and application of array coils in MR spectroscopy," *NMR in Biomedicine*, vol. 10, no. 8, pp. 394-410, 1997.
- [15] P. B. Roemer, W. A. Edelstein, C. E. Hayes, S. P. Souza, and O. Mueller, "The NMR phased array," *Magnetic Resonance in Medicine*, vol. 16, no. 2, pp. 192-225, 1990.
- [16] P. C. Lauterbur, "Image formation by induced local interactions: examples employing nuclear magnetic resonance," *Nature*, vol. 242, pp. 190-191, 1973.
- [17] W. A. Edelstein, J. M. Hutchison, G. Johnson, and T. Redpath, "Spin warp NMR imaging and applications to human whole-body imaging," *Physics in Medicine and Biology*, vol. 25, no. 4, pp. 751, 1980.
- [18] J. Jin, *Electromagnetic analysis and design in magnetic resonance imaging*, Boca Raton, Florida: CRC press, 1998.
- [19] T. Ibrahim, R. Lee, B. Baertlein, and P. L. Robitaille, "B1 field homogeneity and SAR calculations for the birdcage coil," *Physics in Medicine and Biology*, vol. 46, no. 2, pp. 609, 2001.
- [20] P. Dimbylow, "FDTD calculations of the whole-body averaged SAR in an anatomically realistic voxel model of the human body from 1 MHz to 1 GHz," *Physics in Medicine and Biology*, vol. 42, no. 3, pp. 479, 1997.
- [21] A. Taflove, and S. C. Hagness, *Computational Electrodynamics*, Boston, Massachusetts: Artech house, 2005.
- [22] K. Yee, "Numerical solution of initial boundary value problems involving Maxwell's equations in isotropic media," *IEEE Transactions on Antennas and Propagation*, vol. 14, no. 3, pp. 302-307, 1966.

- [23] R. Otazo, B. Mueller, K. Ugurbil, L. Wald, and S. Posse, "Signal - to - noise ratio and spectral linewidth improvements between 1.5 and 7 Tesla in proton echo - planar spectroscopic imaging," *Magnetic Resonance in Medicine*, vol. 56, no. 6, pp. 1200-1210, 2006.
- [24] J. T. Vaughan, C. J. Snyder, L. J. DelaBarre, P. J. Bolan, J. Tian, L. Bolinger, G. Adriany, P. Andersen, J. Strupp, and K. Ugurbil, "Whole - body imaging at 7T: Preliminary results," *Magnetic Resonance in Medicine*, vol. 61, no. 1, pp. 244-248, 2009.
- [25] J. T. Vaughan, M. Garwood, C. Collins, W. Liu, L. DelaBarre, G. Adriany, P. Andersen, H. Merkle, R. Goebel, and M. Smith, "7T vs. 4T: RF power, homogeneity, and signal - to - noise comparison in head images," *Magnetic Resonance in Medicine*, vol. 46, no. 1, pp. 24-30, 2001.
- [26] V. de Moortele, C. Akgun, G. Adriany, S. Moeller, J. Ritter, C. M. Collins, M. B. Smith, J. T. Vaughan, and K. Ugurbil, "B1 destructive interferences and spatial phase patterns at 7 T with a head transceiver array coil," *Magnetic Resonance in Medicine*, vol. 54, no. 6, pp. 1503-1518, 2005.
- [27] C. M. Collins, W. Liu, W. Schreiber, Q. X. Yang, and M. B. Smith, "Central brightening due to constructive interference with, without, and despite dielectric resonance," *Journal of Magnetic Resonance Imaging*, vol. 21, no. 2, pp. 192-196, 2005.
- [28] B. van den Bergen, C. A. Van den Berg, L. W. Bartels, and J. J. Lagendijk, "7 T body MRI: B1 shimming with simultaneous SAR reduction," *Physics in Medicine and Biology*, vol. 52, no. 17, pp. 5429, 2007.
- [29] Y. Zhu, "Parallel excitation with an array of transmit coils," *Magnetic Resonance in Medicine*, vol. 51, no. 4, pp. 775-784, 2004.
- [30] U. Katscher, and P. Börnert, "Parallel RF transmission in MRI," *NMR in Biomedicine*, vol. 19, no. 3, pp. 393-400, 2006.
- [31] R. Brown, P. Storey, C. Geppert, K. McGorty, A. P. Klautau Leite, J. Babb, D. K. Sodickson, G. C. Wiggins, and L. Moy, "Breast MRI at 7 Tesla with a bilateral coil and robust fat suppression," *Journal of Magnetic Resonance Imaging*, vol. 39, no. 3, pp. 540-549, 2014.
- [32] C. D. Lehman, C. Gatsonis, C. K. Kuhl, R. E. Hendrick, E. D. Pisano, L. Hanna, S. Peacock, S. F. Smazal, D. D. Maki, and T. B. Julian, "MRI evaluation of the contralateral breast in women with recently diagnosed breast cancer," *New England Journal of Medicine*, vol. 356, no. 13, pp. 1295-1303, 2007.

- [33] E. S. Roig, A. W. Magill, G. Donati, M. Meyerspeer, L. Xin, O. Ipek, and R. Gruetter, "A double - quadrature radiofrequency coil design for proton - decoupled carbon - 13 magnetic resonance spectroscopy in humans at 7T," *Magnetic Resonance in Medicine*, vol. 73, no. 2, pp. 894-900, 2015.
- [34] H. Ko, J. Park, Y. Shin, and S. Baek, "Gross quantitative measurements of spinal cord segments in human," *Spinal Cord*, vol. 42, no. 1, pp. 35-40, 2004.
- [35] Q. Duan, G. Nair, N. Gudino, J. A. De Zwart, P. Van Gelderen, J. Murphy - Boesch, D. S. Reich, J. H. Duyn, and H. Merkle, "A 7T spine array based on electric dipole transmitters," *Magnetic Resonance in Medicine*, vol. 74, no. 4, pp. 1189-1197, 2015.
- [36] A. Reykowski, S. M. Wright, and J. R. Porter, "Design of matching networks for low noise preamplifiers," *Magnetic Resonance in Medicine*, vol. 33, no. 6, pp. 848-852, 1995.
- [37] C. Von Morze, J. Tropp, S. Banerjee, D. Xu, K. Karpodinis, L. Carvajal, C. P. Hess, P. Mukherjee, S. Majumdar, and D. B. Vigneron, "An eight - channel, nonoverlapping phased array coil with capacitive decoupling for parallel MRI at 3 T," *Concepts in Magnetic Resonance Part B: Magnetic Resonance Engineering*, vol. 31, no. 1, pp. 37-43, 2007.
- [38] B. Wu, P. Qu, C. Wang, J. Yuan, and G. X. Shen, "Interconnecting L/C components for decoupling and its application to low - field open MRI array," *Concepts in Magnetic Resonance Part B: Magnetic Resonance Engineering*, vol. 31, no. 2, pp. 116-126, 2007.
- [39] B. Wu, X. Zhang, P. Qu, and G. X. Shen, "Design of an inductively decoupled microstrip array at 9.4 T," *Journal of Magnetic Resonance*, vol. 182, no. 1, pp. 126-132, 2006.
- [40] J. Jevtic, "Ladder networks for capacitive decoupling in phased-array coils," *Pro Int Soc Mag Reson Med*, pp. 17, 2001.
- [41] R. F. Lee, R. O. Giaquinto, and C. J. Hardy, "Coupling and decoupling theory and its application to the MRI phased array," *Magnetic Resonance in Medicine*, vol. 48, no. 1, pp. 203-213, 2002.
- [42] R. F. Lee, C. R. Westgate, R. G. Weiss, D. C. Newman, and P. A. Bottomley, "Planar strip array (PSA) for MRI," *Magnetic Resonance in Medicine*, vol. 45, no. 4, pp. 673-683, 2001.

- [43] Y. Li, Z. Xie, Y. Pang, D. Vigneron, and X. Zhang, "ICE decoupling technique for RF coil array designs," *Medical Physics*, vol. 38, no. 7, pp. 4086-4093, 2011.
- [44] N. I. Avdievich, J. W. Pan, and H. P. Hetherington, "Resonant inductive decoupling (RID) for transceiver arrays to compensate for both reactive and resistive components of the mutual impedance," *NMR in Biomedicine*, vol. 26, no. 11, pp. 1547-1554, 2013.
- [45] M. P. McDougall, J. M. Knight, E. E. Eigenbrodt, S. M. Wright, and C.-W. Chang, "A simple approach to overcoming mutual coupling effects in some transmit array coils for magnetic resonance imaging," *Conf Proc IEEE Eng Med Biol Soc*, pp. 2043-2046, 2008.
- [46] D. Hoult, G. Kolansky, D. Kripiakevich, and S. King, "The NMR multi-transmit phased array: a Cartesian feedback approach," *Journal of Magnetic Resonance*, vol. 171, no. 1, pp. 64-70, 2004.
- [47] K. N. Kurpad, S. M. Wright, and E. B. Boskamp, "RF current element design for independent control of current amplitude and phase in transmit phased arrays," *Concepts in Magnetic Resonance Part B: Magnetic Resonance Engineering*, vol. 29, no. 2, pp. 75-83, 2006.
- [48] X. Chu, X. Yang, Y. Liu, J. Sabate, and Y. Zhu, "Ultra - low output impedance RF power amplifier for parallel excitation," *Magnetic Resonance in Medicine*, vol. 61, no. 4, pp. 952-961, 2009.
- [49] N. Gudino, J. A. Heilman, M. J. Riffe, O. Heid, M. Vester, and M. A. Griswold, "On - coil multiple channel transmit system based on class - D amplification and pre - amplification with current amplitude feedback," *Magnetic Resonance in Medicine*, vol. 70, no. 1, pp. 276-289, 2013.
- [50] R. Luebbers, and H. Langdon, "A simple feed model that reduces time steps needed for FDTD antenna and microstrip calculations," *IEEE Transactions on Antennas and propagation*, vol. 44, no. 7, pp. 1000-1005, 1996.
- [51] M. Celuch-Marcysiak, and W. Gwarek, "A novel variable source impedance technique for emulating unperturbed eigenmodes in the FD-TD method," *Computation in Electromagnetics, Third International Conference on* pp. 277-282, 1996.
- [52] K. L. Moody, N. A. Hollingsworth, F. Zhao, J.-F. Nielsen, D. C. Noll, S. M. Wright, and M. P. McDougall, "An eight-channel T/R head coil for parallel transmit MRI at 3T using ultra-low output impedance amplifiers," *Journal of Magnetic Resonance*, vol. 246, pp. 62-68, 2014.

- [53] D. M. Pozar, *Microwave engineering*, Hoboken, New Jersey: John Wiley & Sons, 2009.
- [54] J. Cui, J. C. Bosshard, J. V. Rispoli, I. E. Dimitrov, S. Cheshkov, M. P. McDougall, C. Malloy, and S. M. Wright, "A Switched-Mode Breast Coil for 7 T MRI Using Forced-Current Excitation," *IEEE Transactions on Biomedical Engineering*, vol. 62, no. 7, pp. 1777-1783, 2015.
- [55] J. Cui, I. Dimitrov, S. Cheshkov, M. P. McDougall, C. Malloy, and S. M. Wright, "Switchable bilateral/unilateral 7T breast coil using forced current excitation," *Pro Int Soc Mag Reson Med*, pp. 2727, 2013.
- [56] J. Cui, R. D. Bosque, I. Dimitrov, S. Cheshkov, M. P. McDougall, C. Malloy, and S. M. Wright, "Modified FCE Transmit Coil for Bilateral Breast Imaging at 7T with Array Coil Inserts," *Pro Int Soc Mag Reson Med*, pp. 2706, 2017.
- [57] G. Adriany, V. de Moortele, F. Wiesinger, S. Moeller, J. P. Strupp, P. Andersen, C. Snyder, X. Zhang, W. Chen, and K. P. Pruessmann, "Transmit and receive transmission line arrays for 7 Tesla parallel imaging," *Magnetic Resonance in Medicine*, vol. 53, no. 2, pp. 434-445, 2005.
- [58] M. A. Korteweg, W. B. Veldhuis, F. Visser, P. R. Luijten, P. T. M. Willem, P. J. van Diest, M. A. van den Bosch, and D. J. Klomp, "Feasibility of 7 Tesla breast magnetic resonance imaging determination of intrinsic sensitivity and high-resolution magnetic resonance imaging, diffusion-weighted imaging, and ¹H-magnetic resonance spectroscopy of breast cancer patients receiving neoadjuvant therapy," *Investigative Radiology*, vol. 46, no. 6, pp. 370-376, 2011.
- [59] O. Kraff, A. Fischer, A. M. Nagel, C. Mönninghoff, and M. E. Ladd, "MRI at 7 tesla and above: Demonstrated and potential capabilities," *Journal of Magnetic Resonance Imaging*, vol. 41, no. 1, pp. 13-33, 2015.
- [60] B. Wu, C. Wang, D. A. Kelley, D. Xu, D. B. Vigneron, S. J. Nelson, and X. Zhang, "Shielded microstrip array for 7T human MR imaging," *IEEE Transactions on Medical Imaging*, vol. 29, no. 1, pp. 179-184, 2010.
- [61] I. E. Dimitrov, D. Douglas, J. Ren, N. B. Smith, A. G. Webb, A. D. Sherry, and C. R. Malloy, "In vivo determination of human breast fat composition by ¹H magnetic resonance spectroscopy at 7 T," *Magnetic Resonance in Medicine*, vol. 67, no. 1, pp. 20-26, 2012.
- [62] B. L. Stehouwer, D. W. Klomp, M. A. Korteweg, H. M. Verkooijen, P. R. Luijten, W. P. T. M. Mali, M. A. van den Bosch, and W. B. Veldhuis, "7T versus 3T contrast-enhanced breast Magnetic Resonance Imaging of invasive ductulobular

- carcinoma: first clinical experience,” *Magnetic Resonance Imaging*, vol. 31, no. 4, pp. 613-617, 2013.
- [63] B. L. Stehouwer, D. W. Klomp, M. A. van den Bosch, M. A. Korteweg, K. G. Gilhuijs, A. J. Witkamp, P. J. van Diest, K. A. Houwert, W. J. van der Kemp, and P. R. Luijten, “Dynamic contrast-enhanced and ultra-high-resolution breast MRI at 7.0 Tesla,” *European Radiology*, vol. 23, no. 11, pp. 2961-2968, 2013.
 - [64] J. P. Wijnen, W. J. van der Kemp, M. P. Luttje, M. A. Korteweg, P. R. Luijten, and D. W. Klomp, “Quantitative ^{31}P magnetic resonance spectroscopy of the human breast at 7 T,” *Magnetic Resonance in Medicine*, vol. 68, no. 2, pp. 339-348, 2012.
 - [65] D. W. Klomp, B. L. van de Bank, A. Raaijmakers, M. A. Korteweg, C. Possanzini, V. O. Boer, C. A. van de Berg, M. A. van de Bosch, and P. R. Luijten, “ ^{31}P MRSI and ^1H MRS at 7 T: initial results in human breast cancer,” *NMR in Biomedicine*, vol. 24, no. 10, pp. 1337-1342, 2011.
 - [66] K. Pinker, W. Bogner, P. Baltzer, S. Trattnig, S. Gruber, O. Abeyakoon, M. Bernathova, O. Zaric, P. Dubskey, and Z. Bago-Horvath, “Clinical application of bilateral high temporal and spatial resolution dynamic contrast-enhanced magnetic resonance imaging of the breast at 7 T,” *European Radiology*, vol. 24, no. 4, pp. 913-920, 2013.
 - [67] W. Mao, M. B. Smith, and C. M. Collins, “Exploring the limits of RF shimming for high - field MRI of the human head,” *Magnetic Resonance in Medicine*, vol. 56, no. 4, pp. 918-922, 2006.
 - [68] F. Schick, “Whole-body MRI at high field: technical limits and clinical potential,” *European Radiology*, vol. 15, no. 5, pp. 946-959, 2005.
 - [69] U. Katscher, P. Boernert, C. Leussler, and J. S. Van Den Brink, “Transmit sense,” *Magnetic Resonance in Medicine*, vol. 49, no. 1, pp. 144-150, 2003.
 - [70] G. Adriany, V. de Moortele, J. Ritter, S. Moeller, E. J. Auerbach, C. Akgün, C. J. Snyder, T. Vaughan, and K. Ugurbil, “A geometrically adjustable 16 - channel transmit/receive transmission line array for improved RF efficiency and parallel imaging performance at 7 Tesla,” *Magnetic Resonance in Medicine*, vol. 59, no. 3, pp. 590-597, 2008.
 - [71] K. Feng, N. A. Hollingsworth, M. P. McDougall, and S. M. Wright, “A 64-Channel Transmitter for Investigating Parallel Transmit MRI,” *Biomedical Engineering, IEEE Transactions on*, vol. 59, no. 8, pp. 2152-2160, 2012.

- [72] L. L. Wald, and E. Adalsteinsson, "Parallel transmit technology for high field MRI," *MAGNETOM Flash*, vol. 40, no. 1, 2009.
- [73] M. P. McDougall, S. Cheshkov, J. Rispoli, C. Malloy, I. Dimitrov, and S. M. Wright, "Quadrature transmit coil for breast imaging at 7 tesla using forced current excitation for improved homogeneity," *Journal of Magnetic Resonance Imaging*, vol. 40, no. 5, pp. 1165-1173, 2014.
- [74] P. D. Friedman, S. V. Swaminathan, K. Herman, and L. Kalisher, "Breast MRI: the importance of bilateral imaging," *American Journal of Roentgenology*, vol. 187, no. 2, pp. 345-349, 2006.
- [75] R. Brown, P. Storey, C. Geppert, K. McGorty, A. P. K. Leite, J. Babb, D. K. Sodickson, G. C. Wiggins, and L. Moy, "Breast MRI at 7 Tesla with a bilateral coil and T1-weighted acquisition with robust fat suppression: image evaluation and comparison with 3 Tesla," *European Radiology*, vol. 23, no. 11, pp. 2969-2978, 2013.
- [76] L. Liberman, E. A. Morris, C. M. Kim, J. B. Kaplan, A. F. Abramson, J. H. Menell, K. J. Van Zee, and D. D. Dershaw, "MR imaging findings in the contralateral breast of women with recently diagnosed breast cancer," *American Journal of Roentgenology*, vol. 180, no. 2, pp. 333-341, 2003.
- [77] S. Cheshkov, I. Dimitrov, and J. V. Rispoli, "Proton decoupled ^{13}C MRS of the breast at 7T," *Pro Int Soc Mag Reson Med*, pp. 4428, 2012.
- [78] D. Doddrell, V. Glushko, and A. Allerhand, "Theory of Nuclear Overhauser Enhancement and ^{13}C - ^1H Dipolar Relaxation in Proton - Decoupled Carbon - ^{13}C NMR Spectra of Macromolecules," *The Journal of Chemical Physics*, vol. 56, no. 7, pp. 3683-3689, 2003.
- [79] M. P. McDougall, J. M. Knight, E. E. Eigenbrodt, S. M. Wright, and C. W. Chang, "A simple approach to overcoming mutual coupling effects in some transmit array coils for magnetic resonance imaging," *Conf Proc IEEE Eng Med Biol Soc*, pp. 2043-2046, 2008.
- [80] N. E. Hasgall PA, Gosselin MC, Klingeböck A, Kuster N, "IT'IS Database for thermal and electromagnetic parameters of biological tissues," Version 2.5, August 1st, 2014, www.itis.ethz.ch/database.
- [81] Y. T. L. S.M. Wright, J. Nvarro, and M. Davidovitz, "Antennas IV: Microstrip Antennas," *Handbook of RF/microwave components and engineering*, pp. 775-904, Hoboken, New Jersey: John Wiley & Sons, 2003.

- [82] J. S. Boyer, S. M. Wright, and J. R. Porter, "An automated measurement system for characterization of RF and gradient coil parameters," *Journal of Magnetic Resonance Imaging*, vol. 8, no. 3, pp. 740-747, 1998.
- [83] V. L. Yarnykh, "Actual flip-angle imaging in the pulsed steady state: A method for rapid three-dimensional mapping of the transmitted radiofrequency field," *Magnetic Resonance in Medicine*, vol. 57, no. 1, pp. 192-200, 2007.
- [84] S. By, J. V. Rispoli, S. Cheshkov, I. Dimitrov, J. Cui, S. Seiler, S. Goudreau, C. Malloy, S. M. Wright, and M. P. McDougall, "A 16-Channel Receive, Forced Current Excitation Dual-Transmit Coil for Breast Imaging at 7T," *PloS one*, vol. 9, no. 11, pp. e113969, 2014.
- [85] S. By, J. Rispoli, J. Cui, S. Cheshkov, I. Dimitrov, C. Malloy, S. M. Wright, and M. P. McDougall, "16-Channel Receive Array Insert for Breast Imaging at 7T," *Pro Int Soc Mag Reson Med*, pp. 2728, 2013.
- [86] D. Kidd, J. Thorpe, A. Thompson, B. Kendall, I. Moseley, D. MacManus, W. McDonald, and D. Miller, "Spinal cord MRI using multi - array coils and fast spin echo II. Findings in multiple sclerosis," *Neurology*, vol. 43, no. 12, pp. 2632-2632, 1993.
- [87] M. V. Kulkarni, C. B. McArdle, D. Kopanicky, M. Miner, H. Cotler, K. Lee, and J. Harris, "Acute spinal cord injury: MR imaging at 1.5 T," *Radiology*, vol. 164, no. 3, pp. 837-843, 1987.
- [88] G. Nijeholt, M. Van Walderveen, J. Castelijns, J. Van Waesberghe, C. Polman, P. Scheltens, P. Rosier, P. Jongen, and F. Barkhof, "Brain and spinal cord abnormalities in multiple sclerosis. Correlation between MRI parameters, clinical subtypes and symptoms," *Brain*, vol. 121, no. 4, pp. 687-697, 1998.
- [89] D. Norman, C. M. Mills, M. Brant-Zawadzki, A. Yeates, L. E. Crooks, and L. Kaufman, "Magnetic resonance imaging of the spinal cord and canal: potentials and limitations," *American Journal of Roentgenology*, vol. 141, no. 6, pp. 1147-1152, 1983.
- [90] R. A. Patchell, P. A. Tibbs, W. F. Regine, R. Payne, S. Saris, R. J. Kryscio, M. Mohiuddin, and B. Young, "Direct decompressive surgical resection in the treatment of spinal cord compression caused by metastatic cancer: a randomised trial," *The Lancet*, vol. 366, no. 9486, pp. 643-648, 2005.
- [91] A. Raaijmakers, P. Luijten, and C. Berg, "Dipole antennas for ultrahigh - field body imaging: a comparison with loop coils," *NMR in Biomedicine*, vol. 29, no. 9, pp. 1122-1130, 2015.

- [92] A. J. Raaijmakers, M. Italiaander, I. J. Voogt, P. R. Luijten, J. M. Hoogduin, D. W. Klomp, and C. A. van den Berg, "The fractionated dipole antenna: A new antenna for body imaging at 7 Tesla," *Magnetic Resonance in Medicine*, vol. 75, no. 3, pp. 1366-1374, 2015.
- [93] Q. Duan, J. H. Duyn, and H. Merkle, "Segmented Dipole: A Remotely Reconfigurable Near-Field Dipole Antenna Transmitter for Optimized 7 T Spine Imaging," *Pro Int Soc Mag Reson Med*, pp. 3512, 2016.
- [94] J. Cui, C. Sun, D. Alkandari, and S. M. Wright, "An adjustable field-of-view rung element for 7T transmit array coils using forced current excitation," *Pro Int Soc Mag Reson Med*, pp. 2673, 2017.
- [95] C. A. Balanis, *Advanced engineering electromagnetics*, Hoboken, New Jersey: John Wiley & Sons, 2012.
- [96] R. F. Harrington, *Time-Harmonic Electromagnetic Fields*, Hoboken, New Jersey: Wiley-IEEE Press, 2001.
- [97] B. van den Bergen, D. W. Klomp, A. J. Raaijmakers, C. A. de Castro, V. O. Boer, H. Kroeze, P. R. Luijten, J. J. Lagendijk, and C. A. van den Berg, "Uniform prostate imaging and spectroscopy at 7 T: comparison between a microstrip array and an endorectal coil," *NMR in Biomedicine*, vol. 24, no. 4, pp. 358-365, 2011.
- [98] H. Y. Ko, J. H. Park, Y. B. Shin, and S. Y. Baek, "Gross quantitative measurements of spinal cord segments in human," *Spinal Cord*, vol. 42, no. 1, pp. 35-40, //print, 0000.
- [99] F. Wiesinger, V. de Moortele, G. Adriany, N. De Zanche, K. Ugurbil, and K. P. Pruessmann, "Potential and feasibility of parallel MRI at high field," *NMR in Biomedicine*, vol. 19, no. 3, pp. 368-378, 2006.
- [100] I. R. Connell, K. M. Gilbert, M. A. Abou-Khousa, and R. S. Menon, "MRI RF array decoupling method with magnetic wall distributed filters," *IEEE Transactions on Medical Imaging*, vol. 34, no. 4, pp. 825-835, 2015.
- [101] N. Gudino, and M. A. Griswold, "Multi - Turn Transmit Coil to Increase B1 Efficiency in Current Source Amplification," *Magnetic Resonance in Medicine*, vol. 69, no. 4, pp. 1180-1185, 2013.
- [102] M. A. Dieringer, W. Renz, T. Lindel, F. Seifert, T. Frauenrath, F. von Knobelsdorff-Brenkenhoff, H. Waiczies, W. Hoffmann, J. Rieger, H. Pfeiffer, B. Ittermann, J. Schulz-Menger, and T. Niendorf, "Design and application of a four-channel transmit/receive surface coil for functional cardiac imaging at 7T," *Journal of Magnetic Resonance Imaging*, vol. 33, no. 3, pp. 736-741, 2011.

- [103] R. Kriegl, J.-C. Ginefri, M. Poirier-Quinot, L. Darrasse, S. Goluch, A. Kuehne, E. Moser, and E. Laistler, “Novel inductive decoupling technique for flexible transceiver arrays of monolithic transmission line resonators,” *Magnetic Resonance in Medicine*, vol. 73, no. 4, pp. 1669-1681, 2015.
- [104] M. Alecci, C. M. Collins, M. B. Smith, and P. Jezard, “Radio frequency magnetic field mapping of a 3 Tesla birdcage coil: Experimental and theoretical dependence on sample properties,” *Magnetic Resonance in Medicine*, vol. 46, no. 2, pp. 379-385, 2001.
- [105] D. Baudry, A. Louis, and B. Mazari, “Characterization of the open-ended coaxial probe used for near-field measurements in EMC applications,” *Progress In Electromagnetics Research*, vol. 60, pp. 311-333, 2006.

APPENDIX A THE USE OF INFRARED CAMERA IN DEBUGGING RF COILS AND ESTIMATING CURRENT DISTRIBUTION

Capacitor failures are common in RF transmit coils, due to the high peak voltage across it or the high RMS current running through it. Either the dielectric break down (caused by peak voltage) or the thermal stress (caused by RMS current) could cause damage in capacitors. However, it is not always possible to tell if a capacitor has failed under high power, since the appearance may look normal and the behavior on the bench may not be

Additionally, it is often of interest to measure the RF current distribution around the coil. Typically, this is done through a ‘current probe’ which is essentially a tiny shielded magnetic field probe. The probe is made so small such that it only picks up local magnetic field, and therefore is an indicator of the RF current running next to it. However it is an extremely sensitive measurement-the relative position between the coil and the probe greatly affect the reading of the probe.

It was found through experiment that thermal camera is very useful in achieving both goals. For example, unstable behavior was found with the segmented dipole during the test at UTSW on 2/20/17. On the bench however, no abnormal behavior was found using the VNA, which is a low power test. High power test was then performed together with a FLIR thermal camera. 270 W peak power was injected to the segmented dipole described in details in section 5.5. The thermal picture of the match and tune circuits are shown in Fig. 55:

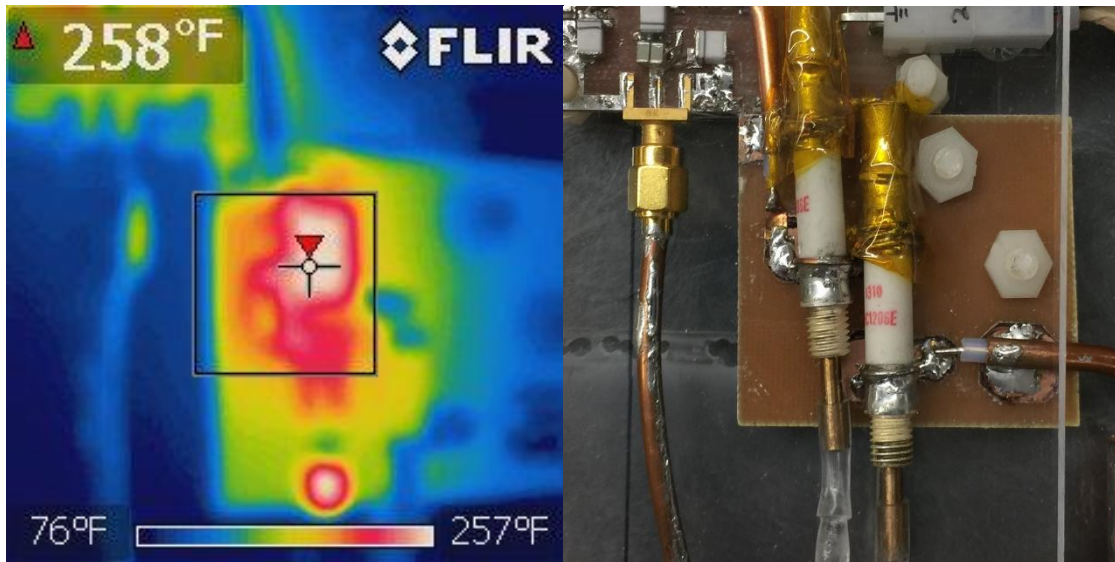


Fig. 55. Extra heat observed in the tuning capacitor

On the match and tune board are two capacitors: A tuning cap and a matching cap. They were all Voltronics NMHVE55 variable capacitors, which is rated for 600 V maximum voltage. According to the thermal reading, the tuning cap was heating much more than the matching cap, and goes up to 260 F, which indicates a potential capacitor failure. After switching the voltronic caps to Sprague-goodman capacitors, which are rated for 6 kV maximum voltage, the issue went away, as is shown in Fig. 56. With the same input power, the capacitors gets to maximum of 170 F, and there was no unexplainable difference between the matching cap and the tuning cap. Therefore, it was concluded that the previous capacitor had failed either to high peak voltage or high temperature, before the above test.

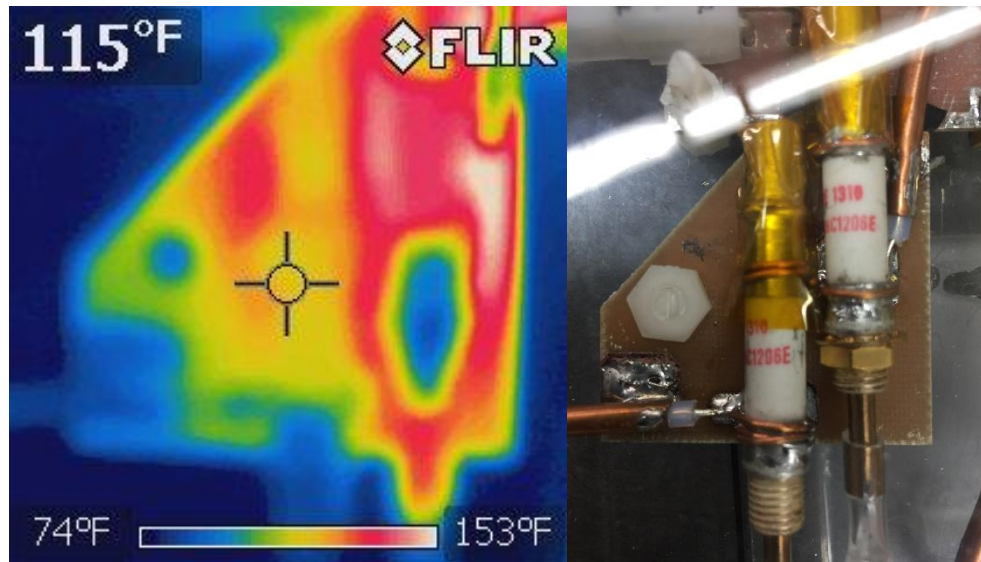


Fig. 56. Thermal images of match and tune cap after new capacitors were installed, and the reference photo

It can also be seen from the thermal photo that the difference in the heating of the capacitors are highly visible, and that metal shows up as dark because of the reflection it gives. A potential application for this is then to use the thermal camera to map the current distribution on a loop coil that is broken up by capacitors (Fig. 57): Since the copper shows up as dark, the reading on the distributed capacitors will be highly visible.



Fig. 57. A loop coil broken up by distributed capacitors

The temperature is related to heating which is proportional to the square of RF current:

$$Q = I^2 R$$

So the temperature indicates the magnitude of the current going through the capacitors. However, the sensitivity of the method needs to be investigated further. One drawback of this method is that it does not provide phase information.